

Characterisation and application of portable solar absorption spectrometers for the detection of greenhouse gas emissions from regional anthropogenic sources

Zur Erlangung des akademischen Grades eines
DOKTORS DER NATURWISSENSCHAFTEN
an der Fakultät für Physik des
Karlsruher Instituts für Technologie (KIT)

genehmigte

DISSERTATION

von

Matthias Max Frey
aus Werl

Referent: Prof. Dr. J. Orphal
Korreferent: Prof. Dr. A. Butz
Tag der mündlichen Prüfung: 06.07.2018

Abstract

In this study, a rigorous calibration procedure for a newly developed mobile Fourier transform infrared spectrometer (EM27/SUN) is implemented in the framework of the recently established Collaborative Carbon Column Observing Network (COCCON). Additionally, the long term stability of the EM27/SUN is investigated. An ensemble of these spectrometers is then used for the quantification of emission hot-spot regions of the most important greenhouse gases carbon dioxide (CO_2) and methane (CH_4).

The assurance of highly accurate and precise CO_2 and CH_4 measurements is of utmost importance for the detection of localised sources of these gases. Even a major city is expected to introduce an enhancement of CO_2 only in the sub-percent range over the atmospheric background concentration of approximately 400 ppmv.

Therefore, in the first part of this thesis a standardised calibration routine for EM27/SUN spectrometers is developed. It includes an optimisation of the spectrometers optical alignment, open path measurements for the characterisation of the instrumental line shape, and atmospheric comparison measurements with a reference EM27/SUN. Using this standardised calibration routine, 30 EM27/SUN were checked at the Karlsruhe Institute of Technology (KIT) between 2014 and 2018, leading to very uniform characteristics of the spectrometers. As a result of a collaboration with the manufacturer of the EM27/SUN, newly produced spectrometers are now routinely checked at the KIT prior to shipment to investigators worldwide. Additionally, in a 3.5 years lasting study, the long term performance of the EM27/SUN with respect to a co-located high resolution spectrometer is investigated and found to be stable on time scales of several years.

Compared to the national scale, uncertainties of local CO_2 and CH_4 emissions are higher for urban areas. Accurate observations of local sources, especially cities, are therefore important for the verification of worldwide mitigation goals. In the second part of this thesis, several EM27/SUN are utilised for the quantification of CO_2 and CH_4 emission strengths of major cities. In a first campaign performed in Berlin in June and July 2014, the EM27/SUN measurements are compared to a dispersion model using COSMO-DE high resolution wind fields. The CO_2 emission strength of Berlin is estimated to 800 kg s^{-1} .

In a second campaign, the EM27/SUN was used in April and May 2015 in Paris to verify an existing emission inventory in conjunction with the atmospheric transport model CHIMERE. It is found that the emissions in the eastern suburbs of Paris are underestimated in the model. Furthermore, opposed to the Berlin campaign, also XCH_4 gradients in the order of 5 ppbv are detected.

In a third campaign conducted in the Tokyo area from February until April 2016, the detected XCO_2 and XCH_4 gradients between different measurement sites, up to 9 ppmv and 30 ppbv, respectively, were larger compared to Berlin and Paris. The estimated CO_2 emission strength between Tokyo and Paris scales with the number of inhabitants. Also, two EM27/SUN were used to verify coincident satellite CO_2 observations from the Orbiting Carbon Observatory-2.

The findings of this thesis will support the evaluation of mitigation goals set by international treaties, e.g the Kyoto protocol and the Paris COP21 agreement.

List of Author's Publications

Frey, M., Sha, M. K., Hase, F., Kiel, M., Blumenstock, T., Harig, R., Surawicz, G., Deutscher, N. M., Shiomi, K., Franklin, J., Bösch, H., Chen, J., Grutter, M., Ohyama, H., Sun, Y., Butz, A., Mengistu Tsidu, G., Ene, D., Wunch, D., Cao, Z., Garcia, O., Ramonet, M., Vogel, F. and Orphal, J.: *Building the COllaborative Carbon Column Observing Network (COCCON): Long term stability and ensemble performance of the EM27/SUN Fourier transform spectrometer*, Atmospheric Measurement Techniques Discussions, 2018, 1-34, doi: 10.5194/amt-2018-146, 2018

Frey, M., Hase, F., Blumenstock, T., Groß, J., Kiel, M., Mengistu Tsidu, G., Schäfer, K., Sha, M. K., and Orphal, J.: *Calibration and instrumental line shape characterization of a set of portable FTIR spectrometers for detecting greenhouse gas emissions*, Atmospheric Measurement Techniques, 8, 3047-3057, doi: 10.5194/amt-8-3047-2015, 2015

Vogel, F. R., **Frey, M.**, Stauffer, J., Hase, F., Broquet, G., Xueref-Remy, I., Chevallier, F., Ciais, P., Sha, M. K., Chelin, P., Jeseck, P., Te, Y. V., Groß, J., Blumenstock, T., Tu, Q. and Orphal, J.: *XCO₂ in an emission hot-spot region: the COCCON Paris campaign 2015*, Atmospheric Chemistry and Physics Discussions, 2018, 1-37, doi: 10.5194/acp-2018-595, 2018

Hase, F., **Frey, M.**, Kiel, M., Blumenstock, T., Harig, R., Keens, A., and Orphal, J.: *Addition of a channel for XCO observations to a portable FTIR spectrometer for greenhouse gas measurements*, Atmospheric Measurement Techniques, 9, 2303-2313, doi: 10.5194/amt-9-2303-2016, 2016

Hase, F., **Frey, M.**, Blumenstock, T., Groß, J., Kiel, M., Kohlhepp, R., Mengistu Tsidu, G., Schäfer, K., Sha, M. K., and Orphal, J.: *Application of portable FTIR spectrometers for detecting greenhouse gas emissions of the major city Berlin*, Atmospheric Measurement Techniques, 8, 3059-3068, doi: 10.5194/amt-8-3059-2015, 2015

Contents

1	Introduction	1
2	Theoretical background	5
2.1	The Earth's atmosphere	5
2.1.1	Composition and vertical structure of the atmosphere	5
2.1.2	The greenhouse effect	7
2.2	Molecular absorption	8
2.2.1	Diatomic molecules	9
2.2.2	Polyatomic molecules	12
2.3	Spectral line shapes	13
2.3.1	Doppler broadening	13
2.3.2	Pressure broadening	14
2.3.3	The Voigt line shape	14
2.4	Fourier transform infrared spectroscopy	14
2.4.1	The FTIR spectrometer	14
2.4.2	The Fourier transformation	15
2.4.3	Apodisation and instrumental line shape	16
2.5	Principles of inversion theory	17
3	Infrared remote sensing networks	19
3.1	TCCON	19
3.2	COCCON	20
3.3	NDACC	20
4	Instrumentation and data analysis	21
4.1	The Bruker HR125 spectrometer	21
4.1.1	TCCON data analysis	21
4.1.2	HR125 low resolution data analysis	23
4.2	The Bruker EM27/SUN mobile spectrometer	23
4.2.1	Instrumental improvements	25
4.2.2	Instrumental line shape	28
4.2.3	Retrieval software and processing	31
4.2.4	Measurement routine	32
5	EM27/SUN long term stability and ensemble performance	35
5.1	Long term performance	36
5.1.1	ILS analysis	36
5.1.2	Total column time series	37
5.1.3	X_{air}	39

5.1.4	XCO ₂	41
5.1.5	XCH ₄	42
5.2	Ensemble performance	44
5.2.1	ILS measurements and instrumental examination	45
5.2.2	XCO ₂ and XCH ₄ comparison measurements	47
5.2.3	Conclusions	49
6	Berlin campaign	51
6.1	Calibration measurements	51
6.1.1	Instrumental line shape	51
6.1.2	Side-by-side solar calibration measurements	52
6.1.3	O ₂ column as an indicator of instrumental stability	54
6.1.4	Column-averaged dry air mole fraction	55
6.2	Campaign considerations and overview	57
6.3	Berlin X _{gas} measurements	60
6.4	Dispersion model	63
6.5	Comparison of model predictions and EM27/SUN time series	65
6.6	Conclusions	68
7	Paris campaign	69
7.1	Campaign design	69
7.2	The atmospheric chemistry transport model CHIMERE	71
7.3	Calibration measurements	73
7.4	Campaign results	74
7.4.1	Measurement results	74
7.4.2	Modelling results	78
7.4.3	Comparison of observational and model data sets	82
7.5	Conclusions	83
8	Tokyo campaign	85
8.1	Campaign design	85
8.2	Calibration measurements	86
8.2.1	ILS measurements	86
8.2.2	Comparison measurements in Tsukuba	87
8.2.3	The EM27/SUN as a transfer standard between TCCON stations	88
8.3	Campaign results	90
8.4	Comparison of EM27/SUN and OCO-2 data	92
8.5	Conclusions	94
9	Summary and outlook	95
	List of Figures	99
	List of Tables	101
	List of Acronyms	103
	Bibliography	105
	Acknowledgements	117

Chapter 1

Introduction

Greenhouse gases (GHGs) are the main driver of the anthropogenic greenhouse effect and thereby largely contribute to the increase in global mean temperature of around 1°C (Hansen et al., 2010). Carbon dioxide (CO_2) and methane (CH_4) are the most important greenhouse gases with respect to radiative forcing (RF), with CO_2 being accountable for 64 % (1.81 W m^{-2}) of the total RF of all GHGs in the Industrial era (IPCC-WG1, 2013; Myrhe et al., 2013). Compared to pre-industrial times, CO_2 has increased by around 45 % from 280 ppmv (Etheridge et al., 1996) to over 400 ppmv today (Le Quéré et al., 2018). Within the same time, CH_4 has risen from 720 ppbv to over 1800 ppbv, an increase of over 150 % (Saunio et al., 2016). The importance of reducing GHGs has also been acknowledged by international parties, leading to the Kyoto protocol¹ and subsequent Paris COP21 agreement², with different mitigation goals.

For the successful implementation of the mitigation goals cities are of special interest. Currently, over 50 % of the human population lives in congested areas (United Nations, 2015) and the future population growth is also predicted to occur mostly in urban centres. Presently, cities are estimated to be responsible for about 53 % - 87 % of the total global CO_2 emissions related to energy use. A further increase is expected (IPCC-WG3, 2014; International Energy Agency, 2017; Dhakal, 2009). While emissions of GHGs can be estimated rather precisely on national scale using fuel consumption statistics, typically with an uncertainty of 3 % - 40 % (Andres et al., 2014), higher uncertainties of 20 % - 50 % are reported for urban GHG emissions (Wu et al., 2016). The Intergovernmental Panel on Climate Change (IPCC) fifth assessment report states that "no single factor explains variations in per-capita emissions across cities and there are significant differences in per-capita GHG emissions between cities within a single country" (IPCC-WG3, 2014). Due to this large uncertainty of global contributions of urban areas today and in the future, accurate and precise city-scale observing and modelling systems are needed. To quantify total GHG emissions as well as reductions in emissions from greenhouse gases referred to in the above mentioned international treaties, standards have to be developed on how to report emissions. Currently, mainly the "bottom up" inventory methods are used. Here, different individual sinks and sources, for example cars, plants or ecoregions are characterised. By upscaling the different contributions, emission inventories and global budgets of GHG emissions are obtained (Dlugokencky et al., 2011; Le Quéré et al., 2014). Accurate reporting of carbon emissions from many different sectors is mandatory for this approach.

However, accurate reports are not available for all sectors. Furthermore, the accuracy of the "bottom up" approach is not always well known and problems might arise if contributions are overlooked, overestimated or underestimated. As an example, until recently the methane leak-

¹<https://unfccc.int/resource/docs/convkp/kpeng.pdf>

²<https://unfccc.int/resource/docs/2015/cop21/eng/10a01.pdf>

age rate in gas pipelines was underestimated in American methane emission inventories (Brandt et al., 2014). Therefore, it is important to additionally supplement this method with the "top down" approach, where the emission strength of local, regional or continental sinks and sources is estimated from inversions of atmospheric measurements in conjunction with chemistry transport models. To this aim, recently the Horizon 2020 project VERIFY³ started. Thereby, the European Union recognises the need for the independent verification of emission inventories through advanced atmospheric observations and modelling frameworks.

For the "top down" method, several types of atmospheric measurements are used, affiliated with different strengths and weaknesses. There are existing global scale⁴ and city scale (Boon et al., 2016; Lauvaux et al., 2013; McKain et al., 2012; Turnbull et al., 2014; Bréon et al., 2015) in situ networks. An accurate emission estimation from in situ measurements is complicated, because the details of the vertical mixing are difficult to parameterise in transport models (Yang et al., 2007). Furthermore, in situ instruments are sensitive to and heavily influenced by very local contributions.

Remote sensing techniques on the other hand are less sensitive to the local surroundings as they record the total column of GHGs. The Total Carbon Column Observing Network (TCCON) records total columns with reference precision to aid and calibrate satellite measurements (Wunch et al., 2011). The instruments of this network are, however, large, expensive and need good infrastructure, thus limiting the global deployment of these spectrometers. As the instruments are not mobile, they are ill suited for campaign use where regional to local sinks and sources of GHGs are quantified. Satellites like the Greenhouse Gases Observing Satellite (GOSAT) (Morino et al., 2011) or the Orbiting Carbon Observatory-2 (OCO-2) (Frankenberg et al., 2015) offer global coverage, but suffer from sparse temporal resolution (the repeat cycle of OCO-2 is 16 days) and are less accurate compared to ground based remote sensing instruments. Therefore, an estimation of emission strengths from local sources is difficult. In the future, geostationary satellites will likely facilitate these estimations.

Recently, a prototype of a mobile solar absorption spectrometer (EM27/SUN) was developed by the Karlsruhe Institute of Technology (KIT) (Gisi et al., 2012) which has been commercialised by Bruker since. Today, more than 30 EM27/SUN are operated worldwide. This instrument is a promising candidate to overcome the above mentioned shortcomings. Especially, it can be used for campaign measurements to infer GHG emissions from local sources. The enhancements in the total column of carbon dioxide, even of a city like Berlin, are small compared to the atmospheric background concentrations, typically in the sub percent domain. Therefore, the first subject of this thesis is the implementation of an extensive calibration routine for the EM27/SUN to allow the unambiguous detection of local and regional sinks and sources of various kinds. The second part of this thesis concerns then the quantification of CO₂ emissions from anthropogenic sources. In this context, for the first time worldwide, a set of EM27/SUN instruments was used for the quantification of CO₂ city emissions.

The remainder of this thesis is structured as follows. Chapter 2 starts with a short review of the characteristics of the Earth's environment, followed by an introduction into molecular absorption, as this is the physical basis of infrared remote sensing. This section is followed by a description of the Fourier transform technique, utilised for infrared remote sensing. Furthermore, the basics on inversion theory are presented here. Chapter 3 will shortly introduce the important networks engaged in infrared remote sensing.

In chapter 4 the instruments used in this thesis are described, first the high resolution Bruker IFS 125HR spectrometer, then in detail the Bruker EM27/SUN. Here, the original setup of

³<https://sc5.easme-web.eu/?p=776810>

⁴<https://www.icos-ri.eu/>

the EM27/SUN and instrumental improvements performed in the course of this PhD thesis are presented. An important part of the thesis is the characterisation of the instrumental line shape and the robust calibration of the spectrometer. Afterwards, the measurement routine and the subsequent analysis and processing of the measured spectra will be described.

The first part of chapter 5 addresses the characterisation of the long term stability of the EM27/SUN with respect to a co-located reference IFS 125HR spectrometer, a prerequisite for the operation at remote sites for long term observations. The second part of this chapter deals with the ensemble performance of the EM27/SUN. For campaigns using multiple spectrometers a high level of conformity is essential.

Having demonstrated the long term stability and the excellent level of agreement and stability between the different spectrometers in chapter 5, in chapter 6 the results of a test campaign performed in June and July 2014 are presented. Five EM27/SUN spectrometers are used for the accurate and precise observation of column-averaged abundances of CO₂ and CH₄ around the major city Berlin. Here, for the first time worldwide, mobile EM27/SUN spectrometers are used in conjunction with a simple dispersion model to infer the total emission strength of a local source.

The Berlin campaign in chapter 6 shows the potential of the EM27/SUN for the estimation of regional and local GHG emission sources, but also the limitations of the simple dispersion model used. In chapter 7 a state of the art chemistry transport model utilising a high resolution emission inventory is compared against the EM27/SUN measurements within the framework of an international cooperation. Target was the Paris megacity in April and May 2015.

Chapter 8 features another aspect of the capabilities of the EM27/SUN spectrometer. During a city campaign performed in Tokyo from February until April 2016, the EM27/SUN is used to validate the recently launched OCO-2 satellite. In chapter 9 summary and outlook are given.

Chapter 2

Theoretical background

2.1 The Earth's atmosphere

The atmosphere is vital for life on Earth. It provides animate beings with oxygen and carbon dioxide and absorbs harmful ultraviolet radiation. Furthermore, the atmospheric natural greenhouse effect warms the Earth's surface and thereby makes it habitable. In this section, relevant properties and processes of the Earth's atmosphere are introduced. First the composition and vertical temperature profile of the atmosphere are discussed. After that, the physical basis of the greenhouse effect is outlined. The content of this section is mainly based on the fifth IPCC report (IPCC-WG1, 2013), Schlager et al. (2012), Ponater et al. (2012) and Le Quéré et al. (2014).

2.1.1 Composition and vertical structure of the atmosphere

Main constituents of the Earth's atmosphere are nitrogen (N_2), oxygen (O_2) and the noble gas Argon (Ar), assuming a dry air atmosphere. The fractional concentration by volume is about 78 % for N_2 , 21 % for O_2 and 0.9 % for Ar . The impact of these gases on the climate system is negligible due to the fact that they interact only weakly with infrared radiation. On the other hand, trace gases like carbon dioxide, methane, nitrous oxide (N_2O), ozone (O_3), together amounting only to 0.04 % by volume to the Earth's atmosphere, have a large impact on the climate system of the Earth due to their radiative forcing impact. Some of these minor constituents are rather constant and long lived, like CO_2 and CH_4 , others vary considerably in time. Since the beginning of the industrial era, the amount of GHGs in the atmosphere has risen considerably (Le Quéré et al., 2018; Saunio et al., 2016). Not included in dry air is water vapour (H_2O), a major greenhouse gas, with concentrations ranging from 0 % - 5 % in the atmosphere. About 99 % of the H_2O mass is concentrated in the lower atmosphere (troposphere), where it is controlled by the hydrological cycle.

In good approximation a parcel of atmospheric air can be described by the ideal gas law:

$$p = nk_B T = \frac{\rho}{\mu} k_B T. \quad (2.1)$$

Here p denotes the pressure of the air parcel, defined by the number density n , the absolute temperature T and the Boltzmann constant k_B . The atmosphere represents a mixture of gases and can be represented by a specific density ρ . The mean mass μ of dry air is 28.97 amu.

Gravity plays a key role regarding the vertical temperature structure of the atmosphere. In a compressive atmosphere the air density decreases exponentially with height. Hydrostatic equilibrium can generally be assumed even in the presence of atmospheric flow processes as the

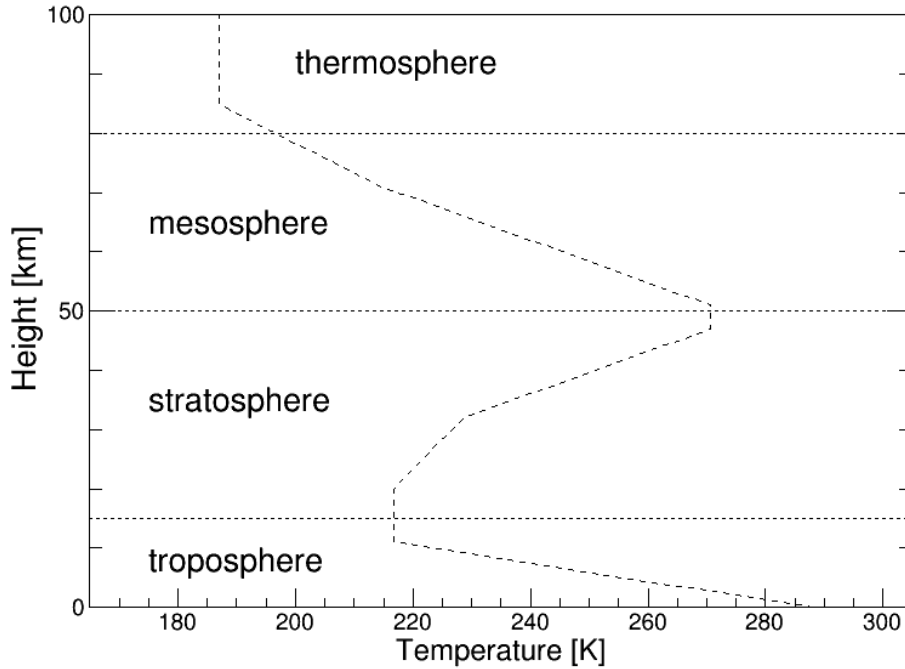


Figure 2.1: Schematic representation of the vertical structure of the atmosphere.

emerging accelerations are small with respect to the gravitational acceleration g . The hydrostatic equation for the atmosphere along the vertical height coordinate z is then given by:

$$\frac{dp}{dz} = -\rho g. \quad (2.2)$$

From Eq. 2.2 the barometric height formula can be derived:

$$\frac{p(z)}{p_0} = e^{\left(-\int_0^z \frac{1}{H(z')} dz'\right)}, \quad (2.3)$$

where p_0 is the barometric ground pressure and $H(z) = \frac{kT(z)}{g(z)\mu}$ is the scaling height. At ground level the scaling height is approximately 8 km, therefore about 90 % of the atmospheric mass is situated below a height of 15 km.

Two major layers can be distinguished in the Earth's atmosphere, the homosphere and the heterosphere. Up to a height of 100 km turbulent mixing in the circulation is happening fast so that the free path length of the molecules is small. The atmosphere is well-mixed (homosphere). On top lies the heterosphere, where diffusion becomes the most important vertical transport mechanism. The various components segregate due to the dependence of the particle velocity on the particle mass, the heavier molecules are constrained to the lower levels of the heterosphere. Even higher (~ 500 km), the free path length is large enough so that small molecules can leave the atmosphere and enter interplanetary space.

A schematic depiction of the vertical temperature profile of the Earth is shown in Fig. 2.1. The lowest vertical layer of the atmosphere is the troposphere which expands to heights of approximately 8 km at the poles and 17 km at the equator. Characteristic for the troposphere is decreasing temperature with height, the typical lapse rate is -6.5 K km^{-1} . The temperature profile is determined by convective uplifting of warm air. Water vapour plays an important role

for this mechanism. Because of the release of latent heat during the uplifting of wet air, the tropospheric temperature gradient is slightly smaller compared to the dry adiabatic air temperature gradient (10 K km^{-1}). At the tropopause, the boundary between troposphere and stratosphere, the lapse rate changes and the temperature gradient becomes positive. The temperature rises with height up to an altitude of approximately 50 km. This region is the stratosphere, the upper bound is called stratopause. The temperature increase in the stratosphere is caused by radiative heating. The solar UV radiation is absorbed by the Earth's ozone layer. Due to the rising temperature with altitude the stratospheric layer is dynamically stable and therefore there is no regular convection and associated turbulence in this part of the atmosphere. Temperatures at the stratopause reach up to 270 K, above lies the mesosphere. Due to the diminishing radiative heating caused by decreasing O_3 concentrations, the temperature sinks to heights of about 85 km, where the mesopause is located. In the thermosphere temperature increases, exceeding 1000 K, due to absorption of shortwave radiation by O_2 and N_2 . Solar activity greatly influences the state of the thermosphere. Because of the high-energy solar radiation the ion density above 75 km increases rapidly. Above the thermosphere the exosphere is located, which links the atmosphere to interplanetary space.

2.1.2 The greenhouse effect

The greenhouse effect describes the heating of the Earth's surface due to absorption of shortwave and re-emission of longwave radiation in the atmosphere, a process essential for life on Earth. A schematic depiction is given in Fig. 2.2. At the top of the atmosphere (TOA) the total solar irradiance (TSI) is about 1372 W m^{-2} , this quantity is known as the solar constant S_0 . The TSI is distributed over the Earth's surface area $4\pi R_E^2$, where R_E is the Earth's radius. The resulting global annual averaged TSI entering the atmosphere is therefore one fourth of the solar constant, 340 W m^{-2} . Of this incoming radiation about 161 W m^{-2} is absorbed by the surface, heating it to a temperature T of around 288 K. The other part is either absorbed by the atmosphere or backscattered by the atmosphere or the Earth's surface.

The absorbed radiation is re-emitted by the Earth, which can be described as a black body in thermal equilibrium. The emission spectrum is given by Planck's law:

$$B_\lambda(T, \lambda) = \frac{2hc^2\lambda^{-5}}{e^{\left(\frac{hc}{\lambda k_B T}\right)} - 1}. \quad (2.4)$$

Here λ is the wavelength of the emitted radiation, h the Planck constant and c the speed of light. The maximum spectral radiance emitted by the Earth is in the far infrared ($\lambda = 10 \mu\text{m}$), whereas for the sun it is in the visible range ($\lambda = 500 \text{ nm}$). This is due to Wien's displacement law, which can be derived from Planck's law. Integrating Planck's law over all wavelengths, one obtains the Stefan-Boltzmann law, which describes the power radiated from a source depending on temperature:

$$j = \epsilon\sigma T^4. \quad (2.5)$$

ϵ is the emissivity ($\epsilon = 1$ for a black body), $\sigma = 5.67 \cdot 10^{-8} \text{ W m}^{-2} \text{ K}^{-4}$ the Stefan-Boltzmann constant. For radiative equilibrium, absorbed and emitted energy need to be equal. Without the atmosphere and therefore no radiative interaction between Earth and atmosphere the radiation budget of the Earth is:

$$(1 - A)\frac{S_0}{4} = \epsilon_S\sigma T_S^4 \quad (2.6)$$

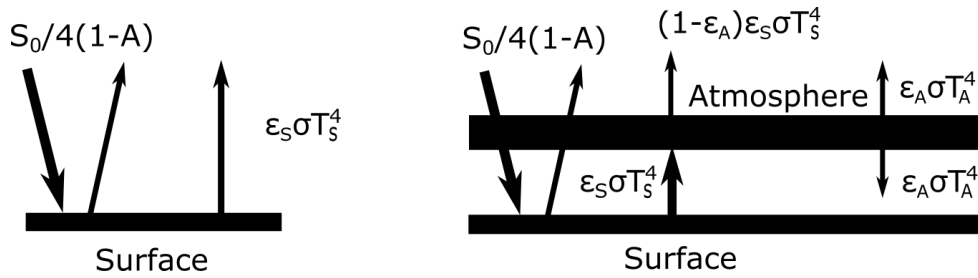


Figure 2.2: Schematic depiction of the greenhouse effect. The left panel shows a one layer model disregarding the Earth’s atmosphere. In the right panel a two-layer model taking into account the atmosphere as an absorbing and re-emitting medium is depicted.

The left side represents the incoming solar radiation reduced by the part which is reflected at the TOA and the Earth’s surface, see left panel of Fig. 2.2. This amount is known as the albedo of the Earth A . For ϵ_S and T_S , the subscript S denotes surface emissivity and surface temperature. Assuming an albedo of $A = 0.3$ and an emissivity of $\epsilon_S = 0.95$ leads to an equilibrium temperature of 258 K. The real Earth’s mean surface temperature is 288 K, the difference of 30 K is caused by the interaction of longwave radiation with the atmosphere. While some minor trace gases of the atmosphere, the GHGs, are transparent for visible light, they strongly absorb and re-emit IR radiation in all directions, thus additionally heating the surface of the Earth. Key substances are CO_2 , CH_4 , N_2O and H_2O .

To qualitatively describe the greenhouse effect, a two level system can be assumed, consisting of the surface layer and an additional atmospheric layer, see right panel of Fig. 2.2. This simple system can be described by the following equations:

$$\epsilon_S \sigma T_S^4 = (1 - A) \frac{S_0}{4} + \epsilon_A \sigma T_A^4 \quad (2.7)$$

$$\epsilon_S \sigma T_S^4 = (1 - \epsilon_A) \epsilon_S \sigma T_S^4 + 2\epsilon_A \sigma T_A^4 \quad (2.8)$$

The first equation represents the requirement for radiative equilibrium at the surface, and the second equation describes the radiative balance in the atmosphere. The subscript A denotes atmosphere. Assuming $\epsilon_A = 0.75$ one obtains a surface temperature of $T_S = 287$ K, close to the above mentioned real mean temperature of the Earth’s surface.

The outlined greenhouse effect occurs naturally. However, since the beginning of the industrial era, concentrations of GHGs have increased dramatically (Etheridge et al., 1996; Le Quéré et al., 2014), thereby reinforcing this mechanism. This is called the anthropogenic greenhouse effect.

2.2 Molecular absorption

In the following section, the interaction between molecules and electromagnetic waves, mainly infrared radiation, will be discussed. Energy is absorbed or emitted by a molecule, thereby changing its electronic, vibrational and rotational state. As the energy needed to excite a molecule is highly species-specific, from the absorption characteristics information about the structure of the molecule or physical processes can be gained. Molecular spectroscopy is therefore an important technique in many fields of science, for example physics, chemistry, medical science, biology, astronomy and environmental studies. Here it is used to derive concentrations of trace gases in the atmosphere. Due to the complexity of this topic, only a short introduction is given. The basic principles of molecular absorption are explained for diatomic molecules, after that as

an example for polyatomic molecules carbon dioxide is discussed. More details can be found in Haken and Wolf (2006), Petty (2007) and Demtröder (2010).

2.2.1 Diatomic molecules

Inside a molecule, the atoms can perform vibrations with respect to their state of equilibrium. The frequencies of the vibrations typically lie in the infrared spectral region. For diatomic molecules the interaction between the atoms m_1 and m_2 is approximately described by a harmonic oscillation with the force constant k . The quantum mechanical calculation yields the energy levels:

$$E_{vib} = \hbar\omega \left(\nu + \frac{1}{2} \right), \quad \nu = 0, 1, 2, \dots \quad \text{with} \quad \omega = \sqrt{\frac{k}{\mu}}. \quad (2.9)$$

Here \hbar denotes the reduced Planck constant, ν the vibrational quantum number, ω the vibration frequency and $\mu = \frac{m_1 m_2}{m_1 + m_2}$ the reduced mass. In the harmonic approximation the differences between two adjacent energy levels are equidistant, $\Delta E = \hbar\omega = E_{\nu+1} - E_\nu$. As the harmonic oscillator selection rule requires $\Delta\nu = \pm 1$, the transition amplitudes are only different from zero for adjacent energy levels, . At room temperature ($T \approx 300$ K), $k_B T$ is about one order of magnitude smaller than $\hbar\omega$ so that almost all molecules are located in the ground state. Therefore, the dominating transition is from $\nu = 0$ to $\nu = 1$.

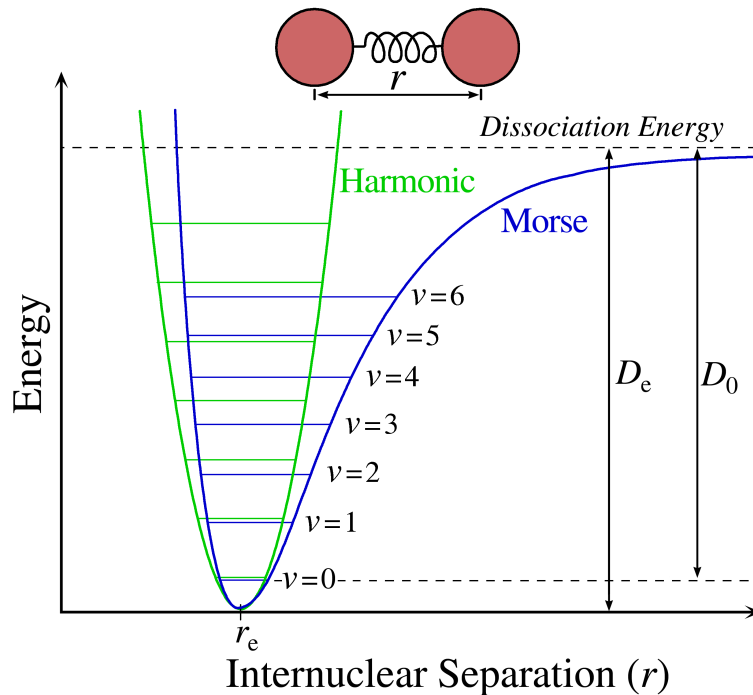


Figure 2.3: Schematic depiction of the Harmonic potential and the Morse-potential. The higher energy levels of the Morse-potential are lowered with respect to the Harmonic potential. Image taken from Wikipedia (www.wikipedia.org/wiki/Anharmonischer_Oszillator#/media/File:Morse-potential.png).

For the lower energy states the harmonic oscillator is a good approximation. However, it is clear that the real potential has to be asymmetric with respect to the equilibrium position R_e .

Reducing the distance below R_e will lead to an increasingly repulsing potential, which prevents the permeation of the atoms. A large distance $R > R_e$ on the other hand leads to a weakening of the molecular bond and eventually to dissociation, in other words the potential curve flattens out towards a constant value, the dissociation energy D_e . The harmonic potential together with a more realistic potential (Morse-potential) is depicted in Fig. 2.3. The energy levels of the anharmonic oscillator are in good approximation:

$$E_{vib} = \hbar\omega \left(\nu + \frac{1}{2} \right) \left[1 - x_e \left(\nu + \frac{1}{2} \right) \right] \quad \text{with} \quad x_e = \frac{\hbar\omega}{4D_e}. \quad (2.10)$$

The first part can be identified as the energy levels of the harmonic oscillator, whereas the second part is due to the anharmonicity of the potential. x_e is the anharmonicity constant, which is the ratio between the harmonic oscillator energetic quantum and four times the dissociation energy. In contrast to an ideal quantum mechanical harmonic oscillator the energy levels are not equidistant anymore but decrease with increasing ν . Moreover, transitions larger than $\Delta\nu \pm 1$ are allowed. These are called overtones, and for higher $\Delta\nu$ their intensity rapidly decreases, resulting in much weaker spectral lines.

A molecule does not only vibrate, it also has the ability to rotate. Instead of one line corresponding to the vibration frequency of the transition, due to the rotation energy, for highly resolved spectra one observes a multitude of nearby lines, called a spectral band. For diatomic molecules, in the simplest case the rotational energy is approximated by the model of the rigid rotator. In contrast to the vibration energy, differences between the energy levels are not equidistant, but increase linearly with the rotational quantum number J . The energy levels are given by:

$$E_{rot} = hcBJ(J+1), \quad J = 0, 1, 2, \dots \quad \text{with} \quad B = \frac{h}{8\pi^2c\Theta}. \quad (2.11)$$

B is the rotational constant and $\Theta = \mu R^2$ the moment of inertia (R denotes the bond length of the molecule). B is an important measurement quantity which gives information about the structure of the molecule. The selection rule for optical transitions concerning the angular momentum is $\Delta J = \pm 1$.

So far the centrifugal force was neglected. Including this effect one arrives at the model of the non-rigid rotator, which takes into account that with increasing rotation the molecule expands. Qualitatively, the stretching of the molecule leads to a larger angular momentum, in turn resulting in a smaller B , therefore lowering the energy values:

$$E_{rot} = hcBJ(J+1) - hcDJ^2(J+1)^2 \quad \text{with} \quad D = \frac{\hbar^3}{4\pi k\Theta^2 R_c^2 c}. \quad (2.12)$$

D denotes the distortion constant. Eq. 2.12 holds true for a harmonic force field. Accounting for an anharmonic force field introduces higher order terms of J .

In the Born-Oppenheimer approximation, the energy levels of a molecule are a combination of its electronic energy E_{el} and rotational-vibrational energy:

$$E_{tot} = E_{el} + E_{vib} + E_{rot}. \quad (2.13)$$

The energy for transitions between the different rotational-vibrational states is provided by absorbed photons. The main part of the energy comes from the change in the vibrational state while the energy needed to change the rotational state is rather small. A typical energy level scheme is depicted in Fig. 2.4. For a transition between ν and $\nu + 1$ the absorption lines can be divided into three groups, the branches of a transition band. Transitions with $\Delta J = -1$ span

smaller energy differences for higher J and are called P-branch. For $\Delta J = +1$ the transitions span larger energy differences for higher J , this is the R-branch. A pure vibrational transition $\Delta J = 0$, called Q-branch, is only allowed for molecules with an angular momentum parallel to their symmetry axis. Compared to the P-branch and R-branch, the absorption lines are much more closely spaced. Often there is only one strong line visible because the lines overlap.

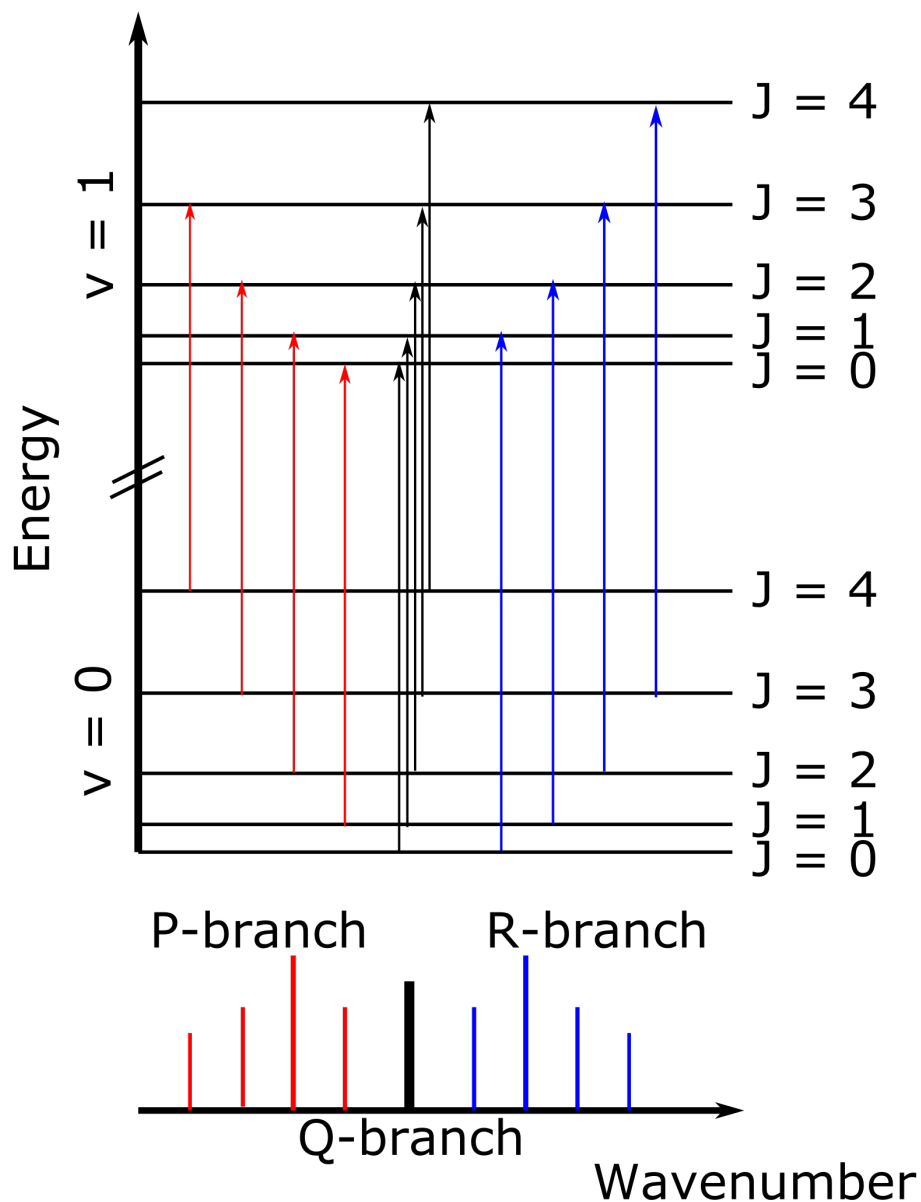


Figure 2.4: Illustration of the rotational-vibrational energy transitions for different vibrational and rotational quantum numbers. The corresponding transition lines are shown below. The intensity of a particular transition is proportional to the population density of the corresponding energy level.

Schematically shown in Fig. 2.4 are the line intensities of a transition band. They scale with the population N_J of the molecular rotational state. The ratio can be described using the Boltzmann statistics:

$$\frac{N_J}{N_0} = (2J + 1)e^{-(E_J - E_0)/k_B T}. \quad (2.14)$$

Starting at the centre of the transition band, first the line strength increases linearly due to the increasing statistical weight of the states caused by the $2J + 1$ degeneracy of the rotational states. Further away from the centre of the band, the line strength decreases again when the thermal distribution of the molecular states becomes dominant.

It should be noted that a transition between two energy states is not equivalent to a measurable spectral signature. The transition is only active in the infrared if during the transition the dipole moment of the molecule changes. A diatomic molecule with symmetric charge distribution like N_2 cannot emit dipole radiation. However, multipole transitions of O_2 and N_2 signatures are possible. The transition elements are close to zero, therefore the transition is unlikely, but because of the large quantities in the atmosphere N_2 and O_2 are detectable with solar absorption spectroscopy.

2.2.2 Polyatomic molecules

Until now only diatomic molecules were discussed. The spectra of polyatomic molecules are more complex. In order to determine the location of N atoms, $3N$ coordinates are needed. This is the number of degrees of freedom (DOF) of the system. For describing the centre of mass motion 3 DOF are needed, additional 3 DOF for the rotation of the molecule. The remaining $3N - 6$ DOF are the normal vibration modes f of the system. Linear molecules contain $f = 3N - 5$ normal vibration modes because there are only 2 rotational DOF. In addition to the normal modes and their overtones, also linear combinations of the vibrational modes are possible. In contrast to diatomic molecules also transitions with $\Delta J = 0$ are allowed, giving rise to the Q-branch.

For this thesis, the linear molecule CO_2 , consisting of one carbon atom and two oxygen atoms, is of special interest. CO_2 has $f = 9 - 5 = 4$ vibrational normal modes, which are depicted in Fig. 2.5. With $\tilde{\nu} = \frac{1}{\lambda}$ denoting the wavenumber, the symmetric stretching vibration $\tilde{\nu}_2 = 1388 \text{ cm}^{-1}$ is infrared inactive, the asymmetric stretching vibration $\tilde{\nu}_1 = 2349 \text{ cm}^{-1}$ and the bending vibration $\tilde{\nu}_3 = 667 \text{ cm}^{-1}$, which is degenerated twice, are infrared active. For the stretching vibrations the $\Delta J = 0$ transition is forbidden whereas it is allowed for the bending vibration due to the dipole moment change perpendicular to the molecular axis. Fig. 2.6 shows the structure of the $2\tilde{\nu}_1 + 2\tilde{\nu}_2 + \tilde{\nu}_3$ CO_2 combination band recorded with the IFS 125HR spectrometer in Karlsruhe. The P-branch and the R-branch are clearly visible, as well as the general shape of the spectral band discussed above.

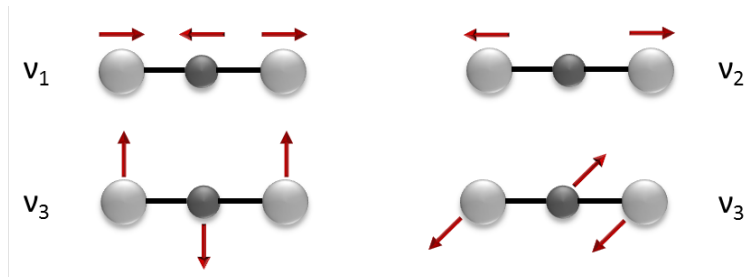


Figure 2.5: The four vibration modes of the CO_2 molecule. The symmetric stretching vibration $\tilde{\nu}_2$ is infrared inactive, whereas the asymmetric stretching vibration $\tilde{\nu}_1$ and the bending vibration $\tilde{\nu}_3$ are infrared active. The bending vibration is degenerated twice.

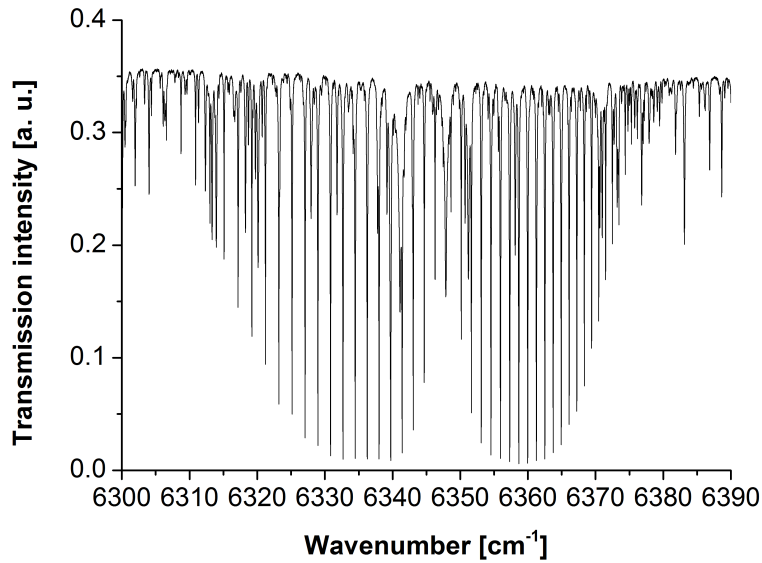


Figure 2.6: Atmospheric transmission spectrum of CO₂ recorded in Karlsruhe with the IFS 125HR spectrometer. The P-branch and the R-branch are clearly visible.

2.3 Spectral line shapes

Spectral lines from emission or absorption of radiation are inherently not infinitesimally narrow. Several mechanisms lead to a specific shape and broadening. The always existing natural line width, existing due to the finite lifetime of the excited states, has a Lorentzian shape and a typical full width at half maximum (FWHM) of $\Delta\tilde{\nu} = 10^{-8} \text{ cm}^{-1}$. For atmospheric conditions the natural line broadening can be neglected compared to the other broadening mechanisms discussed in this section.

2.3.1 Doppler broadening

The unsystematic thermal motion of molecules leads to a statistical Doppler shift during the emission of a photon resulting in a broadening of spectral lines. For a thermal velocity v , the observed wavenumber $\tilde{\nu}$ is altered with respect to the rest wavenumber $\tilde{\nu}_0$ according to:

$$\tilde{\nu} = \tilde{\nu}_0 \cdot \frac{1}{c \pm v}. \quad (2.15)$$

For a thermal gas the velocity distribution is given by the Maxwell-Boltzmann distribution:

$$P_v(v)dv = \sqrt{\frac{m}{2\pi k_B T}} e^{-\frac{mv^2}{2k_B T}} dv \quad (2.16)$$

The resulting spectral line has a Gaussian shape and is temperature dependent:

$$f_D(\tilde{\nu}) = \frac{1}{\sigma\sqrt{2\pi}} e^{-\frac{1}{2}\left(\frac{\tilde{\nu}-\tilde{\nu}_0}{\sigma}\right)^2} \quad \text{with} \quad \sigma = \sqrt{\frac{k_B T \tilde{\nu}_0^2}{mc^2}} \quad (2.17)$$

The FWHM of the Doppler line shape is $\Delta\tilde{\nu}_D = \tilde{\nu}_0 \sqrt{\frac{8k_B T \ln 2}{mc^2}}$. The Doppler broadening is therefore dependent on temperature as well as molecular mass and is proportional to the wavenumber. As an example, for the combination band of CO₂ discussed in section 2.2, assuming a temperature of 270 K the Doppler broadening is approximately $\Delta\tilde{\nu}_D = 7 \cdot 10^{-3} \text{ cm}^{-1}$.

2.3.2 Pressure broadening

In the atmosphere, a molecule is always exposed to collisions with other molecules, causing a shortening of the lifetime of the excited states and broadened line shapes. The probability for a collision increases with the number density of the molecules. Therefore, this effect is more important in the lower atmospheric levels. Similar to the natural line broadening, the shape of the pressure broadened lines is Lorentzian:

$$f_P(\nu) = \frac{1}{\sqrt{\pi}} \frac{\Delta\nu_P}{\nu^2 + \Delta\nu_P^2}. \quad (2.18)$$

The width of this Lorentz profile is dependent on the mean time between two collisions τ_{coll} :

$$\Delta\nu_P = \frac{1}{2\pi\tau_{coll}c} \propto p \quad \text{with} \quad \tau_{coll} \propto \frac{\sqrt{T}}{p}. \quad (2.19)$$

The FWHM of this profile is proportional to the pressure p . Therefore, it is the dominating contribution to the line shape in the troposphere. Assuming a pressure $p \approx 1000$ hPa, the pressure broadening is about $\Delta\tilde{\nu}_P \approx 0.1$ cm⁻¹. This is in good agreement with the measured value for the FWHM of the lines in Fig. 2.6.

2.3.3 The Voigt line shape

For a typical atmospheric scene both pressure and Doppler broadening contribute to the shape of a spectral line. The Voigt profile is the convolution of the Gaussian and Lorentzian profile:

$$f_V(\tilde{\nu}) = \int_{-\infty}^{\infty} f_P(\tilde{\nu}) f_D(\tilde{\nu} - \tilde{\nu}') d\tilde{\nu}'. \quad (2.20)$$

The above equation cannot be solved analytically. However, numerical approximations can be used (e.g. Humlicek (1979); Liu et al. (2001)). Due to the computational expense of the convolution operation, the Voigt profile is often approximated using a pseudo-Voigt profile.

2.4 Fourier transform infrared spectroscopy

Fourier transform infrared (FTIR) spectroscopy has evolved into one of the most powerful and most used technique in many fields of science. Here it is used for remote sensing of GHGs. In this section, the principles of FTIR spectroscopy are explained. First the design and principle of a FTIR spectrometer is explained. After that the procedures for deriving a spectrum from the interferogram (IFG), which is the raw product of the FTIR spectrometer, is given. The content of this section is mainly based on Beer (1992) and Davis et al. (2010).

2.4.1 The FTIR spectrometer

In Fig. 2.7 a schematic depiction of a Michelson interferometer, which generally is the main part of a FTIR spectrometer, is given. The incoming collimated radiation from an external light source, e.g. the sun or a lamp, is divided into two partial beams by the beamsplitter (BS). One part is reflected to a fixed mirror, the other part is transmitted to a movable mirror, thereby introducing a path difference between the partial beams. After recombination they interfere depending on the path difference. The interference pattern, in other words the fluctuating intensity of the recombined light beam, is recorded by a detector. The detected signal consists of a constant part $I_{DC}(x)$ and a fluctuating part $I_{AC}(x)$:

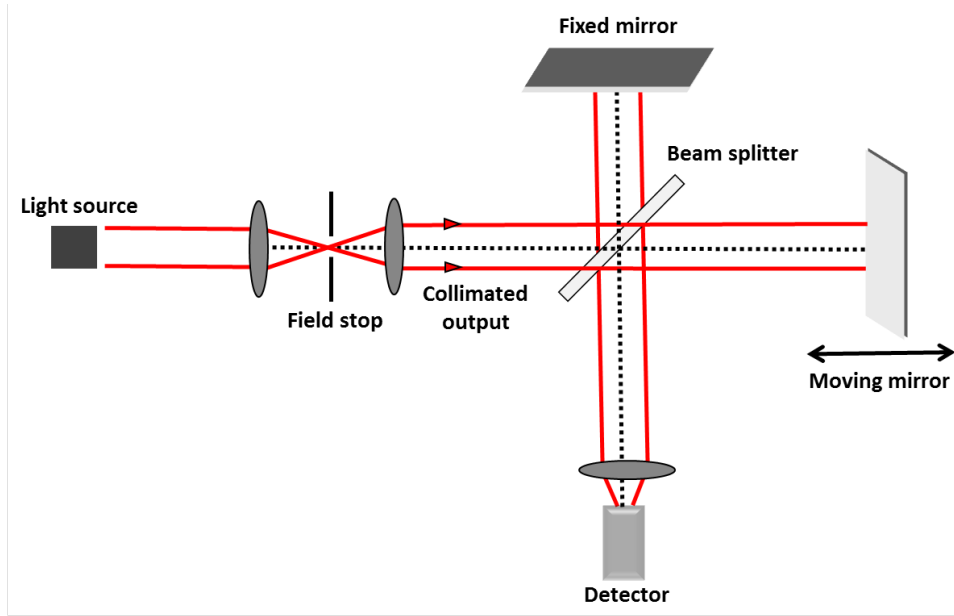


Figure 2.7: Schematic depiction of a Michelson interferometer, which is the main part of a FTIR spectrometer.

$$\bar{I}(x) = \int_0^{\infty} I(\tilde{\nu})(1 + \cos(2\pi\tilde{\nu}x))d\tilde{\nu} \quad (2.21)$$

$$= I_{DC}(x) + I_{AC}(x) \quad (2.22)$$

$I_{AC}(x)$ is commonly referred to as the interferogram and in the following the subscript AC will be omitted and denoted $I(x)$. $I(x)$ yields the spectral information of the Fourier transform spectrometer (FTS). To precisely determine the optical path difference, in the case of the instruments used in this study a helium-neon laser is used. The laser beam moves through the interferometer exactly like the radiation of the light source. A sampling point is recorded at each zero crossing of the laser AC interferograms. Uncorrected offsets of the laser signal lead to systematic errors in the resulting spectrum, see section 4.2.1 for details.

2.4.2 The Fourier transformation

The interferogram $I(x)$ and the spectrum $S(\tilde{\nu})$ are linked via the Fourier analysis and the Fourier synthesis, which together form the Fourier transformation:

$$S(\tilde{\nu}) = F(I(x)) = \int_{-\infty}^{\infty} e^{-i2\pi\tilde{\nu}x} I(x)dx \quad (2.23)$$

$$I(x) = F^{-1}(S(\tilde{\nu})) = \int_{-\infty}^{\infty} e^{i2\pi\tilde{\nu}x} S(\tilde{\nu})d\tilde{\nu} \quad (2.24)$$

The above mentioned case is an idealistic depiction. Measured interferograms are neither continuous, nor infinite. Therefore, the continuous Eq. 2.23 and 2.24 have to be converted to a discrete Fourier transform with N equally spaced sampling points with distance Δx :

$$S(n\Delta\tilde{\nu}) = \sum_{m=1}^N e^{(-i2\pi n\Delta\tilde{\nu}m\Delta x)} I(m\Delta x) \quad (2.25)$$

$$I(m\Delta x) = \frac{1}{N} \sum_{n=1}^N e^{(i2\pi n\Delta\tilde{\nu}m\Delta x)} S(n\Delta\tilde{\nu}). \quad (2.26)$$

The unambiguous reconstruction of the spectral function from equidistantly spaced sampling points with spacing Δx is only possible if the frequency range ($\tilde{\nu}_{max} - \tilde{\nu}_{min}$) is limited:

$$\frac{1}{\Delta x} > 2(\tilde{\nu}_{max} - \tilde{\nu}_{min}) \quad (2.27)$$

The above equation is the Nyquist theorem. If the spectrum contains frequencies outside this range, these contributions are folded back into the observed range leading to systematic distortions of the spectrum. For the FTIR spectrometers used in this work, the sampling interval is derived from interferences of a HeNe laser (633 nm) and the desired high-folding limit is $\tilde{\nu}_{max} = 15798 \text{ cm}^{-1}$. Therefore, in order to fulfill the Nyquist theorem, a sampling point has to be recorded at every zero crossing of the laser AC interferograms, not only the uprising zero crossing. This poses additional challenges to the electronics board of the instrument and has for a long time been an error source in FTIR spectroscopy (Messerschmidt et al., 2010). For the EM27/SUN this effect was also diagnosed and corrected, see section 4.2.1.

2.4.3 Apodisation and instrumental line shape

So far it was assumed that the path length of the moving mirror is unlimited, whereas in practice the interferogram is truncated at the maximum optical path difference (MOPD). Mathematically, the resulting spectrum $S_{meas}(\tilde{\nu})$ can be described as the convolution of the Fourier transform of the infinite interferogram $I_{ideal}(x)$ and the Fourier transform of the boxcar function $B(x)$:

$$S_{meas}(\tilde{\nu}) = F(I_{ideal}(x)) \otimes F(B(x)) \quad (2.28)$$

$$= S_{ideal}(\tilde{\nu}) \otimes \frac{\sin(2\pi MOPD\tilde{\nu})}{\pi\tilde{\nu}} \quad (2.29)$$

$B(x)$ is 1 for $x \leq |MOPD|$ and 0 otherwise. The Fourier transform of $B(x)$ is the sinc function. The spectral resolution of the spectrometer is defined by this sinc function. The FWHM is $\Delta\tilde{\nu} = \frac{0.6035}{MOPD}$. An unwanted effect of the sinc function is the appearance of unphysical, negative sidelobes in the spectrum. In order to suppress the negative sidelobes, sometimes a numerical apodisation is applied. An apodisation is the multiplication of the boxcar function with another function like a triangular or specially designed functions. This is especially important for low resolution instruments like the EM27/SUN. On the downside an apodisation decreases the spectral resolution and amplifies the correlation between measured values from different spectral positions. A good compromise between acceptable resolution, degradation, and suppressing the negative sidelobes is the Norton-Beer medium function (Beer, 1992), which was applied to the measured interferograms of the EM27/SUN spectrometer in this thesis.

The instrumental characteristics of the spectrometer can be expressed by a spectral response function, the so called instrumental line shape (ILS). The ILS is commonly separated into two parts for FTIR spectrometers. The first part exists also for ideally aligned spectrometers and stems from the fact that the interferogram is finite and the spectrometer takes in radiation which

is not perfectly parallel. This alters the ILS, since the path difference of the partial beams is dependent on the inclination of the beam. This effect can easily be taken into account if the spectrometers field stop radius r and the focal length f of the collimator in front of the field stop are known:

$$\Delta\tilde{\nu} = \frac{1}{2}\tilde{\nu}_0\alpha_{max}^2 \quad \text{with} \quad \alpha_{max} \approx \frac{r}{f} \quad (2.30)$$

Here α_{max} is the maximum angle from which the radiation enters the spectrometer, also called the semi Field of View (semiFOV). $\tilde{\nu}_0$ is the wavenumber of the incoming radiation. From Eq. 2.30 it is apparent that the ILS becomes wavenumber dependent. This part of the ILS is the self-apodisation, calculated via:

$$M_{self}(x) = \text{sinc}(\pi\Delta\tilde{\nu}x) \quad (2.31)$$

Apart from this effect, there is a second component of the ILS due to misalignments and optical aberrations of the spectrometer. This part is usually described by a modulation efficiency (ME) amplitude and a phase error, both functions of the optical path difference. These parameters are derived from experiments, either gas cell measurements (Hase et al., 1999) or open path measurements (Frey et al., 2015). In the course of this thesis, a method for characterising the ILS of the EM27/SUN spectrometer from open path measurements was developed and refined. During the last four years the ILSs of 30 spectrometers were characterised with this method, see sections 4.2.2 and 5.2.

2.5 Principles of inversion theory

The construction of a measurement parameter \mathbf{y} from target variables \mathbf{x} , also called state vector, using a function \mathbf{f} is known as the direct or forward problem, whereas the reconstruction of \mathbf{x} from \mathbf{y} is called inverse problem. In atmospheric FTIR spectroscopy, \mathbf{y} is typically a transmission spectrum, while \mathbf{x} is consisting among others of trace gas abundances. A detailed description of the inversion theory can be found in Rodgers (2000), on which this section is based on. In the following the convention is such that small letters denote scalars, bold small letters designate vectors and bold capital letters denote matrices.

An inversion calculation normally starts with the forward model, which approximates the measurement:

$$\mathbf{y} = \mathbf{f}(\mathbf{x}, \mathbf{u}) \quad (2.32)$$

Here \mathbf{x} is a N -dimensional vector of independent variables that are unknown and shall be reconstructed by the inversion of the model \mathbf{f} . \mathbf{u} are known parameters kept constant during the inversion. Generally \mathbf{f} is non-linear and has to be linearised for the inversion:

$$\mathbf{y}(\mathbf{x}, \mathbf{u}) = \mathbf{f}(\mathbf{x}_0, \mathbf{u}) + \frac{\partial \mathbf{f}}{\partial \mathbf{x}}(\mathbf{x} - \mathbf{x}_0) \quad (2.33)$$

$$\mathbf{y}(\mathbf{x}, \mathbf{u}) = \mathbf{f}(\mathbf{x}_0, \mathbf{u}) + \mathbf{K}(\mathbf{x} - \mathbf{x}_0) \quad (2.34)$$

Here $\mathbf{K} = \frac{\partial \mathbf{f}}{\partial \mathbf{x}}$ is the $N \times M$ -dimensional Jacobian matrix, where M is the dimension of the measurement vector \mathbf{y} . The linearisation around a reference state \mathbf{x}_0 is only locally permissible. Therefore, the linearised inversion has to be iterated multiple times to arrive at the final solution. Because often $N > M$, the inversion problem is overdetermined. To derive a solution the squared

norm of the difference between \mathbf{y} and \mathbf{y}_{meas} weighted with the inverted covariance matrix \mathbf{S}_y is minimised:

$$\|\mathbf{y}_{\text{meas}} - \mathbf{y}(\mathbf{x})\|_{\mathbf{S}_y^{-1}}^2 = (\mathbf{y}_{\text{meas}} - \mathbf{y}(\mathbf{x}))^T \mathbf{S}_y^{-1} (\mathbf{y}_{\text{meas}} - \mathbf{y}(\mathbf{x})) = \text{minimal} \quad (2.35)$$

The diagonal elements of \mathbf{S}_y contain the uncertainty of each measurement value as variances, $S_{y,ii} = \sigma_i^2$. Transposed matrices and vectors are denoted with superscript T .

The estimate for the state vector after $i + 1$ iterations using the Gauss-Newton iteration is:

$$\mathbf{x}_{i+1} = \mathbf{x}_i + (\mathbf{K}_i^T \mathbf{S}_y^{-1} \mathbf{K}_i)^{-1} \mathbf{K}_i^T \mathbf{S}_y^{-1} (\mathbf{y}_{\text{meas}} - \mathbf{y}(\mathbf{x}_i)) \quad (2.36)$$

The iteration is terminated if the difference between \mathbf{x}_{i+1} and \mathbf{x}_i converges against a preset small value. If the inversion problem is highly non-linear, the iteration might lead to values for which the linear approximation is not eligible. In order to avoid this problem, the Levenberg-Marquardt algorithm can be used which introduces a damping parameter so that large differences between two iteration steps do not occur.

In most cases Eq. 2.36 is not useful for the reconstruction of trace gas amounts from remote sensing measurements simply because the information from the experiment is insufficient. The $\mathbf{K}^T \mathbf{S}_y^{-1} \mathbf{K}$ matrix is nearly singular, leading to unrealistic oscillations in the inverted profile. To retrieve realistic gas profiles side constraints, so called regularisations, are used. Introducing the regularisation to Eq. 2.35 leads to:

$$\|\mathbf{y}_{\text{meas}} - \mathbf{y}(\mathbf{x})\|_{\mathbf{S}_y^{-1}}^2 + \gamma \|\mathbf{B}(\mathbf{x} - \mathbf{x}_a)\|^2 = \text{minimal} \quad (2.37)$$

\mathbf{x}_a is an a priori set of state variables, \mathbf{B} is the regularisation matrix, in the simplest case the unity matrix. Common regularisation methods are the Tikhonov-Phillips regularisation and the optimal estimation approach. The former is applied in this work. From the mathematical point of view both techniques are equivalent. For the Tikhonov-Phillips regularisation often a constraint is used that enforces a smooth profile shape. To achieve this, \mathbf{B} is usually chosen as the discrete first order derivative operator. The iterative solution is:

$$\mathbf{x}_{i+1} = \mathbf{x}_i + (\mathbf{K}_i^T \mathbf{S}_y^{-1} \mathbf{K}_i + \gamma \mathbf{B}^T \mathbf{B})^{-1} (\mathbf{K}_i^T \mathbf{S}_y^{-1} (\mathbf{y}_{\text{meas}} - \mathbf{y}(\mathbf{x}_i)) + \gamma \mathbf{B}^T \mathbf{B} (\mathbf{x}_a - \mathbf{x}_i)) \quad (2.38)$$

The regularisation parameter γ adjusts the strictness of the constraint. For large γ , the solution is close to the a priori state vector, while for small γ , the contribution of the a priori to the solution is insignificant. For the optimal estimation approach, in Eq. 2.38 $\gamma \mathbf{B}^T \mathbf{B}$ has to be replaced by inverted covariance matrix \mathbf{S}_y of the a priori information.

The averaging kernel matrix \mathbf{A} describes the vertical resolution of a measurement:

$$\mathbf{A} = (\mathbf{K}^T \mathbf{S}_y^{-1} \mathbf{K} + \gamma \mathbf{B}^T \mathbf{B})^{-1} \mathbf{K}^T \mathbf{S}_y^{-1} \mathbf{K} \quad (2.39)$$

As the a priori profile \mathbf{x}_a is always relatively smooth, as it is often a climatological mean profile, also the solution of Eq. 2.38 is smoothed, compared to the solution without constraint for which \mathbf{A} is the unity matrix.

For real measurements, the column vectors of \mathbf{A} are the response to a delta disturbance at one height level. The column vectors describe the vertical correlation between the different height levels. They are normally peaked functions where the width describes the vertical resolution of the retrieval, assuming \mathbf{x} is a vertical gas profile. \mathbf{A} is among others dependent on the spectral resolution of the instrument. It will be seen in section 5.1.5 that this different sensitivity induces biases between high resolution and low resolution spectrometers, especially on days where the true state of the atmosphere differs significantly from the a priori state.

Chapter 3

Infrared remote sensing networks

3.1 TCCON

The Total Carbon Column Observing Network was founded 2004 with the aim of providing long-term column-averaged abundances of GHGs with reference precision for the validation of NASA's OCO mission. Currently, there are 23 operational sites (Wunch et al., 2015), depicted in Fig. 3.1. The sites span a wide range of observing conditions, from the tropics to the polar regions, continental and maritime, urban and rural. TCCON data is used for carbon cycle studies (e.g. Sussmann et al. (2012); Guerlet et al. (2013); Deutscher et al. (2014)), validation of satellite measurements and satellite algorithm advancement (e.g. Butz et al. (2011); Schepers et al. (2012); Bösch et al. (2013)) as well as development of improved spectroscopic models and line lists (e.g. Tran et al. (2010); Gordon et al. (2011); Reuter et al. (2012)). The network operates high resolution Bruker IFS 125HR spectrometer.

As the instruments need good infrastructure and are expensive, TCCON has sparse coverage in large parts of the world, namely Africa, South America and parts of Asia. Also, the instruments need expert maintenance, further complicating the operation at remote sites.



Figure 3.1: Map of previous, operational and future TCCON stations. Image taken from Wunch et al. (2015).

3.2 COCCON

The Collaborative Carbon Column Observing Network (COCCON) was started up in 2014 with the aim of setting up a centralised framework for operating the EM27/SUN spectrometer ensuring reliable instrument performance, calibration of each instrument with respect to TCCON and development of a centralised processing and data storage facility. Scientifically, the goal is to expand the reach of the existing TCCON to remote areas with low infrastructure, which are not easily accessible, validation of satellite measurements and quantifying local and regional GHG emission sinks and sources. At the moment the focus lies on the latter goal. COCCON utilises the Bruker EM27/SUN spectrometer, a mobile FTIR spectrometer. As a result of the fruitful collaboration with the manufacturer, new instruments are double-checked at the Karlsruhe Institute of Technology. In detail, each new instrument is tested, optimised (diagnosis and correction of non-ideal alignment, double-passing, channelling, non-linearity issues, solar tracker problems or inaccurate positioning of the second detector, see section 4.2) and calibrated prior to deployment. This approach ensures a high level of conformity between the instruments, a prerequisite for campaign deployment and long-term carbon cycle studies.

Even to remote areas, the EM27/SUN can easily be shipped. In January 2016 the author of this thesis installed a first COCCON station in Namibia.

3.3 NDACC

The Network for the Detection of Atmospheric Composition Change (NDACC) started operations 1991 (De Mazière et al., 2018). It is composed of over 70 globally distributed ground based remote sensing research sites. Within the NDACC, the Infrared Working Group (IRWG) operates 22 stations operating Fourier transform spectrometers for solar absorption measurements in the mid infrared (MIR). The aim of NDACC is to provide consistent, high quality, long term measurements of trace gases and particles for the detection of overall trends in the composition of the upper troposphere and stratosphere. In the beginning, the primary focus was the monitoring of ozone and ozone depleting substances. The initial data products were total columns of O_3 , HCl, HNO_3 , $ClONO_2$ and HF. Today NDACC contributes to carbon cycle studies and retrieves numerous trace gases. These data products are used for satellite validation and model studies (e.g. Sussmann et al. (2005); de Laat et al. (2010)).

Chapter 4

Instrumentation and data analysis

Parts of this chapter have been adopted from Frey et al. (2015) and Frey et al. (2018).

4.1 The Bruker HR125 spectrometer

As part of the TCCON the Karlsruhe Institute of Technology operates a high resolution ground based FTIR spectrometer at KIT, Campus North (CN) near Karlsruhe (49.100° N, 8.439° E, 112 m a.s.l.). Standard TCCON instruments have been described in great detail elsewhere (Washenfelder et al., 2006; Wunch et al., 2011). The Karlsruhe instrument, in the following called HR125, is housed in an air-conditioned shipping container equipped with heating, ensuring constant temperature of the instrument throughout the year. This spectrometer is the first demonstration of synchronised recordings of TCCON and NDACC spectra using a dedicated dichroic beamsplitter arrangement (Optics Balzers Jena GmbH, Germany) with a cut-off wavenumber of 5250 cm^{-1} . It uses an indium gallium arsenide (InGaAs) detector in conjunction with an indium antimonide (InSb) detector, details can be found in (Kiel et al., 2016b). The TCCON HR125 measures a variety of atmospheric gases with reference accuracy. The heartpiece of the spectrometer is a cube-corner Michelson interferometer with a calcium fluoride (CaF_2) BS and a linearly moving scanner. The spectrometers line of sight is controlled by a camera-based solar tracker (Gisi et al., 2011). By the TCCON filters, the relevant wavenumber region 4000 - 11000 cm^{-1} is covered so that atmospheric gases like O_2 , CO_2 , CH_4 , CO and H_2O can be retrieved. The TCCON measurements were chosen as reference measurements because these gases are also measured by the EM27/SUN spectrometer. For TCCON measurements in the near infrared (NIR) the HR125 records single sided interferograms with a resolution of 0.014 cm^{-1} or 0.0075 cm^{-1} , corresponding to a maximum optical path difference of 64 cm and 120 cm. The recording time for a typical measurement consisting of two forward and two backward scans is 212 s, and 388 s, respectively. The applied scanner velocity is 20 kHz. The TCCON site Karlsruhe participated in the IMECC aircraft campaign (Messerschmidt et al., 2010; Geibel et al., 2012). The spectrometer has been used for calibrating all gas cells used by TCCON for instrumental line shape monitoring (Hase et al., 2013).

4.1.1 TCCON data analysis

TCCON data processing is performed using the GGG Suite software package (Wunch et al., 2011). In this study, the current release version, GGG 2014 is used (Wunch et al., 2015). The software package includes a pre-processor correcting for solar brightness fluctuations (Keppel-Aleks et al., 2007) and performing a fast Fourier transform including a phase error correction

Target gas	Spectral window [cm ⁻¹]
CO ₂	6180.0 - 6260.0
CO ₂	6297.0 - 6382.0
CH ₄	5880.0 - 5996.0
CH ₄	5996.4 - 6007.5
CH ₄	6007.0 - 6145.0
CO	4208.7 - 4257.3
CO	4262.0 - 4318.8

Table 4.1: Various target gases of the TCCON. In addition, the spectral windows are given.

routine to convert recorded interferograms into solar absorption spectra. It should be noted that forward and backward scans are split by the preprocessing software and analysed separately. The central part of the software package is the non-linear least-squares retrieval algorithm GFIT. It performs a scaling retrieval of an a priori profile, then integrates the scaled profile over height to calculate the total column of the gas of interest. The software package additionally uses meteorological data from the National Centers for Environmental Prediction (NCEP) and provides daily a priori gas profiles. All a priori profiles in GGG are generated by a set of empirical functions to optimise the fit to in situ measurements from various platforms, e.g. balloon-borne, AirCore, aircraft and satellites (Toon, 1991; Karion et al., 2010; Wofsy, 2011; Bernath et al., 2005). The empirical functions include a secular increase, interhemispheric gradient, seasonal cycle, and stratospheric decay based on the age of air. For CO₂, the a priori profiles are also based on the GLOBALVIEW data set (GLOBALVIEW-CO2, 2013). For H₂O, the a priori profiles are adopted from the National Center for Environmental Prediction analysis (Kalnay et al., 1996). For the creation of daily temperature and pressure profiles, the NCEP data product together with on site surface pressure is used. In case of the Karlsruhe site, ground pressure data are taken from a nearby meteorological tall tower with a height of 200 m. Starting from May 2017, ground pressure measurements from the German Weather Service station Karlsruhe-Rheinstetten are used¹.

TCCON uses the high-resolution transmission molecular absorption database HITRAN 2012 with empirical corrections for their retrieval (Toon, 2014). The corrections are based on laboratory and atmospheric spectra derived from FTS and balloon measurements (Wunch et al., 2010, 2015). In contrast to NDACC, TCCON uses wide spectral regions for the retrieval, opposed to narrow microwindows. This approach minimises temperature dependencies and reduces the noise error of the retrieved total columns because multiple lines contribute. A summary of the target gases and spectral regions is given in Table 4.1. H₂O is not shown, as it is retrieved from several narrow spectral windows.

In order to obtain accurate measurements, error sources have to be recognised and minimised. To achieve this, TCCON converts the retrieved total column abundances VC_{gas} of the measured gases into column-averaged dry air mole fractions (DMFs), where the DMF of a gas is denoted X_{gas} and calculated via:

$$X_{gas} = \frac{VC_{gas}}{VC_{dryair}} \quad (4.1)$$

Here VC_{dryair} is the total column of dry air. In the NIR, O₂ can be retrieved from the 7885 cm⁻¹

¹<https://www.dwd.de/DE/leistungen/beobachtung/beobachtung.html>

absorption band. As the ratio of O_2 in dry air is well known and constant, equation 4.1 can be written as:

$$X_{gas} = \frac{VC_{gas}}{VC_{O_2}} \cdot 0.2095 \quad (4.2)$$

In this representation, several error sources cancel out that affect both the target gas and O_2 . Furthermore, the dependence on the ground pressure is reduced improving comparability between different sites. However, residual bias with respect to in situ measurements still persists, as well as a residual spurious dependence of retrieval results on the apparent airmass. Therefore, the GGG suite also includes a post-processing routine applying an empirical airmass-dependent correction factor (ADCF) and an airmass-independent correction factor (AICF). The latter is deduced from comparisons with aircraft in situ measurements and ties the results to the World Meteorological Organization gas standard scale. The empirical ADCF is introduced because for most gases, X_{gas} retrieved from remote sensing exhibit a slight airmass dependent, systematic symmetric variability. This artefact is probably due to spectroscopic inadequacies, incorrect a priori gas profiles and instrumental issues.

4.1.2 HR125 low resolution data analysis

In addition to the afore mentioned TCCON data product, a second data product from the HR125 will be deployed in this thesis, in the following called HR125 LR. For this product the raw interferograms are first truncated to the resolution of the EM27/SUN, 0.5 cm^{-1} . At 0.5 cm^{-1} resolution, the ILS of the HR125 is expected to be nearly nominal. However, to avoid any systematic bias of the HR125 LR data with respect to the EM27/SUN results, the same procedure for ILS determination from H_2O signatures in open path lab air spectra was applied and the resulting ILS parameters adopted for the trace gas analysis. The analysis procedure will be explained in detail in section 4.2.3. The reason for the construction of this HR125 LR data set is that with this approach the analysis for the two instruments can be performed in exactly the same way. The resolution is harmonised, so the averaging kernels for a given airmass are nearly identical. Differences between the EM27/SUN and the HR125 LR data set can then be attributed to instrumental features alone and do not need to be disentangled from retrieval software, resolution and airmass dependent differences. Note that for the low resolution data set, forward and backward scans are averaged and then analysed whereas they are analysed separately for the TCCON data set. Therefore, number of coincident measurements with the EM27/SUN data set compared to the TCCON data set is lower.

4.2 The Bruker EM27/SUN mobile spectrometer

The EM27/SUN spectrometer from KIT, which was developed in collaboration with Bruker OpticsTM, is utilised for the acquisition of solar spectra. The central part of this Fourier transform spectrometer, which is depicted in Figure 4.1, is a RockSolidTM pendulum interferometer with 2 cube corner mirrors and a Quartz beamsplitter. The compensated BS design minimises the curvature in the phase spectrum. This setup achieves high stability against thermal influences and vibrations. The retroreflectors are gimbal-mounted, which results in frictionless and wear-free movement. In this aspect, the EM27/SUN is more stable than the HR125 high resolution FTS, which suffers from wear because of the use of friction bearings on the moving retroreflector. Over time this leads to shear misalignment and requires regular realignment (Hase, 2012). The gimbal-mounted retroreflectors move a geometrical distance of 0.45 cm

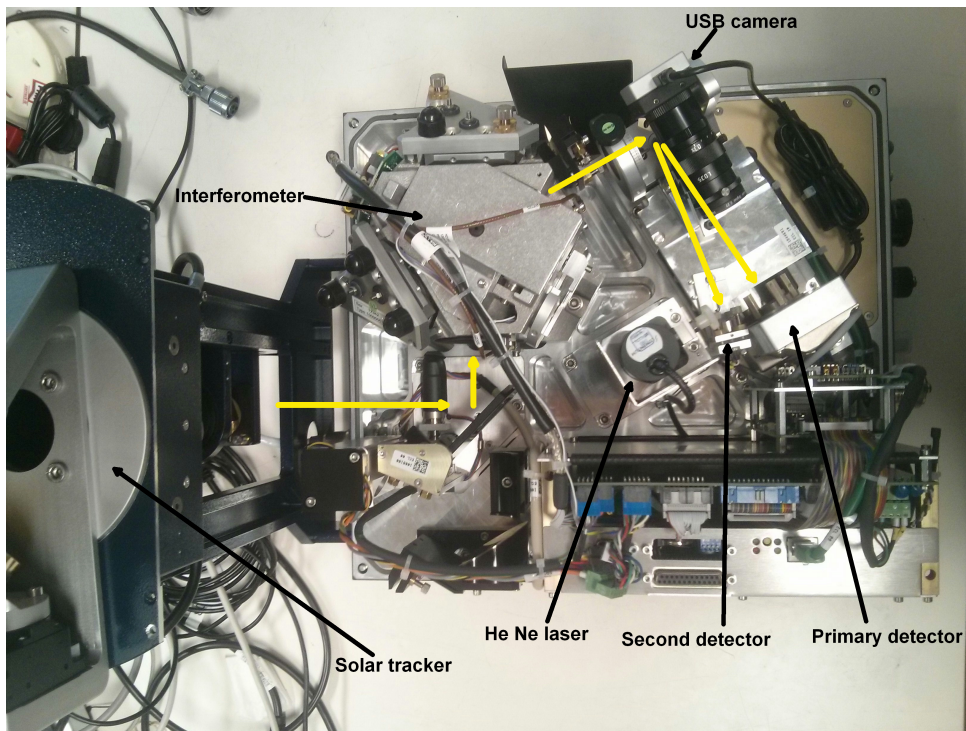


Figure 4.1: Inner body of the EM27/SUN spectrometer. Yellow arrows denote the light path. This EM27/SUN is equipped with a second channel for CO observations (Hase et al., 2016).

against each other leading to an optical path difference of 1.8 cm which corresponds to a spectral resolution of 0.5 cm^{-1} . The EM27/SUN routinely records double-sided interferograms. A standard, not frequency stabilised HeNe laser controls the sampling of the interferogram. The spectrometer is sealed and contains a desiccant cartridge. It can withstand harsh environmental conditions, such as high humidity, while operating outside. The spectrometer weighs approximately 25 kg including a miniature version of the camtracker (Gisi et al., 2011). The dimensions are $35 \times 40 \times 27 \text{ cm}$, so it can be carried by one person.

The yellow arrows in Figure 4.1 indicate the solar light path inside the spectrometer. The solar radiation is led into the spectrometer by the tracker. The collimated beam of 25 mm diameter enters through the wedged entrance window, which acts as a long-pass-filter, filtering out radiation below 750 nm in order to block stray light on the detectors, and is tilted against the optical axis to avoid channelling. The beam enters the interferometer, where a CaF_2 beamsplitter splits the light beam into two parts. The two parts are reflected back by two cube corner mirrors. After recombination, the modulated radiation exits the interferometer and is blocked by an aperture with a diameter of $\approx 5 \text{ mm}$. This aperture is introduced to avoid non-linear detector response and to control optical aberrations. The remaining radiation is focused on the 0.6 mm field stop by a 90° off-axis paraboloid mirror with a focal length of 127 mm. This leads to a semi field of view of 2.36 mrad which corresponds to 56 % of the mean solar disk diameter. To avoid channelling, the field stop aperture is tilted against the optical axis. Behind it a diffusor is placed to minimise channelling and non-linearity effects. Directly behind the diffusor the InGaAs detector is located, consisting of a photodiode from Hamamatsu with a size of $1 \text{ mm} \times 1 \text{ mm}$ and spectral sensitivity between $5000 - 11000 \text{ cm}^{-1}$. The detector is DC-coupled and thereby supports the correction of variable atmospheric transmission (Keppel-Aleks et al., 2007). The covered spectral range allows the deduction of trace gas abundances of CO_2 , CH_4 , H_2O and O_2 .

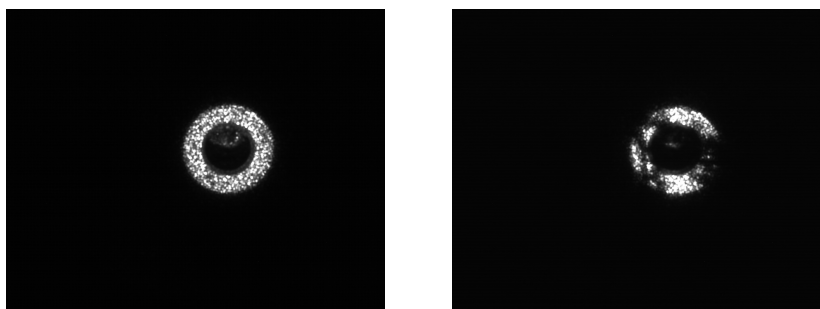


Figure 4.2: Images of the solar disk on the aperture of the EM27/SUN for a scene with clear sky (left panel) and trees in the line of sight (right panel). The CamTracker program has no difficulty to focus the Sun.

A camera is used for precise control of the line of sight of the spectrometer (Gisi et al., 2011). Figure 4.2 shows an image of the Sun on the aperture for an unobstructed view and a scene where the Sun is covered by trees.

In the course of this PhD thesis an extension to the described standard EM27/SUN setup was tested. A second detector was inserted into the spectrometer, see Figure 4.1, and part of the solar beam is led to this second extended InGaAs detector which expands the measurable range to the 4000 cm^{-1} region. This upgrade enables the detection of carbon monoxide. Details can be found in Hase et al. (2016). The extension is now sold by Bruker Optics as a regular upgrade and is in wide use in the EM27/SUN FTIR community.

4.2.1 Instrumental improvements

In the course of this thesis, 30 EM27/SUN spectrometers were checked at KIT. In the following section, diagnosed and corrected detrimental effects are described.

Ghost to parent ratio

The EM27/SUN records spectra in the region from 100 cm^{-1} to 15798 cm^{-1} . In order to satisfy the Nyquist theorem the sampling of the interferogram has to be performed at every zerocrossing of the laser AC interferograms (HeNe laser, wavelength 633 nm). If the sampling is not performed exactly at the zerocrossing, systematic sampling errors are introduced leading to artefacts in the measured spectrum, so called sampling ghosts (Messerschmidt et al., 2010; Dohe et al., 2013). These artefacts are superimposed on the real spectrum and appear at the wavenumber position of the high-folding limit (15798 cm^{-1}) minus the wavenumber position of the original spectrum. Therefore, the sampling ghost is reversed with respect to the original spectrum. The manufacturer recently released an effective workaround for this problem which was adopted for our measurements. A temporal linear interpolation is applied for calculating the downward zero crossing positions. This method suppresses the ghosts below the detection limit ($< 5 \times 10^{-6}$), see Figure 4.3. In the left panel the original spectrum is shown, a narrow band pass filter centred at 6000 cm^{-1} was applied. The ghost is too small to be seen. In the right panel the effect of the interpolation scheme is shown. The black line shows the ghost, appearing at approximately 15798 cm^{-1} minus 6000 cm^{-1} wavenumbers. With the interpolation scheme activated, the ghost disappears. In addition, this set up was tested for possible line shape errors and other kinds of out-of-band artefacts, but no detrimental effects were found.

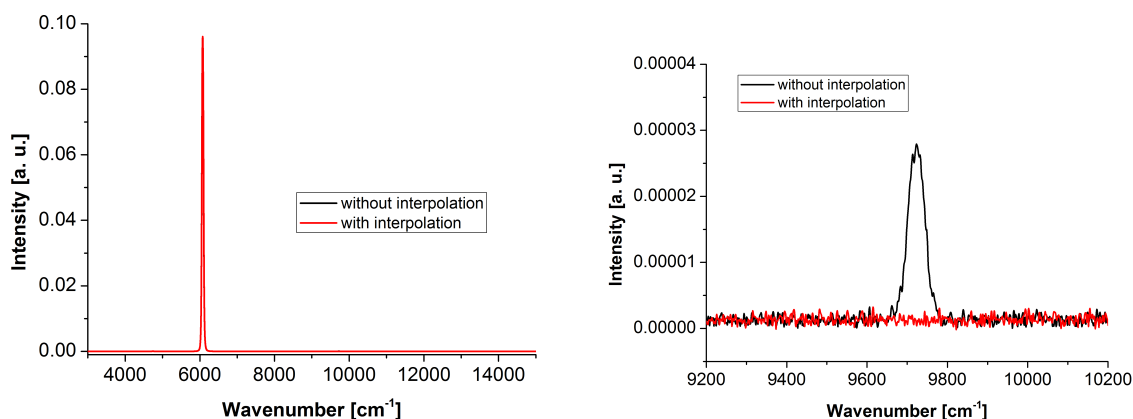


Figure 4.3: The left panel depicts the spectral range of a lamp measurement, where a narrow band-pass was put in front of the detector. The right panel shows a zoom into the region where the ghost appears. It is apparent that with the interpolation scheme the sampling ghost artefact disappears.

Double passing

Another detrimental effect in FTIR spectroscopy is double passing. The modulated light beam is reflected from a component behind the interferometer and passes through the spectrometer a second time. It is again reflected at the entrance window of the EM27/SUN and then reaches the detector. Although this effect does not directly affect the retrieval in case of the EM27/SUN as the double passing appears at double wavenumber with respect to the original spectrum, it can and should be corrected as it allows to detect other kinds of out-of-band artefacts. To avoid double passing the entrance window has to be tilted against the optical axis. An example is shown in Figure 4.4. The left panel shows the original spectrum before and after the entrance window was tilted against the optical axis. In the right panel, a zoom into the region where the double passing appears is shown. The far wing of the original spectrum covers the beginning of the double passing (black curve), for higher wavenumbers the structure of the original spectrum is apparent. After the correction the double passing is suppressed below the detection limit (red line).

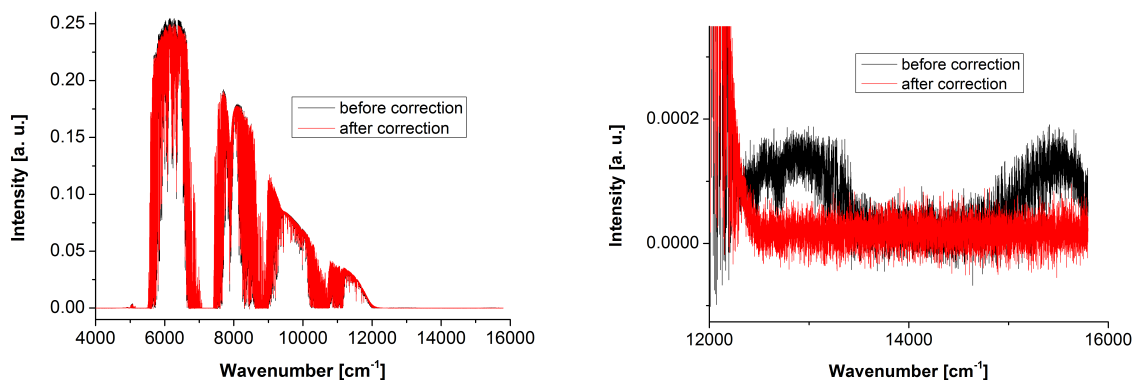


Figure 4.4: In the left panel a typical atmospheric measurement is depicted. The right panel shows a zoom into the region where the double passing occurs. The black line was measured before the correction. The structure of the original spectrum is clearly visible, the beginning of the double passing is overlaid by the far wing of the original spectrum. The red curve does not show any double passing.

Channelling

Channelling is a delicate detrimental effect caused by interference at surfaces in optical elements. In atmospheric spectra it is hard to identify as it is a small modulation overlying the measured spectrum and masked by the changing intensity due to absorption features. Therefore, to diagnose channelling, open path lamp measurements are utilised. Channelling frequency and amplitude are wavenumber dependent, generally more pronounced in the mid infrared part of the spectrum. To identify channelling, apart from extreme cases where it is directly visible, a large number of spectra (~ 30) have to be averaged. From the channelling frequency $\Delta\nu$ the thickness d of the optical part producing the channelling can be identified via $\Delta\nu = \frac{1}{2nd}$, where n is the refractive index of the medium. Using this diagnostic, surfaces responsible for channelling could be identified, for example the glass of the lamp used for the open path measurements. In this particular case, it could be corrected by tilting the light bulb against the optical axis and by roughening the surface of the light bulb. The detector element was also identified as a potential source for channelling in the mid infrared. This is shown in the left panel of Figure 4.5. Depicted are lamp measurements from the extended InGaAs detector in the 4300 cm^{-1} wavenumber region for different EM27/SUN spectrometers. In contrast to the prototype setup, some recently upgraded EM27/SUN show channelling (SN 33) with a frequency of 4.3 cm^{-1} while others are free of channelling (SN 46). Subsequent tests revealed that this channelling affects the CO measurements of the EM27/SUN, which are evaluated in the $4200 - 4318\text{ cm}^{-1}$ region. An extreme example is shown in the right panel of Figure 4.5. The shape of the measurements from instrument SN 33 is distorted with respect to the other EM27/SUN as well as a reference high resolution spectrometer measuring at the resolution of the EM27/SUN. Attempts were undertaken to correct this artefact. As it is restricted by the instrument geometry, tilting of the whole detector element will modify the channelling. A final solution to this problem is under investigation but still pending, these findings were also reported to the manufacturer.

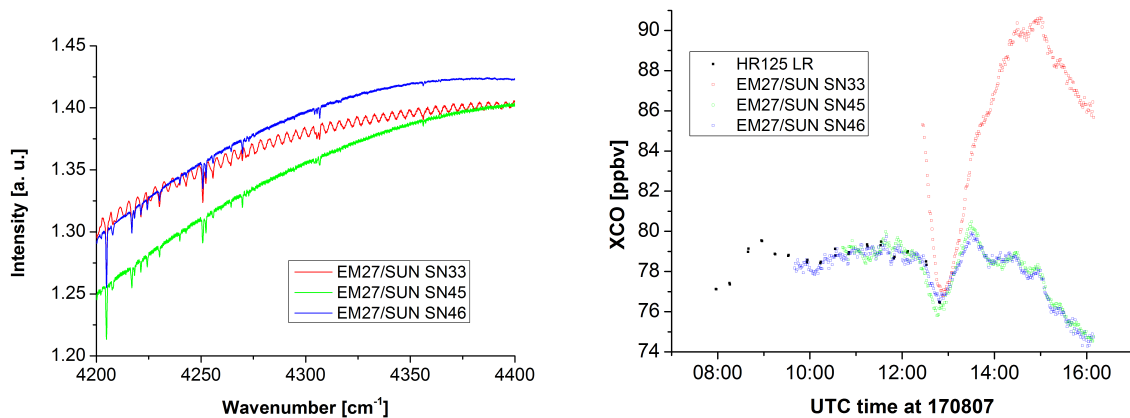


Figure 4.5: The left panel shows open path measurements for three EM27/SUN in the 4300 cm^{-1} wavenumber region. Instrument SN 33 exhibits strong channelling with a channelling frequency of 4.3 cm^{-1} . In the right panel column averaged dry air mole fractions of CO are depicted for the three EM27/SUN as well as the reference high resolution spectrometer, with measurements taken at the resolution of the EM27/SUN. The shape of the XCO time series of instrument SN33 is distorted with respect to the other instruments.

4.2.2 Instrumental line shape

Accurate knowledge of a spectrometer's instrumental line shape is extremely important to gain correct information from measurements because using wrong ILS values leads to systematic errors in the gas retrieval. The ILS can be divided into two parts. One part describes the modulation loss through inherent self-apodisation of the spectrometer which is present also in an ideal instrument. This contribution can easily be calculated utilising the OPD and FOV of the spectrometer, see section 2.4. The other component of the ILS results from misalignments and optical aberrations of each individual spectrometer and can be characterised by a modulation efficiency amplitude and a phase error, both functions of the optical path difference (Hase et al., 1999). These parameters have to be deduced from lab measurements.

Here an ILS characterisation scheme for the EM27/SUN is implemented. Whereas for TCCON spectrometers the standard procedure to derive the ILS are low pressure gas cell measurements, this proposed approach uses an open-path observation of a few meters of lab air to avoid the need for a gas cell, only an external light source is required. The ILS is derived from H_2O lines in the $7000 - 7400 \text{ cm}^{-1}$ spectral region. The selected microwindow encompasses a large number of water vapour lines spanning a wide range of line intensities. Residuals of spectral fits to fully resolved open path spectra collected with the TCCON spectrometer were used to verify that the selected microwindow does not contain lines with significantly inconsistent line parameters.

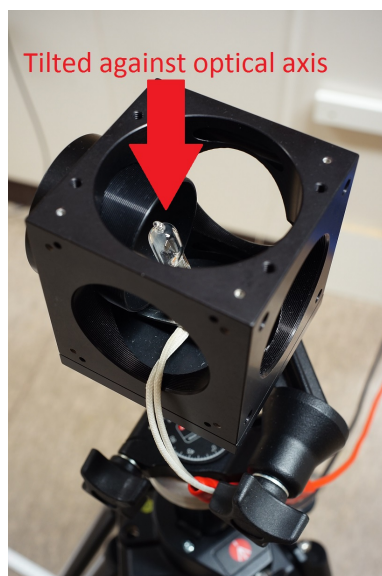


Figure 4.6: Setup of the lamp system. The bulb is tilted against the optical axis to avoid channelling. The lamp system is mounted on a height-adjustable tripod for the fine adjustment of the light beam.

Fig. 4.6 shows a picture of the lamp setup. An OsramTM Halogen 50 W lamp as radiation source is deployed, together with a fast aspherical collimation lens of 2 inches diameter, as used in projection collimators. In order to avoid channelling the light bulb was tilted with respect to the optical axis, and for assuring a uniform illumination the glass surface of the bulb was roughened towards the lens by use of a piece of sandpaper. This is also useful to further suppress channelling. The system was mounted on a stable, height-adjustable tripod because this much alleviates the fine adjustment for achieving a uniform light beam on the tracker mirror and a uniform image of the source on the field stop. Due to the modification of the bulb a voltage lower than the nominal voltage should be applied for operation. A stabilised digital laboratory DC power supply was used, a voltage of 11 V was applied. Two hours prior to the actual measurements the instrument was powered up to guarantee that the non-stabilised reference laser operates at a constant wavelength. As the water column inside the spectrometer cannot be neglected, the instrument was vented by opening the two apertures of the spectrometer, in

order to ensure that the mixing ratio of water vapour is about the same inside and outside the spectrometer. The apertures were opened when the instrument was switched on and closed after recording of the spectra. Out of the dependence of stable thermal conditions and because of the temporal violation of the sealed spectrometer closure, it is recommended to apply this procedure only in a reasonably clean, controlled environment. It is mandatory not to open the spectrometer apertures if the humidity in the room is too high or if the instrument is colder than the surrounding because of the risk of condensation. The distance between instrument and lamp should not be chosen too small, because otherwise the heat of the lamp will affect a non-negligible section of the open path, thus introducing a systematic error. Furthermore, care should be taken that the free aperture of the tracker is fully illuminated and that the image of the lamp on the field stop is evenly illuminated and exceeds the diameter of the field stop. This can be achieved by shifting and tilting the source and by rotating the mirrors of the solar tracker using its internal camera. The resulting illumination on the field stop aperture can also be comfortably judged using this camera.

For the measurements themselves 30 times 10 double-sided scans at 0.5 cm^{-1} resolution were recorded. The settings in the measurement file are the same as for solar measurements except that the the highest pregain setting was used. The final spectrum used in the subsequent analysis was obtained by taking the averaged interferogram, performing a DC-correction and a Fourier transformation. The DC correction is important to be consistent with the atmospheric spectra. Omitting the DC correction for the open path measurements would thereby lead to systematic errors in the retrieved ILS. In order to predict the correct width of the observed H_2O lines and so correctly retrieve the ILS width, the distance between instrument, measured from the first tracking mirror, and lamp needs to be measured. Furthermore, air temperature and pressure at the time of measurement need to be taken into account. In this setup, temperature and pressure were recorded using a Lutron MHB-382SD data logger with a temperature accuracy of $\pm 0.8^\circ \text{ C}$ and pressure accuracy of $\pm 3 \text{ hPa}$ (above 1000 hPa) or $\pm 2 \text{ hPa}$ (below 1000 hPa). The optical path length between first tracking mirror and the longpass filter plus the distance between light bulb and collimation lens is identical for all EM27/SUN spectrometers (43 cm) as well as the path length inside the spectrometer housing (58 cm). These contributions have to be added to the aforementioned distance of a few meters.

For the analysis of the measured lab spectra, the retrieval software LINEFIT Version 14.5 (Hase et al., 1999) was used. As the ILS characteristics were close to nominal, the simple two-parameter ILS model was applied. For the H_2O linelist the HITRAN 2009 linelist with minor adjustments was used, see Sect. 4.2.3. A preliminary LINEFIT analysis run on the measured spectrum was performed in order to determine the H_2O column. From this H_2O column value, the total path length, and the temperature, the partial pressure of H_2O was calculated. This value was afterwards used for the final LINEFIT run, which provided the ILS parameters. A typical fit result is shown in Fig. 4.7. The standard deviation of the residual is $1\sigma = 0.24 \%$.

For providing a demonstration of the level of reliability of the procedure, ILS parameters from spectra recorded at several different distances were determined. The results are depicted in Fig. 4.8, applying two different ways of performing the analysis. The simple analysis assumes a uniform path between lamp and detector. The more refined approach divides the observed absorption into two contributions, one from inside and one from outside the spectrometer. It is assumed that due to the venting, the mixing ratio of H_2O inside the spectrometer is the same as outside, but it is taken into account that the air inside the spectrometer is slightly warmer due to power dissipation of the spectrometer. Temperature inside the spectrometer is recorded by a sensor provided in the housekeeping data of each OPUS file. As indicated by Fig. 4.8, both results are in agreement within 0.2 %. It is recommended to follow the refined procedure which is probably more accurate. Note that the deduced ILS parameters are also consistent with

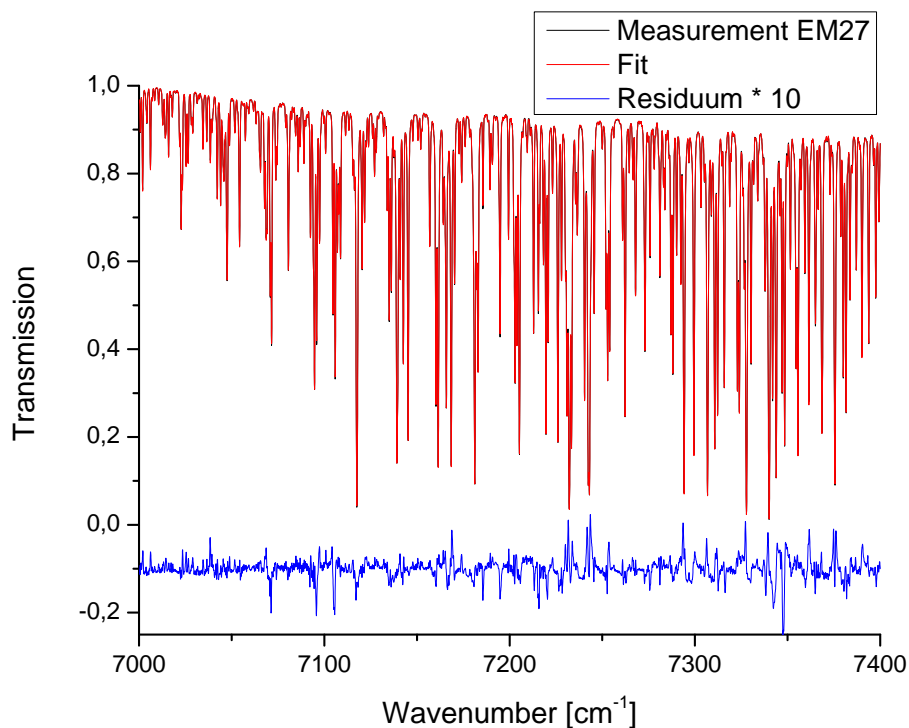


Figure 4.7: Transmission spectrum of 4 m lab air (black curve) in the 7000 - 7400 cm^{-1} region. Overlaid is the LINEFIT calculation (red curve). The residuum multiplied by a factor of ten is shown in blue. For clarity reasons, an offset of -0.1 was added to the residuum.

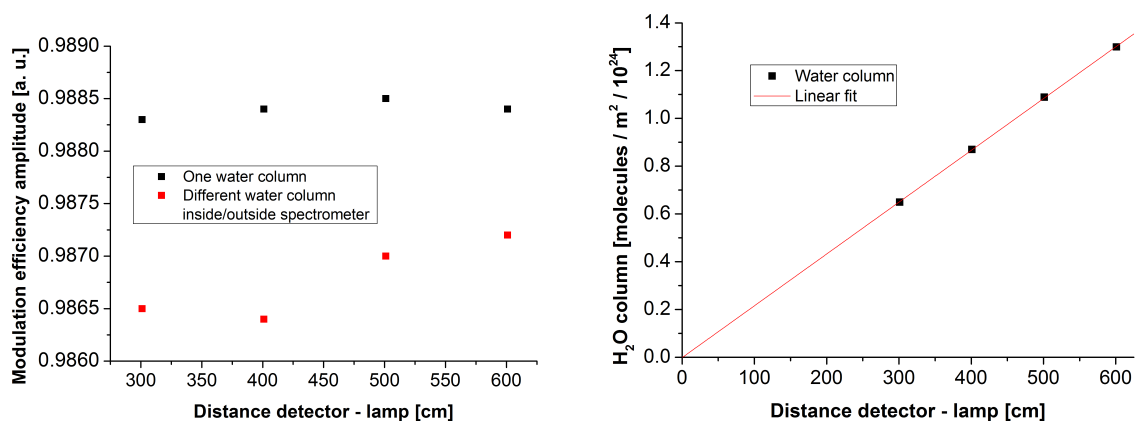


Figure 4.8: The left panel shows modulation efficiencies obtained with LINEFIT for two different ways of performing the analysis. The simple analysis assumes an uniform path between lamp and detector, whereas the more refined approach divides the observed absorption into two contributions, one from inside and one from outside the spectrometer. Results are in agreement within 0.2 %. The right panel shows the calculated water vapour column, a side product of the ILS analysis, as a function of the distance between lamp and detector.

Error source	uncertainty	propagation on ME
Temperature	± 0.8 K	-0.16 %
Total pressure	± 3 mbar	0.19 %
Distance	± 5 cm	-0.04 %
Partial pressure H ₂ O	± 0.5 mbar	0.13 %
Measurement noise		0.05 %
Total		0.29 %

Table 4.2: Estimated uncertainties for various assumed error sources.

changing distance between source and spectrometer. This is also emphasised in the right panel of Figure 4.8, where the calculated water vapour column, a side product of the ILS analysis, scales linearly with distance between lamp and detector.

An error estimation for the open path measurements is given in Table 4.2. For the temperature and pressure error, the stated accuracies of the data logger manufacturer were used. For the other potential error sources reasonable assumptions were made. The total error, given by the root-squares-sum of the individual errors, is 0.29 % in ME amplitude, consisting of several errors of approximately the same magnitude.

For the given example the modulation efficiency at MOPD is significantly lower than nominal. This finding is also true for most other EM27/SUN spectrometer as will be shown in section 5.2, which is surprising as great care was taken to align the instrument. Therefore, lamp measurements were also performed for the HR125 at a resolution of 0.5 cm^{-1} to investigate whether this method shows a bias. For this small optical path difference, the HR125 should be perfectly aligned. However, the LINEFIT analysis shows a ME of 0.9824 at MOPD. From this result it is concluded that this method shows an overall low bias of around 1.5 %.

The ILS analysis will be revisited in the following chapters. The long term stability, ensemble spread and ILS stability before and after campaign use of the EM27/SUN will be investigated.

4.2.3 Retrieval software and processing

In a first step, a solar brightness fluctuation correction is performed similar to Keppel-Aleks et al. (2007). Furthermore, the recorded interferograms are Fourier transformed using the Norton-Beer-Medium apodisation function (Davis et al., 2010). This apodisation is useful for reducing sidelobes around the spectral lines, an undesired feature in unapodised low resolution spectra, which would complicate the further analysis. Together with a quality control, which filters interferograms with intensity fluctuations above 10 % and intensities below 10 % of the maximal modulation amplitude, this is implemented in a Python tool.

In this work, spectra were analysed utilising the PROFFIT Version 9.6, a non-linear least-squares spectral fitting algorithm (Hase et al., 2004). This code is in wide use and has been thoroughly tested in the past for the HR125 as well as the EM27/SUN (e.g. Schneider and Hase (2009); Sepúlveda et al. (2012); Kiel et al. (2016a); Chen et al. (2016)). Due to the low resolution of the EM27/SUN, the atmospheric spectra were fitted by scaling of a priori trace gas profiles, although PROFFIT has the ability to perform a full profile retrieval (Dohe, 2013). As source of the a priori profiles, the TCCON daily profiles introduced in section 4.1.1 are utilised to be consistent with the TCCON analysis. For the daily temperature and pressure profiles, the approach from TCCON was also adopted, using NCEP model data together with on site ground pressure data from a meteorological tall tower².

²www.imk.kit.edu/messmast/

Every retrieval depends on the choice of line lists for the solar lines and atmospheric gases absorption lines. The HITRAN 2008 line list in its original form is used for CH₄, the HITRAN 2008 line list with a line-mixing parameterisation for CO₂ adopted from a code provided by Lamouroux et al. (2010) and the line list used by TCCON for O₂. For the H₂O line list the HITRAN 2009 line list was used with changes introduced by Toon (2014) and additional ad hoc adjustments where it seemed appropriate. A solar list was derived from ACE-FTS and ground-based Izana atmospheric spectra.

For the evaluation of the O₂ gas column the 7765 - 8005 cm⁻¹ spectral region is used, which is also applied in the TCCON analysis (Wunch et al., 2010). For CO₂ the spectral windows used by TCCON are combined to one larger window ranging from 6173 - 6390 cm⁻¹. CH₄ is evaluated in the 5897 - 6145 cm⁻¹ spectral domain. For H₂O the 8353 - 8463 cm⁻¹ region is used. This is in contrast to TCCON, deploying several narrow spectral windows. An example fit for the different spectral windows is shown in Fig. 4.9. The residual of the spectral fit for the water column retrieval is high compared to the other gases because of the difficulties in measuring H₂O line parameters. The standard deviation of the residual is $\sigma = 0.2\%$ for CO₂ and CH₄, $\sigma = 0.1\%$ for O₂ and $\sigma = 0.5\%$ for H₂O.

For consistency reasons, and to reference the results to the WMO scale, the EM27/SUN retrieval also includes a post-processing. The AICF from TCCON is adopted, and similar to Wunch et al. (2010), an airmass dependency correction of the form

$$Xgas_c = Xgas_{unc} \left\{ 1 + a \left[\left(\frac{\theta + b}{90^\circ + b} \right)^2 - \left(\frac{45^\circ + b}{90^\circ + b} \right)^2 \right] \right\} \quad (4.3)$$

is used, where a , b are fit parameters, θ is the solar zenith angle (SZA), $Xgas_c$ and $Xgas_{unc}$ are the airmass dependency corrected and uncorrected column-averaged DMF of the respective species. Wunch et al. (2010) use TCCON data from North American sites to derive correction factors. Since it is expected that the correction factors differ due to the differing spectral resolution of TCCON and EM27/SUN and different radiative transfer models, the factors were derived by a different approach. The data recorded at Karlsruhe are not well suited to correct the airmass dependency due to actual intraday variability, as the site is situated near a medium sized city, and several power plants are in the region. Instead parameters obtained from a comprehensive evaluation of EM27/SUN data recorded during a campaign on a research vessel (Klappenbach et al., 2015) are used. These data are not influenced by local source contributions and clearly show an SZA dependency in the XCO₂ and XCH₄ data, even though for the CO₂, CH₄ and H₂O a priori profiles, CAMS model data was used (Agustí-Panareda et al., 2014; Massart et al., 2014). For these measurements the O₂ column does not show a detectable SZA dependency for SZA below 80°; the SZA dependency is essentially generated by the CO₂ and CH₄ columns in the numerator. The obtained parameters are $a = 6.296 \cdot 10^{-3}$, $b = 1.291$ for XCO₂ and $a = 3.796 \cdot 10^{-3}$, $b = 16.04$ for XCH₄. To tie the results to the TCCON scale, a global calibration factor between EM27/SUN and TCCON is calculated, which will be shown in section 5.1.

4.2.4 Measurement routine

Over the last years, regular measurements with an EM27/SUN (SN 37), from here on called reference EM27/SUN, have been performed on a terrace on the top floor of the IMK-ASF, building 435 KIT CN, with an altitude of 133 m a.s.l., coordinates are 49.094° N and 8.436° E. The spectrometer was moved from the lab on the fourth floor to the roof terrace on the seventh floor thus being exposed to mechanical and thermal stress. The instrument was coarsely oriented

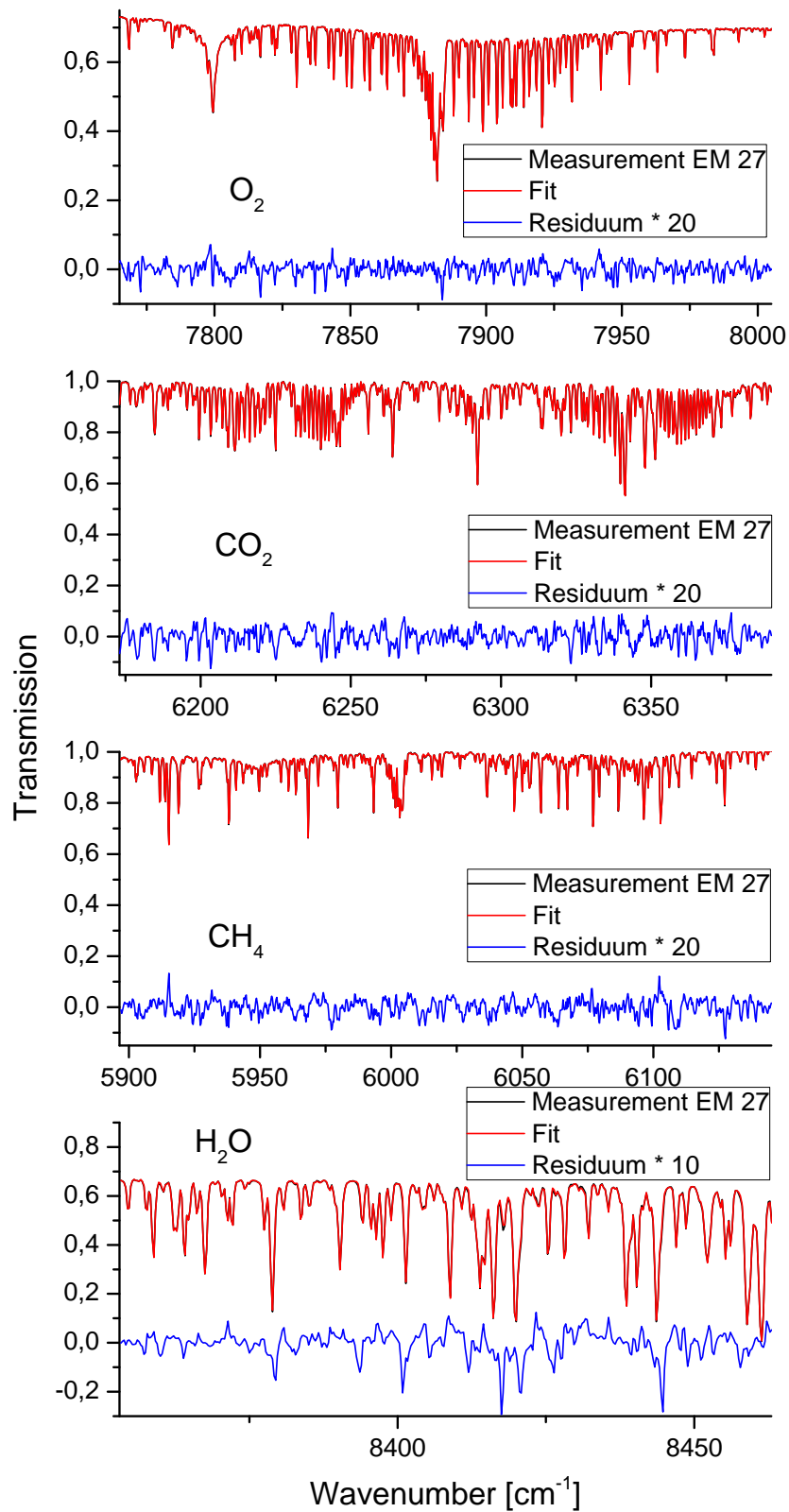


Figure 4.9: Spectral windows used during the retrieval for the different species. The fit is in accordance with the measurement. The residual has been multiplied with a factor of 10 for H₂O and 20 for the other species.



Figure 4.10: Calibration measurements performed prior to a campaign on top of the KIT - IMK office building North of Karlsruhe. The instrument in the middle shows a sun cover. Photograph courtesy of F. Hase.

north, without effort for levelling. If further orientation was needed, the spectrometer was manually rotated so that the solar beam was centred onto the entrance window. The CamTracker program was then able to track the sun. As the EM27/SUN was operated in summer, it heated up to temperatures above 40°C . In order to protect the electronics from the heat, a sun cover for the EM27/SUN was built, which reduced the temperatures inside the spectrometer by about 10°C . In winter the temperatures were as low as -4°C at the start of measurements. Double-sided interferograms with 0.5 cm^{-1} resolution were recorded. With 10 scans and a scanner velocity of 10 kHz , one measurement takes about 58 s. For precise time recording, a GPS receiver was used.

30 different EM27/SUN were calibrated at KIT in the last years. For the calibration procedure, measurements together with the reference EM27/SUN were performed. A picture of a typical calibration day before campaign deployment is shown in Fig. 4.10.

Chapter 5

EM27/SUN long term stability and ensemble performance

Precise measurements of atmospheric quantities of greenhouse gases, especially CO₂ and CH₄ are of utmost importance for the estimation of emission strengths and flux changes (Olsen and Randerson, 2004). Furthermore, these measurements can be directly used to evaluate emissions reductions as demanded by international treaties, e.g. the Paris COP21 agreement. The TCCON network measures total columns of carbon dioxide and methane with reference precision (Wunch et al., 2011). However, the instruments used by this network are rather expensive and need large infrastructure to be set up and expert maintainance. Therefore, TCCON stations have sparse global coverage, especially in Africa, South America and large parts of Asia (Wunch et al., 2015). Current satellites like the Orbiting Carbon Observatory-2 (OCO-2) (Frankenberg et al., 2015) and the Greenhouse Gases Observing Satellite (GOSAT) (Morino et al., 2011) offer global coverage. Nonetheless, they suffer from coarse temporal resolution (the repeat cycle of OCO-2 is 16 days), and in the case of GOSAT from sparse spatial sampling as well as limited precision of a single measurement. These limitations mostly inhibit a straightforward estimation of the emission strength of localised sources of CO₂ and CH₄ like cities, landfills, swamps or fracking and mining areas from satellite observations. However, recently OCO-2 data was used for estimating the source strength of large power plants (Nassar et al., 2017).

The previously described EM27/SUN portable FTIR spectrometer is a promising instrument to overcome the above mentioned shortcomings as it is a mobile, easy to deploy and low-cost supplement to the Bruker IFS 125HR spectrometer used in the TCCON network. In this chapter, the long term performance of the EM27/SUN with respect to a reference high resolution TCCON instrument is investigated. Additionally, the ensemble performance of several EM27/SUN spectrometers is tested. From 2014 to 2018, 30 EM27/SUN were calibrated at KIT before being shipped to the operators. Several instruments that were distributed before this calibration routine at KIT was established, were upgraded with a second channel for CO observations at Bruker OpticsTM and after this were also calibrated at KIT. This results in a unique data set as all EM27/SUN are directly calibrated with respect to a reference EM27/SUN, continuously operated at KIT, as well as a co-located TCCON instrument. From this data set an EM27/SUN network precision and accuracy can be estimated.

The results presented here have recently been published as Frey et al. (2018), from which this chapter is mainly adopted from.

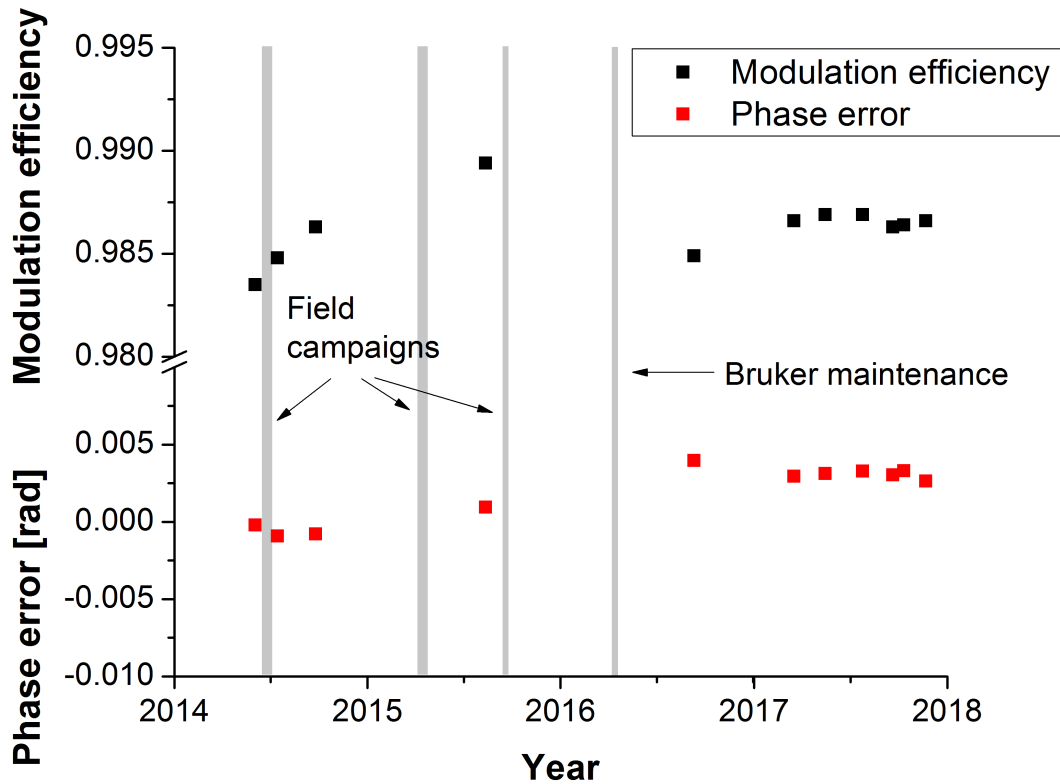


Figure 5.1: ILS time series of the reference EM27/SUN. Results for modulation efficiency and phase error were obtained with LINEFIT 14.5. The mean value of the modulation efficiency is 0.9862 with a standard deviation of 0.0015. For the phase error an average value of 0.0019 ± 0.0018 is found. As can be seen from the closely spaced measurements in 2017, there is no seasonality in the ILS values. Grey areas denote periods of transportation of the instrument.

5.1 Long term performance

Here the long term stability of an EM27/SUN is investigated with respect to a HR125 spectrometer. The methods used in this analysis have been outlined in chapter 4.2.2 and 4.2.3.

5.1.1 ILS analysis

Accurate knowledge of the real ILS of a spectrometer is important as errors in the ILS lead to systematic errors in the trace gas retrieval. For this reason, regular ILS measurements were performed from the beginning of this PhD thesis to detect possible misalignments and alignment drifts. Source of a loss of adjustment is mostly mechanical strain, due to e.g. impacts or vibrations especially due to transportation of the instruments. The time series of the ILS measurements is shown in Figure 5.1. The modulation efficiency at MOPD is close to nominal at all times with values between 0.9835 and 0.9896, a mean value of 0.9862 and a standard deviation of 0.0015. The phase error is close to zero for the whole time series with a mean value of 0.0019 ± 0.0018 .

There is no overall trend apparent in the time series, the remaining differences in the modulation efficiency are probably due to the remaining uncertainty of the measurement technique. As is apparent from the more frequent measurements in 2017, there is also no seasonality in the modulation efficiency. Furthermore, it should be noted that the measurement routine was refined in the course of the thesis. In particular, in the beginning (2014) it was assumed that the inside

of the EM27/SUN is free of water vapour, so the instrument was not vented during the lamp measurements. However, sensitivity studies as presented in Frey et al. (2015) revealed that the influence of the water vapour column inside of the spectrometer cannot always be neglected. This is why the 2014 measurements show larger scatter, as here the amount of water vapour inside the spectrometer is not known. For this analysis, it was assumed that also for the 2014 measurements the total pressure inside the spectrometer is the same as of the surrounding air, which is a sensible assumption as the spectrometer is not evacuated. This explains also that the deviations become smaller in 2017. A further test to verify the stability of the instrument is the X_{air} parameter, which is the surface pressure divided by the measured column of air. This test will be described in section 5.1.3.

The grey lines denote transportation of the spectrometer over longer distances for field campaigns in Berlin (North-Eastern Germany), Oldenburg (Northern Germany) and Paris (France) and for maintenance at Bruker Optics. Note that no realignment of the interferometer was performed during this maintenance. Only the reference HeNe laser was exchanged due to sampling instabilities during interferogram recordings. More specific, the laser wavelength was unstable resulting in a corruption of parts of the measured spectra. The reason this instrument was not used for campaigns in 2016 and 2017 is that it was chosen as the reference EM27/SUN for comparison measurements with the HR125 spectrometer in order to take measurements at Karlsruhe as frequently as possible. The instrument was not realigned during the whole comparison study of 3.5 years.

5.1.2 Total column time series

In this section, the total column measurements from the EM27/SUN are compared to the reference HR125 spectrometer. For the measurements, the EM27/SUN was moved to a terrace on the top floor of the IMK-ASF, building 435 KIT Campus North (49.094° N, 8.436° E), on a daily basis if weather conditions were favourable. For the HR125 spectrometer two data products are discussed, the official TCCON product (Wunch et al., 2011; Kiel et al., 2016b) at 0.02 cm⁻¹ resolution where only data points with a 0 quality flag are used, and a truncated 0.5 cm⁻¹ resolution product (HR125 LR), which was analysed like the EM27/SUN measurements, see section 4.2.3. For this data product lamp measurements as described in section 4.2.2 were conducted to retrieve the ILS of the HR125. The full time series from March 2014 to November 2017 is shown in Figure 5.2. For better visibility only coincident data points measured within one minute between EM27/SUN and the other data sets are shown. There are 8349 paired measurements between EM27/SUN and TCCON and 4624 between EM27/SUN and HR125 LR. This is only a small subset of the overall data sets, in total there are 50550 EM27/SUN and 25361 TCCON measurements.

All species show a pronounced seasonal cycle, where the variability in water vapour is strongest with values below 1×10^{26} molc m⁻² in winter and up to 14×10^{26} molc m⁻² in summer. Furthermore, the seasonal cycle of water vapour is shifted with respect to the other species. Another feature seen is that there is an offset in the EM27/SUN (red squares) and HR125 LR (blue squares) total column data with respect to the TCCON data (black squares). This is a feature commonly observed when drastically reducing the resolution (Petri et al., 2012; Gisi et al., 2012). The observed offset between EM27/SUN and HR125 LR measurements is smaller. The remaining difference can be attributed to the different measurement heights of the HR125 (112 m) and EM27/SUN (133 m). For a quantitative analysis the total column measurements are not utilised but rather the dry air mole fractions X_{Gas} , as in this representation systematic errors, e.g. ILS errors, timing errors, tracking errors and non-linearities tend to cancel out. Furthermore, the height dependence largely cancels out in this representation. The comparison

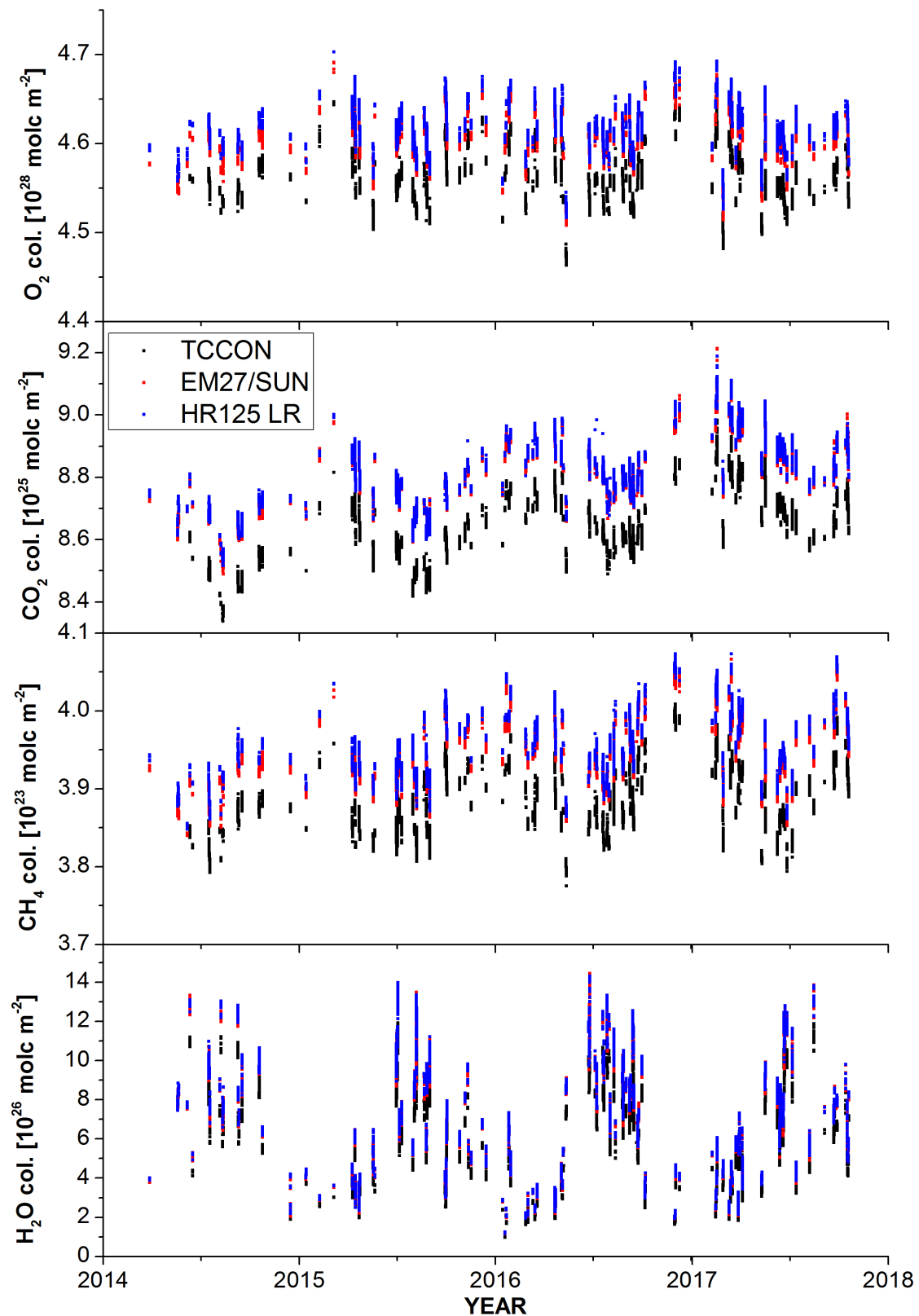


Figure 5.2: Total column time series for O_2 , CO_2 , CH_4 and H_2O measured at KIT in Karlsruhe from March 2014 until October 2017. The number of interferograms and recording time for the different data types are the following: TCCON: 2 IFGs, 114 s; EM27/SUN: 10 IFGs, 58 s; HR125 LR: 4 IFGs, 152 s. Only coincident measurement points (within one minute) are depicted.

ME	O ₂ [10 ²⁸ molc m ⁻²]	H ₂ O [10 ²⁶ molc m ⁻²]	CH ₄ [10 ²³ molc m ⁻²]	CO ₂ [10 ²⁵ molc m ⁻²]
August 16				
0.99	4.6097	7.4551	3.9457	8.7321
1.00	4.5936	7.4323	3.9356	8.6879
February 17				
0.99	4.6718	3.7746	4.0261	9.0968
1.00	4.6545	3.7628	4.0148	9.0455

Table 5.1: Sensitivity study on the effect of ILS changes on the retrieval of the total gas columns. Depicted are hourly pooled data on 01 August 2016 and 15 February 2017 around solar noon, corresponding to a solar elevation angle of 60° and 30°.

will be presented in the following sections.

Before that, a sensitivity study is performed demonstrating the effect of changes in the ILS on the gas retrieval. For this study, one hour of measurements around solar noon on 01 August 2016 and 15 February 2017, corresponding to solar elevation angles (SEA) of 60° and 30°, were analysed with artificially altered ILS values. The results are shown in Table 5.1. An increase of 1 % in modulation efficiency leads to a decrease of 0.35 % (0.37 %) on the retrieved O₂ column, 0.31 % (0.31 %) on H₂O, 0.26 % (0.28 %) on CH₄ and 0.50 % (0.57 %) on CO₂ for an SEA of 60° (30°). So the change in the retrieved total column is not alike, but a unique characteristic of each species, and also slightly airmass dependent. As the decrease in the CO₂ column is larger than the decrease in the O₂ column, XCO₂ decreases with an increasing ILS, 0.16 % (0.19 %) for 1 % ILS increase, whereas XCH₄ increases 0.10 % (0.09 %). This is opposed to prior studies (Gisi et al., 2012; Hedelius et al., 2016), reporting an increase of XCO₂ and decrease of XCH₄ for an increase of the modulation efficiency, albeit in agreement with the findings from Hase et al. (2013), reporting that a change in the modulation efficiency results in a larger decrease in the CO₂ column compared to the O₂ column.

5.1.3 X_{air}

In this section, the column averaged amount of dry air X_{air} is investigated. This quantity is a sensitive test of the stability of a spectrometer because for X_{air} there is no compensation of possible instrumental problems, in contrast to the DMFs, where errors can partially cancel out. X_{air} compares the measured oxygen column (VC_{O₂}) with surface pressure measurements (P_S):

$$X_{air} = \frac{0.2095}{VC_{O_2} \cdot \bar{\mu}} \cdot \left(\frac{P_S}{g} - VC_{H_2O} \cdot \mu_{H_2O} \right) \quad (5.1)$$

Here $\bar{\mu}$ and μ_{H_2O} denote the molecular masses of dry air and water vapour, respectively, g is the column averaged gravitational acceleration and VC_{H_2O} is the total column of water vapour. The correction with VC_{H_2O} is necessary as the surface pressure instruments measure the pressure of the total air column, including water vapour. For an ideal measurement and retrieval with accurate O₂ and H₂O spectroscopy, as well as accurate surface pressure, X_{air} would be unity. However, due to insufficiencies in the oxygen spectroscopy, this value is not obtained. For TCCON measurements X_{air} is typically ~ 0.98 (Wunch et al., 2015). For the EM27/SUN prior studies showed a factor of ~ 0.97 (Frey et al., 2015; Hase et al., 2015; Klappenbach et al., 2015). Large deviations ($\sim 1\%$) from these values indicate severe problems, e.g. errors with the surface

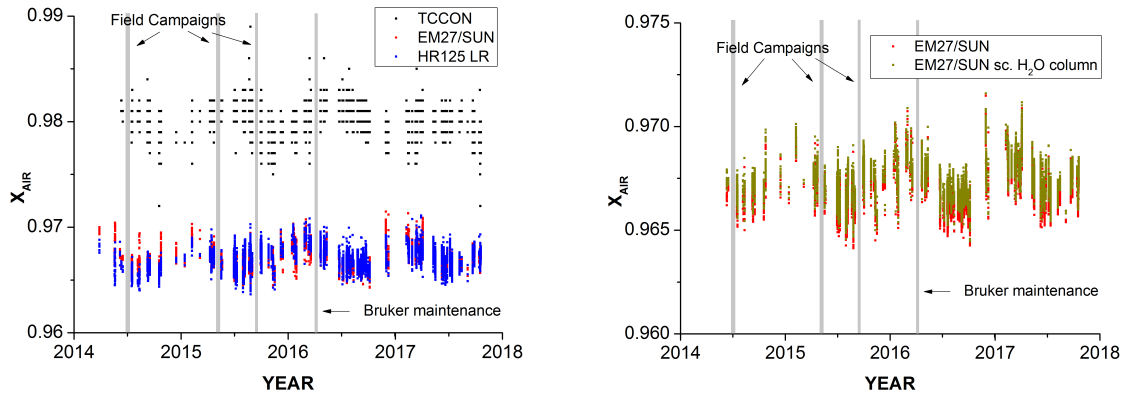


Figure 5.3: The left panel shows the X_{air} time series measured at KIT in Karlsruhe for the TCCON, EM27/SUN and HR125 LR data sets. For clarity, only coincident measurements (within one minute) of the data sets are plotted. Grey areas denote periods where the EM27/SUN was moved over long distances. The right panel shows a comparison of the original EM27/SUN time series with a modified version, where a scaling factor of 0.8 was applied to the H_2O total column.

pressure, pointing errors or changes in the optical alignment of the instrument. As mentioned in section 5.1.1, here X_{air} is used to check whether small changes in the modulation efficiency indicated by the open path measurements are due to actual alterations in the alignment of the EM27/SUN or due to the residual uncertainty of the calibration method.

The left panel of Figure 5.3 shows the X_{air} time series of TCCON, the EM27/SUN and HR125 LR. For clarity, only coincident data points that were measured within one minute between the different data sets are shown. Grey areas denote periods where the EM27/SUN was moved over long distances for campaigns or maintenance. The absolute values of X_{air} differ for the data sets, with 0.9805 ± 0.0012 for TCCON, 0.9669 ± 0.0010 for the EM27/SUN and 0.9670 ± 0.0011 for HR125 LR. The difference between the EM27/SUN and the HR125 LR is within 1σ precision. The difference between the EM27/SUN and the TCCON data set, which is commonly observed as previously noted, is a consequence of the different resolution together with the different retrieval algorithm (Gisi et al., 2012). It can be seen that all data sets exhibit a seasonal variability, which is more prominent in the TCCON data as can also be seen from the higher standard deviation. From this higher variability it can be concluded that the airmass dependency in the official TCCON O_2 retrieval is higher than for the PROFFIT retrieval, a finding also observed by Gisi et al. (2012). For the PROFFIT retrieval, it is suspected that part of the variability stems from insufficiencies in the utilised HITRAN 2008 H_2O linelist. It was reported by Tallis et al. (2011) that in the $8000 - 9200 \text{ cm}^{-1}$ region, line intensities are low by up to 20 % compared to other wavenumber regions. This in return will lead to a systematic overestimation of the water column, which also affects X_{air} . To test the sensitivity of X_{air} with respect to the measured H_2O column, in the right panel of Figure 5.3 the original EM27/SUN time series is compared to a data set where the H_2O column is artificially reduced by 20 %. This approach is further justified by a study from the Romanian National Institute for Research and Development in Optoelectronics (INOE) conducted in 2017, where they compared total column amounts of water vapour from an EM27/SUN and a radiometer. They found that the EM27/SUN values were systematically higher by 20 % (Dragos Ene, priv. comm.). And indeed, the standard deviation, which is here used as a measure for the seasonal variability, of the modified time series (0.0009) is lower when compared to the original time series (0.0010).

There are no obvious steps between the EM27/SUN and the HR125 LR data sets so that it can

be concluded that the EM27/SUN is stable over the complete course of the over three year long comparison and differences seen in the modulation efficiency are introduced by the remaining uncertainty in the calibration method.

5.1.4 XCO₂

In Figure 5.4 XCO₂ time series of the three data sets are shown together with offsets between the data sets. The general characteristics of the data sets are similar. The yearly increase of XCO₂ due to anthropogenic emissions of about 2 ppmv can be seen as well as the seasonal cycle with a decrease of XCO₂ of approximately 10 ppmv during summer due to photosynthesis, characteristic for mid latitude stations. Despite these agreements in the general trend, there are also differences between the data sets. With respect to the TCCON data the EM27/SUN and the HR125 LR data sets have a high bias (0.98 % and 0.84 %, respectively), see Table 5.2. A high bias was also observed by Gisi et al. (2012); Frey et al. (2015), albeit with smaller absolute differences. This is due to the fact that (1) in the Gisi et al. paper the TCCON data was retrieved with a prior version of GFIT (GGG2012) and (2) after the publication of the Frey et al. paper the Karlsruhe TCCON data was reprocessed with a customised GFIT retrieval accounting for baseline variations (Kiel et al., 2016b). The offset between EM27/SUN and TCCON shows a seasonal variability. Reasons for this are mainly the differences in airmass correction, averaging kernels and retrieval algorithm. These effects have been investigated before (Gisi et al., 2012; Klappenbach et al., 2015; Hedelius et al., 2016, 2017; Frey et al., 2015). For the long term stability of the EM27/SUN the focus lies on the comparison with the HR125 LR data set, where the above mentioned differences do not exist. There is a small offset between the two data sets, resulting in a calibration factor of 1.0014, which seems to be constant over time. To test this assumption a linear fit was applied to the XCO₂ ratios, see right panel of Figure 5.4. In Table 5.2 the slope coefficient is depicted. For both comparisons the slope per year is well within the 1σ precision (0.44 ppmv) of the data set. In absolute numbers the slope per year is ≈ -0.02 ppmv for both ratios, or a drift smaller than 0.1 ppmv over the whole comparison period of around three and a half years.

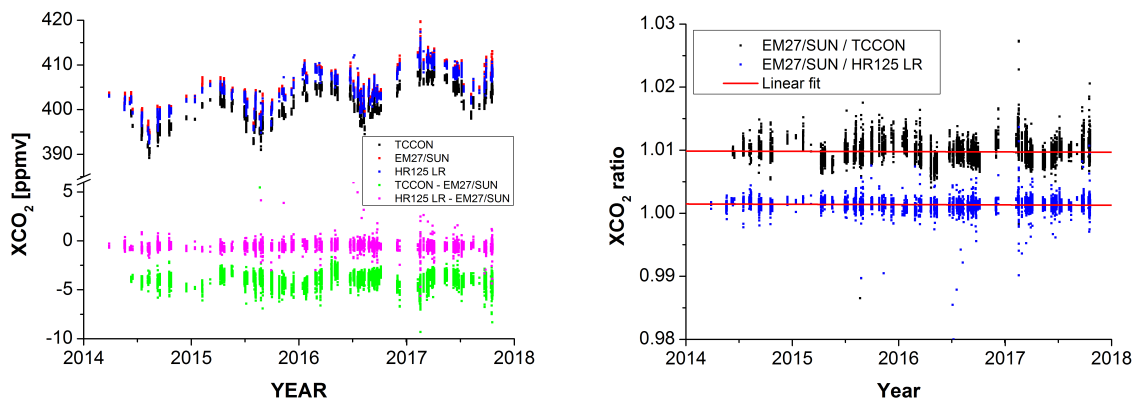


Figure 5.4: The left panel shows the XCO₂ time series measured at KIT in Karlsruhe for the three data sets from March 2014 to October 2017. Additionally, the absolute offsets between the EM27/SUN and the two other data sets are shown. For clarity, only coincident measurements (within one minute) of the data sets are plotted. The right panel shows the XCO₂ ratio between the EM27/SUN and the two HR125 data sets. A linear fit was applied to investigate a possible trend in the ratios.

XCO ₂ ratio	No. coincidences	Mean (1 σ)	Yearly trend in the ratio
EM27 / TCCON	8349	1.0098 (0.0015)	-5×10^{-5}
EM27 / HR125 LR	4624	1.0014 (0.0011)	-5×10^{-5}

Table 5.2: XCO₂ biases between EM27/SUN and HR125 data sets.

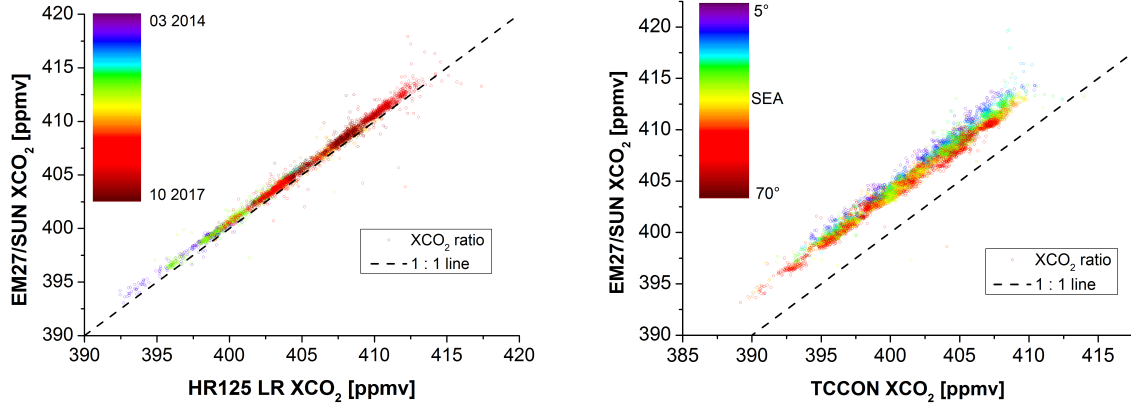


Figure 5.5: The left panel shows the XCO₂ comparison between EM27/SUN and HR125 LR. The colour bar denotes the date of the measurement, the dashed line is the 1 : 1 line. In the right panel the comparison with TCCON is shown. Note that here the colour bar shows the solar elevation angle (SEA).

Figure 5.5 shows the data sets in a very concise way. In the left panel the EM27/SUN is compared to the HR125 LR, the colour bar indicates the date of measurement and the dashed line is the 1 : 1 line. It can be seen that there is no trend in the data apart from the overall increase in time due to anthropogenic emissions. In the right panel the EM27/SUN is compared to the TCCON data set, the colour bar shows the solar elevation angle (SEA). This representation is chosen so that the remaining airmass dependency of the ratio can be seen. It is also interesting to note that omitting the TCCON airmass independent correction factor for our analysis would move the data set significantly closer to the 1 : 1 line. The scaling factor would change from 1.0098 to 0.9995. As this finding is not true for XCH₄ and is probably accidental, the AICF is maintained.

5.1.5 XCH₄

Figure 5.6 shows the XCH₄ time series of the different data sets. As for XCO₂, the general features are in agreement for all data sets. There is a slight annual increase of about 10 ppbv. Moreover, there is a seasonal cycle with a variability of ≈ 30 ppbv. However, compared to XCO₂ the interannual seasonality strength and phase varies significantly between the years due to the many different variable sinks and sources of methane, e.g. (Dlugokencky et al., 1997). The differences between the data sets largely resemble the differences observed for XCO₂. The bias between EM27/SUN and TCCON is 0.72 %, see Table 5.3. This bias is close to the bias observed by Hedelius et al. (2016), 0.75 %, where they used the GGG software package for the EM27/SUN retrieval. Although a single bias is reported, as was observed for XCO₂ the offset is not constant, but rather shows a seasonality. The retrievals between EM27/SUN and HR125 LR agree within 1 σ precision (0.9997 ± 0.0008). The left panel of Figure 5.7 shows the ratio between EM27/SUN and HR125 LR colour coded with the observation date. As for XCO₂, no trend is apparent. An explicit linear fit to the XCH₄ ratio produces a slope coefficient of 0.0001,

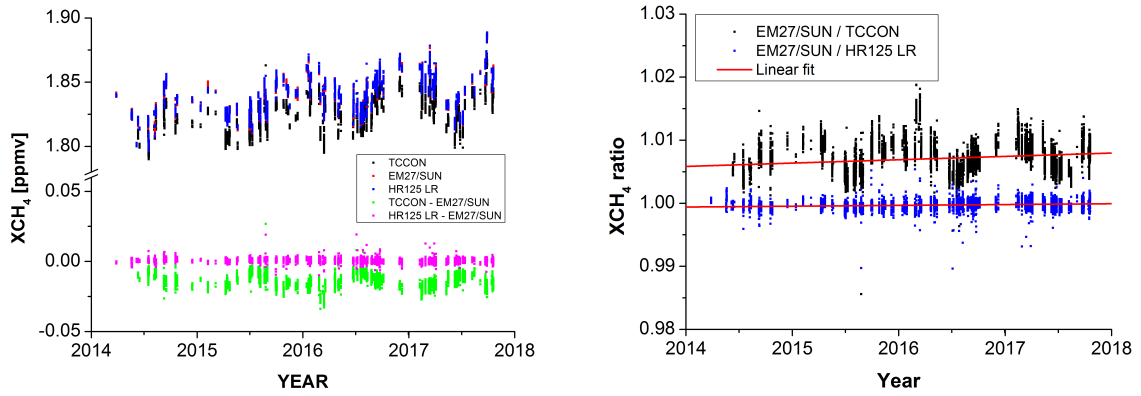


Figure 5.6: The left panel shows the XCH_4 time series for the three data sets measured at KIT in Karlsruhe from March 2014 to October 2017. Additionally, the absolute offsets between the EM27/SUN and the two other data sets are shown. For clarity, only coincident measurements (within one minute) of the data sets are plotted. The right panel shows the XCH_4 ratio between the EM27/SUN and the two HR125 data sets. A linear fit was applied to investigate a possible trend in the ratios.

XCH_4 ratio	No. coincidences	Mean (1σ)	Yearly trend in the ratio
EM27 / TCCON	8349	1.0072 (0.0024)	0.0005
EM27 / HR125 LR	4624	0.9997 (0.0008)	0.0001

Table 5.3: XCH_4 biases between EM27/SUN and HR125 data sets.

one order of magnitude smaller than the 1σ precision of the ratio (0.0008).

An interesting feature is observed in the ratio between EM27/SUN and TCCON data sets, see right panel of Figure 5.7. In general the pattern is similar to that of XCO_2 , with a slight dependence on the SEA. The ratio in the Figure is colour coded with the date of observation rather than the SEA. It can be seen that for 01 March 2016 and 14 March 2016 (shaded area in

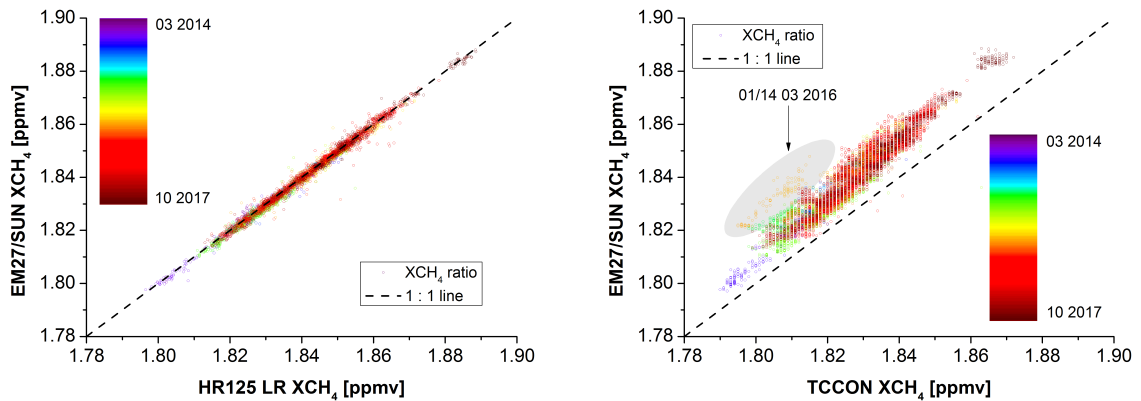


Figure 5.7: The left panel shows the XCH_4 comparison between EM27/SUN and HR125 LR. The colour bar denotes the date of the measurement, the dashed line is the 1 : 1 line. In the right panel the comparison with TCCON is shown. The shaded area encloses measurements from 01 and 14 March 2016. For these days the ratio is significantly different with respect to the remaining data set (see text for discussion).

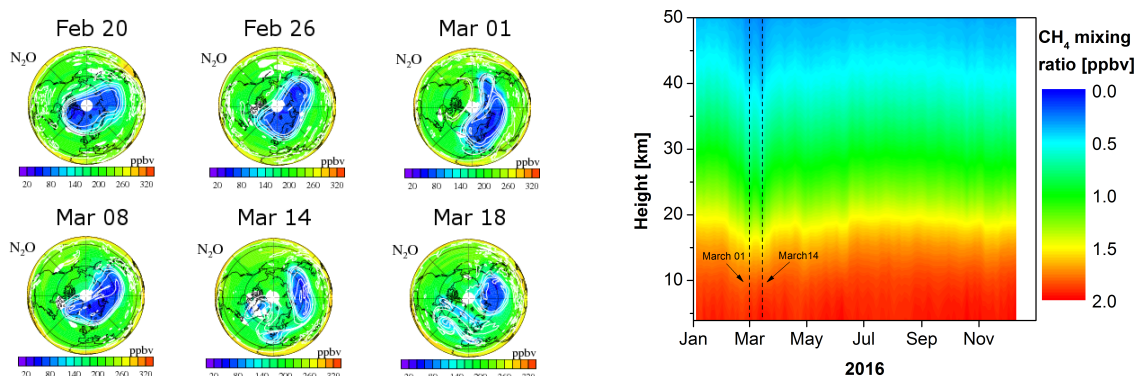


Figure 5.8: In the left panel N_2O MLS data from the Aura satellite are shown as a tracer for the position of the polar vortex for several days in February and March 2016. Data and plots courtesy of the NASA science team (<https://mls.jpl.nasa.gov/>). The right panel shows CH_4 mixing ratios from the NDACC FTIR station Jungfraujoch in Switzerland, downloaded from the NDACC archive (<http://www.ndaccdemo.org/stations/jungfraujoch-switzerland/>). Dotted lines depict 01 and 14 March 2016. For these dates, the XCH_4 data significantly differs from the remaining data set.

Figure 5.7) the XCH_4 ratio significantly differs from the other observations. Previous work by Ostler et al. (2014) has shown that stratospheric intrusions in the polar vortex have a different effect on MIR and NIR retrievals, even when using the same a priori profile. This is due to the differing sensitivity of the retrievals with respect to altitude. Therefore, differences between the true atmospheric profile and the assumed a priori profiles on these days could cause the differences seen. This will in turn lead to larger differences between EM27/SUN and TCCON XCH_4 because of the different impact on the retrieved columns due to differing sensitivities. A spread of the polar vortex to mid-latitudes could lead to significantly altered CH_4 profiles compared to the a priori profiles, explaining the observed differences in the XCH_4 ratio. The left panel of Fig. 5.8 shows N_2O data from the Microwave Limb Sounder (MLS) on the Aura satellite for several days in February and March 2016 on the 490 K potential temperature level, corresponding to a height of approximately 18 km. N_2O is chosen because it serves as a tracer for the position of the polar vortex. Indeed, it seems that beginning of March 2016 the polar vortex stretches out to mid-latitudes. To further test this hypothesis in the right panel of Figure 5.8 NDACC CH_4 profiles from the Jungfraujoch station in 2016 are shown. The station is situated approximately 270 km south of Karlsruhe with a station height of 3580 m. For dates without measurements, the data were interpolated using a weighted average. The dotted black lines denote 01 March 2016 and 14 March 2016, the dates on which the XCH_4 ratio between EM27/SUN and TCCON shows an anomaly. The changed profile form during that period is clearly visible. As this station is south of Karlsruhe, it is expected that also for Karlsruhe the CH_4 profile shows considerable downwelling, explaining the observed anomaly in the XCH_4 ratio.

5.2 Ensemble performance

Having demonstrated the long term stability of the EM27/SUN with respect to a reference spectrometer in the previous section, here the level of agreement of an ensemble of EM27/SUN spectrometers is investigated. The procedure is the same as for the comparison between the reference EM27/SUN and the HR125. First, the ILS is analysed, followed by calibration factors for XCO_2 and XCH_4 .

5.2.1 ILS measurements and instrumental examination

Instrument SN	ME at MOPD	Phase error [rad]
29	0.9862	0.0014
32	0.9862	0.0034
33	0.9814	-0.0017
37	0.9862	0.0019
38	0.9784	0.0009
39	0.9811	-0.0005
41	0.9835	0.0001
42	0.9752	0.0039
44 (prior)	0.9374	-0.0074
44	0.9714	-0.0019
45	0.9845	0.0034
46	0.9837	0.0024
50	0.9839	0.0023
51	0.9847	0.0017
52	0.9854	0.0048
53	0.9830	0.0025
59	0.9886	0.0029
61	0.9830	0.0013
62	0.9823	0.0053
63	0.9853	0.0011
65	0.9881	0.0024
69	0.9863	0.0030
70	0.9775	0.0056
72	0.9959	0.0030
75	0.9972	0.0041
76	1.0160	0.0007
77	0.9855	0.0016
85	0.9876	0.0025
86	0.9830	0.0031
88	0.9832	0.0007
91	0.9836	0.0021

Table 5.4: Summary of the modulation efficiencies at MOPD and phase errors for all EM27/SUN calibrated in Karlsruhe.

The measurement of the ILS is a valuable diagnostic for detecting misalignments of spectrometers because differences in the ILS of the EM27/SUN spectrometers due to misalignment can lead to biases between the instruments. Here, the spread of ILS values of all EM27/SUN spectrometers that were calibrated at KIT in the past four years is estimated. Numerical values are given in Table 5.9, the results are visualised in Figure 5.9. The black square denotes an ILS measurement of the HR125 spectrometer, also with 1.8 cm MOPD. This test was done to check for an absolute offset of our method. The HR125 would be expected to show an ideal ILS for short optical path differences. However, a value of 0.9824 was obtained. From this measurement it is concluded that our method shows an absolute offset and that values between 0.98 and 0.99 are desired.

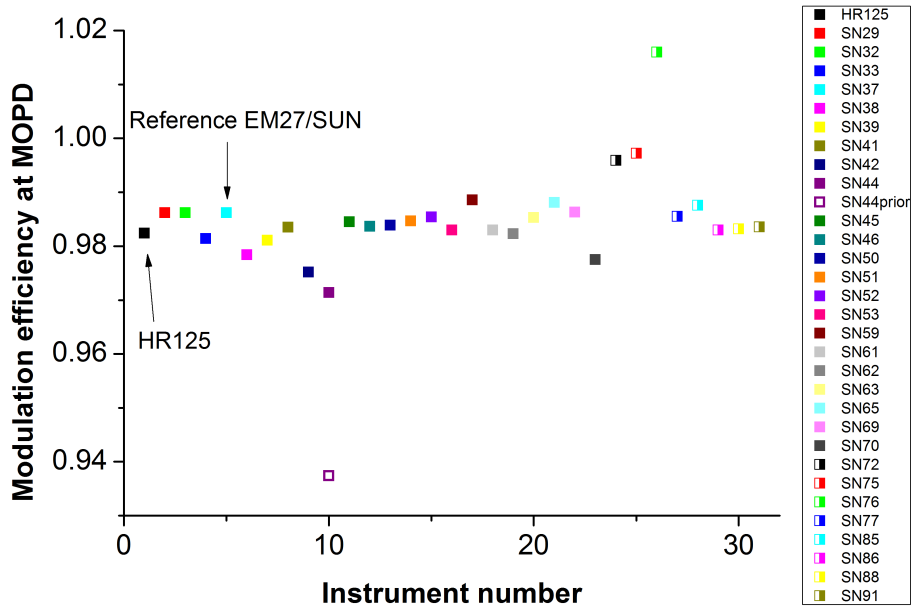


Figure 5.9: Modulation efficiencies at MOPD for all EM27/SUN calibrated in Karlsruhe. For SN44 prior, ILS measurements were taken before an alignment check and subsequent realignment of the instrument. For comparison reasons, also an ILS measurement for the HR125 was performed.

In general, the agreement between the 30 tested EM27/SUN is good with an ensemble mean of 0.9851 ± 0.0078 , which is not differing significantly from the value obtained for the HR125, but there are exceptions. Instrument SN 44 was checked at KIT only after an upgrade with the second channel was performed at Bruker Optics. Before realignment, the instrument showed a very low ME value of 0.9374. A realignment of the instrument enhanced the ME to 0.9714. This is still significantly low compared to the EM27/SUN ensemble mean, but the difference was drastically reduced. The second instrument showing strong deviations from the ensemble mean is SN 76 with an ILS of 1.0160, the only instrument showing overmodulation. The ILS was even higher (1.0350) when first ILS measurements were performed. Due to our findings, the manufacturer exchanged the interferometer block which reduced the overmodulation, but it partly remained. For instrument SN 75 and SN 76 it has recently been confirmed that the manufacturer forgot to insert the foreseen spacer to achieve the correct detector position with respect to the beamsplitter. The beamsplitter is coated, and the coating is applied on both sides of the beamsplitter over half the surface area. If the light beam exiting the interferometer and the detector element are in the line of the two coating regions, detrimental effects occur. For this reason, the detector element needs to be lifted up with respect to the interferometer. This problem also occurred for instrument SN 77 but there it was diagnosed and corrected by KIT (ILS before lifting: 1.0340, ILS after correction: 0.9855).

The above mentioned problems show the benefit of the calibration routine at KIT. Imperfections from non-ideal alignments were diagnosed and corrected. Moreover, other detrimental effects, e.g. double-passing, channelling, non-linearity issues, solar tracker problems, non-ideal alignment of the second detector or camera issues, were corrected or minimised for a number of instruments. Finally, it was checked whether the linear interpolation method suppressing sampling ghosts was activated.

Instr. SN	Dates	No. co.	XCO ₂ factor	XCH ₄ factor	O ₂ factor
29	140606, 140718	490	1.0004 (0.02)	0.9997 (0.03)	1.0008 (0.03)
32	150414 - 150422	1548	0.9997 (0.03)	0.9997 (0.03)	1.0004 (0.03)
33	170807, 170815	339	0.9991 (0.03)	0.9994 (0.04)	1.0009 (0.05)
38	150410 - 150421, 160121	1609	0.9989 (0.03)	0.9997 (0.04)	0.9988 (0.04)
39	140717, 150414, 150415	1210	0.9992 (0.04)	0.9994 (0.04)	1.0003 (0.04)
41	140717, 150414 - 150422	1877	0.9999 (0.03)	1.0002 (0.03)	0.9991 (0.03)
42	160730, 160801	368	0.9978 (0.04)	1.0003 (0.04)	0.9975 (0.03)
44	170227	286	0.9979 (0.03)	0.9984 (0.03)	0.9985 (0.03)
45	170807, 170815	382	0.9995 (0.03)	0.9991 (0.04)	1.0008 (0.02)
46	170808, 170815	503	0.9993 (0.03)	0.9994 (0.03)	1.0003 (0.03)
50	150421, 150422	699	0.9999 (0.03)	0.9995 (0.03)	0.9995 (0.03)
51	160126, 160129	256	0.9995 (0.03)	0.9993 (0.03)	1.0007 (0.05)
52	150421, 150422	727	0.9990 (0.04)	0.9998 (0.05)	1.0002 (0.05)
53	150421, 150422	729	0.9987 (0.03)	1.0001 (0.03)	0.9992 (0.04)
59	160318	273	0.9998 (0.03)	0.9991 (0.03)	1.0019 (0.04)
61	151002, 170713	618	0.9993 (0.03)	0.9996 (0.04)	1.0000 (0.04)
62	160121	18	0.9988 (0.04)	0.9990 (0.02)	1.0002 (0.02)
63	160121	15	1.0003 (0.05)	1.0001 (0.05)	1.0002 (0.07)
65	160511	234	1.0005 (0.04)	0.9998 (0.05)	1.0020 (0.03)
69	160908, 170713	636	0.9994 (0.03)	0.9993 (0.03)	1.0008 (0.03)
70	160831, 160906	522	0.9985 (0.02)	1.0005 (0.03)	0.9978 (0.03)
72	170215, 170216	433	0.9994 (0.05)	1.0001 (0.03)	0.9999 (0.04)
75	170516, 170517	852	0.9993 (0.03)	0.9991 (0.03)	1.0018 (0.05)
76	170608	365	0.9991 (0.04)	0.9997 (0.04)	1.0026 (0.06)
77	170927	389	0.9999 (0.03)	0.9997 (0.03)	1.0001 (0.04)

Table 5.5: Calibration factors for XCO₂, XCH₄ and O₂ for all investigated instruments with respect to the reference EM27/SUN spectrometer as well as calibration dates and number of coincident measurements. Values in brackets denote percent standard deviations.

5.2.2 XCO₂ and XCH₄ comparison measurements

After checking alignment and performing lamp measurements, side-by-side solar calibration measurements were performed on the terrace on top of the KIT-IMK office building with each spectrometer with respect to the reference EM27/SUN and also a co-located HR125 spectrometer. Calibration measurements started in June 2014 and are ongoing, if new spectrometers arrive for testing. The aim is to have at least one day of comparison measurements so that the spectrometers can be scaled to TCCON via the reference EM27/SUN. TCCON is extensively compared to measurements on the WMO scale. Dates of the comparison measurements for the different spectrometers as well as number of coincident measurements are shown in Table 5.5. On 21 January 2016 the reference spectrometer suffered from laser sampling errors after approximately one hour of measurements. Therefore, the number of coincident measurements for SN 62 and SN 63 that were calibrated on this date are sparse.

The calibration factors and standard deviations for all instruments with respect to the reference spectrometer are also depicted in Table 5.5. Calibration factors were obtained using the methods described in section 5.1.4. The calibration factors are close to nominal for all species and

instruments. Instruments that were calibrated more than once in Karlsruhe (SN38, SN39, SN 41, SN 61 and SN 69) do not exhibit a larger standard deviation compared to the other instruments. This supports the assumption of long term stability as observed by the reference instrument, see section 5.1.

For XCO₂ the ensemble mean is high compared to the reference EM27/SUN, with a mean calibration factor of 0.9993. Applying this factor to all calculated calibration factors centres the data around the ensemble mean. As an estimate for the spread of the calibration factors $\frac{1}{n}\sum|XGas\ factor - 1|$, an average bias between the instruments of 0.20 ppmv is calculated. From Table 5.5 also an average standard deviation $\frac{1}{n}\sum|\sigma|$ of 0.13 ppmv is estimated. For XCH₄ the ensemble mean is closer to the reference EM27/SUN (0.9997) when compared to XCO₂. From this an average bias of 0.8 ppbv results. The average standard deviation is 0.6 ppbv. These values are comparable to results obtained in a study from Hedelius et al. (2017). They checked the intercomparability of the 4 United States TCCON sites using an EM27/SUN as a travel standard. They report average biases of 0.11 ppmv for XCO₂ and 1.2 ppbv for XCH₄, for the average standard deviations they obtain 0.34 ppmv (XCO₂) and 1.8 ppbv (XCH₄). It has to be noted that for the Hedelius et al. (2017) study only data within ± 2 h local noon were taken into account whereas here no constraints regarding the time of measurement were applied. As another sensitive test the O₂ total column calibration factors are given. In contrast to XCO₂ and XCH₄, there is no canceling of errors in this quantity. The ensemble mean is slightly high compared to the reference EM27/SUN (0.9999). The average bias is 0.11 % O₂ with an average standard deviation of 0.04 % O₂.

Note that for the given setup this average bias is a worst case scenario. The bias only applies if no calibration factor is used in the subsequent analysis. The main strength of this calibration routine is that the computed calibration factors can be used, thereby significantly lowering the bias between the EM27/SUN. The remaining bias is then given by the long term drift of the individual instrument, see section 5.1.4 and 5.1.5, and potential sudden alignment drifts due to mechanical strain from e.g. transportation or campaign use. To estimate this drift, the calibration factors before and after the Berlin campaign performed in 2014 are utilised. There the drifts between five instruments were below 0.01 % for both XCO₂ and XCH₄ (Frey et al., 2015).

Ideally, identical calibration factors are expected as the real ILS of the instruments is taken into account. As this is not the case, it is investigated whether the remaining differences can be attributed to the uncertainties of the open path measurements, which are summarised in Table 4.2. The results are incorporated in Fig. 5.10. The left panel shows the correlation between O₂ and XCO₂ calibration factors. Black squares denote the empirical calibration factors derived from the side-by-side measurements. The red squares show calculated calibration factors based on the ME uncertainty budget. The dashed red line is a linear fit through the calculated factors. About half the measured empirical factors are within the bounds of the factors derived from the ME error budget. Furthermore, the slope of the calculated and empirical factors are in good agreement, confirming that the remaining ME uncertainty is contributing to the uncertainty of the calibration factors (roughly 50 % of the observed scatter). The other contributions for this uncertainty are likely due to a superposition of various small device-specific imperfections. The right panel of Fig. 5.10 shows the correlation between O₂ and XCH₄ calibration factors. The findings mentioned above for the O₂ and XCO₂ correlation also hold true here.

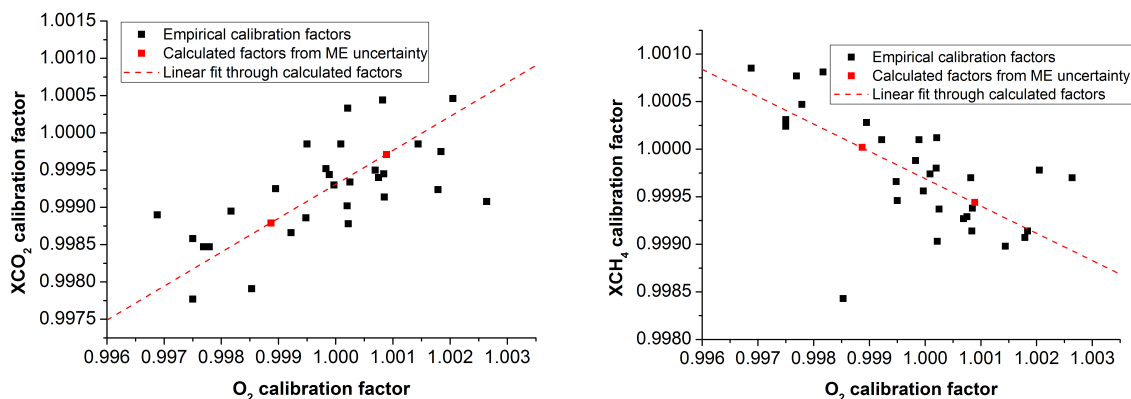


Figure 5.10: Correlation of O_2 calibration factors and XCO_2 (left panel) as well as XCH_4 (right panel) calibration factors. Black squares show the empirical calibration factors from the side-by-side measurements, red squares show calculated factors derived from the total ME uncertainty shown in Table 4.2, the dashed red line is a linear fit through the calculated factors. The slope of empirical and calculated factors is in good agreement.

5.2.3 Conclusions

Based on a long-term intercomparison of column-averaged greenhouse gas abundances measured with an EM27/SUN FTIR spectrometer and with a co-located 125HR spectrometer, respectively, it is concluded that the EM27/SUN offers highly stable instrument characteristics on timescales of several years. The drifts on shorter timescales reported by Hedelius et al. (2016) were probably exclusively - as conjectured by the authors of the study - due to a deviation from the instrumental design as originally recommended. The application of a wideband detector suffering from non-linearity together with steadily decreasing signal levels due to ageing of the tracker mirrors seem to be the reason for the observed drifts.

The favourable instrument stability which is preserved even during transport events and operation under ambient conditions suggests that the EM27/SUN spectrometer is well suited for campaign use and long-term deployment at very remote locations as a supplement of the TCCON. An annual to biannual check of the instrument performance by performing a side-by-side intercomparison with a TCCON spectrometer seems adequate for quality monitoring. For separating out instrumental drifts from atmospheric signals, the addition of low-resolution spectra derived from the TCCON measurements is highly useful, because in this kind of comparison, the smoothing error and any possible resolution-dependent biases of the analysis software cancel out. The ensemble performance of 30 EM27/SUN spectrometers turns out to be very uniform, supported by a centralised acceptance inspection performed at KIT before the spectrometers are deployed. When using the empirical ILS parameters derived for each spectrometer, the scatter in XCO_2 amounts 0.13 ppmv, while it is 0.6 ppbv for XCH_4 . The standard deviation of the oxygen columns is 0.04%. It is expected that the conformity of measurement results will be even better than indicated by this scatter, if the reported empirical calibration factors are taken into account. These empirical calibration factors are likely composed of several small device-specific error contributions, a major contribution is identified to stem from the uncertainty of the ILS measurements.

Chapter 6

Berlin campaign

In this chapter, the results from a measurement campaign performed in Berlin 2014 using five EM27/SUN are utilised to determine the CO₂ emission strength of the major city Berlin. First, the level of stability of the five instruments before and after the campaign is investigated. After this, the general design considerations for this campaign are explained. Thereafter, the EM27/SUN measurements from Berlin are shown, followed by a description of a simple dispersion model representing the emissions of Berlin, which will afterwards be compared to the EM27/SUN measurements to deduce the CO₂ emission strength of Berlin. The findings of this chapter have been published in Frey et al. (2015) and Hase et al. (2015), from which this chapter is mainly adopted.

6.1 Calibration measurements

In chapter 5 the long term stability of one EM27/SUN is investigated, as well as the ensemble performance with respect to this reference EM27/SUN. Remaining is the question of the stability of multiple spectrometers before and after campaign use. High requirements with regard to the stability of the EM27/SUN are demanded, as the emission of a major city only introduces an increase of column-averaged DMFs XCO₂ and XCH₄ in the sub percentage level. Therefore, great care has to be taken that differences can be attributed to real signals and not to instrumental drifts. High instrumental precision and stability are a prerequisite for this approach. The reference EM27/SUN used in chapter 5 for the long term comparison will be denoted instrument 1 in the following.

6.1.1 Instrumental line shape

The calibration measurements consisted of open path measurements and solar measurements. Results of the open path measurements are depicted in Table 6.1. For the trace gas retrieval the mean value of the measurements before and after the campaign is used, the setup for these experiments was exactly the same. The modulation efficiencies show very good agreement before and after the campaign. The correlation between ME amplitude and XCO₂ was deduced from a sensitivity test, see section 5.1.2. Instrument 2 has the biggest difference in terms of ILS modulation efficiency change before and after the campaign with 0.19 %, corresponding to a change of only 0.03 % for XCO₂ and 0.02 % for XCH₄. Note that this is not self-evident since the instruments were transported from Karlsruhe to Berlin by car and moved each measurement day during the campaign, thus experiencing a lot of mechanical impacts and vibrations.

Instr.	ME (3 Jun)	ME (15 Jul)
1	0.9834	0.9848
2	0.9774	0.9793
3	0.9827	0.9842
4	0.9860	0.9863
5	0.9808	0.9814

Table 6.1: Compilation of ILS modulation efficiencies measured at maximum OPD = 1.8 cm. Measurements were performed in Karlsruhe in June and July 2014, in between the spectrometers were transported for campaign measurements on the road, thus experiencing a lot of mechanical impacts and vibrations.

6.1.2 Side-by-side solar calibration measurements

Side-by-side measurements were performed at KIT in Karlsruhe before the Berlin campaign on 06, 13 and 16 June 2014 as well as after the campaign on 16, 17 and 18 July 2018. For the spectral analysis of the solar spectra the PROFFIT 9.6 retrieval algorithm is used, utilising the ILS parameters from the open path measurements, see section 6.1.1. Deviating from the strategy of the long term comparison measurements described in section 4.2.3, instead of using one temperature profile per day, here MERRA model data are applied, providing temperature data on a $1.25^\circ \times 1.25^\circ$ on pressure levels ranging from 1000 - 0.1 hPa 8 times a day. Furthermore, for the a priori trace-gas profiles, the WACCM ver. 6 climatology was utilised¹.

Total column amounts

In Figure 6.1 the column values of the measured species of the different instruments are depicted. It is apparent that the intraday variability of all spectrometers is nearly identical. Data gaps appearing for all instruments were caused by passing clouds. In addition, instrument 4 suffered from a hardware problem on 13 June 2014 as well as on two days after the Berlin campaign and therefore was only partly able to perform measurements. The tracker of this instrument did not follow the sun anymore but moved to a random position during initialisation. This was caused by a mechanical problem of the azimuthal tracker motor. Intraday changes of the O₂ column can be mostly attributed to pressure changes, which will be discussed in section 6.1.3. There are slight systematic offsets, strongest between instrument 2 and instrument 4 with a difference of 0.2 %. However, note that a similar offset is also observed in the CO₂ and CH₄ gas columns, as can be seen in Fig. 6.1. Therefore, the resulting effects on the target quantities XCO₂ and XCH₄ are smaller.

For a better comparison an intercalibration factor between the instruments is established. This is done in the same way as was discussed in chapter 5. All spectrometers are scaled to instrument 1, as it is also the reference EM27/SUN used in the long term comparison.

In Table 6.2 the calibration factors for the O₂ column for the calibration measurements before and after the campaign are given. Differences before and after the campaign are very small, only 0.03 % for instrument 2 and even less for the other instruments. This is surprisingly good, because column values are sensitive to various potential error sources, including ILS errors, timing errors, tracking errors and non-linearities.

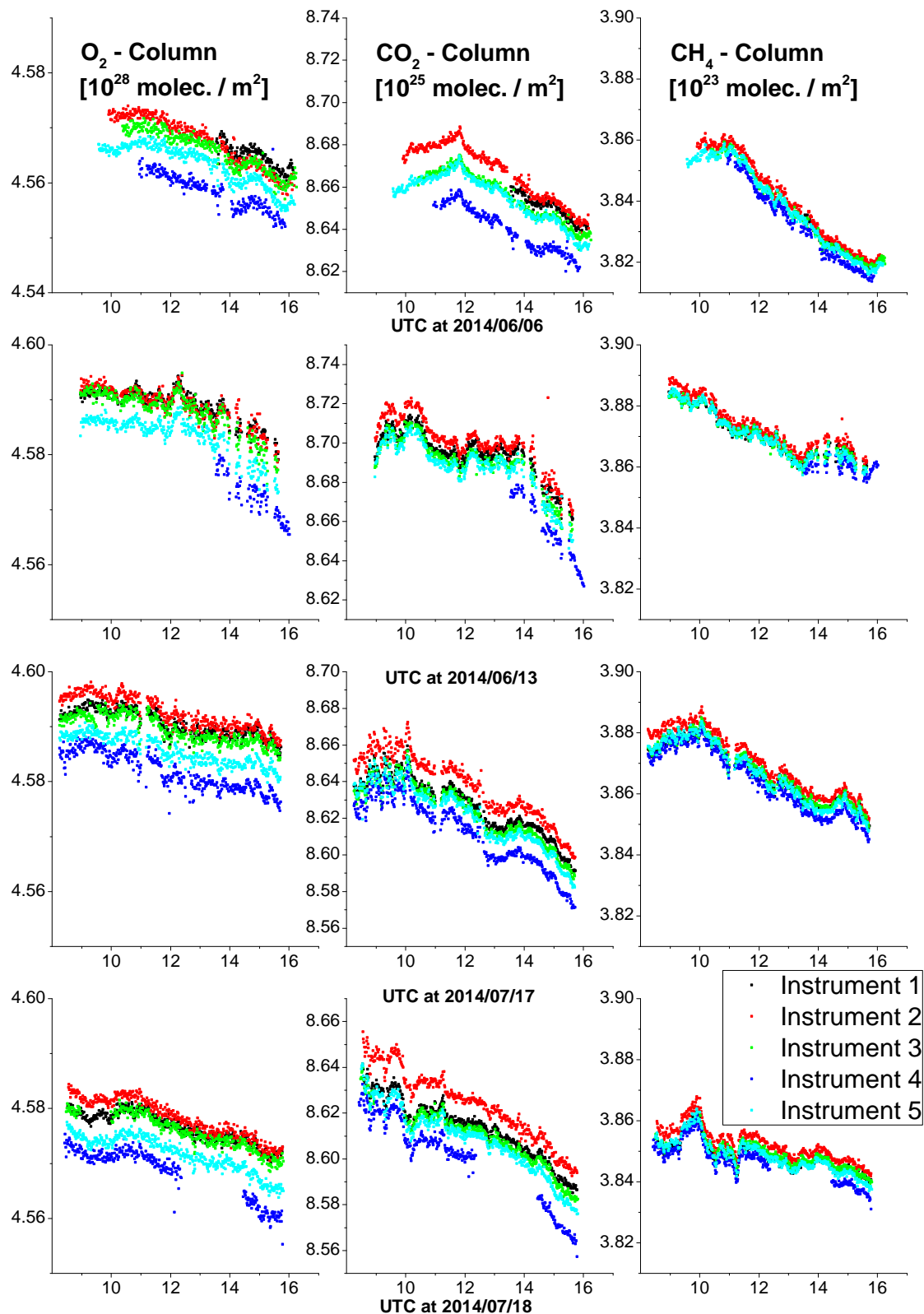


Figure 6.1: Total columns of O_2 , CO_2 and CH_4 for the different spectrometers on four days of the calibration measurements in Karlsruhe. Solar observations were performed in June and July 2014, in between the spectrometers were transported for campaign measurements. One data point consists of 10 interferograms, the measurement time being 58 s. The ILS parameters from the open path measurements are used.

Instr.	O ₂ col. June	O ₂ col. July
2	1.0000 (0.04)	0.9997 (0.04)
3	1.0003 (0.03)	1.0002 (0.03)
4	1.0018 (0.07)	1.0020 (0.04)
5	1.0012 (0.03)	1.0011 (0.03)

Table 6.2: Calibration factor for O₂ for the different instruments with respect to instrument 1. Measurements were performed in Karlsruhe during June and July 2014, in between the spectrometers were transported for campaign measurements. All spectrometers are scaled to instrument 1 because it is also the reference EM27/SUN used in the long term comparison in chapter 5. Values in parentheses denote the percent 1 σ precision of the ratio.

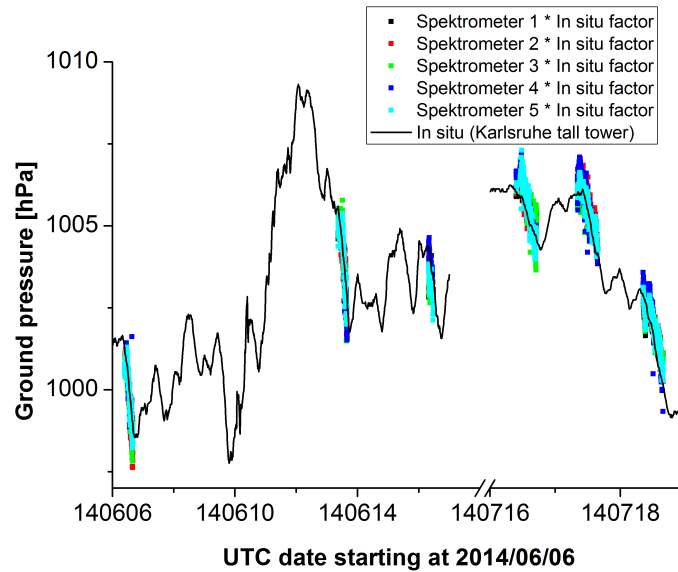


Figure 6.2: In situ pressure data from the Karlsruhe tall tower (www.imk.kit.edu/messmast/) together with pressure data calculated from total column amounts of O₂ and CO₂. The column data is scaled with an in situ factor of 0.9700 for better comparability.

6.1.3 O₂ column as an indicator of instrumental stability

The consistency between retrieved O₂ and measured surface pressure is a very sensitive test for the instrumental stability because for the oxygen column, there is no compensation of possible instrumental problems which were discussed in the previous section. In order to compare the data set with barometer measurements recorded at the ground level of the Karlsruhe meteorological tall tower, the ground pressure is calculated from the measured O₂ and H₂O total columns:

$$P_S = \left(\frac{O_2}{0.2095} \cdot \bar{\mu} + H_2O \times \mu_{H_2O} \right) \cdot g \cdot \exp \left(-\frac{\Delta h}{h_S} \right) \quad (6.1)$$

P_S is the surface pressure, $\bar{\mu}$ the molecular mass of dry air, μ_{H_2O} the molecular mass of water, g the gravity acceleration, Δh the height difference between the Karlsruhe tall tower ground level and the Institute terrace where the EM27/SUN spectrometers were located and h_S the scaling height. A systematic scaling factor of 0.9700 is found between these records and the barometric ground pressure. This factor is in good agreement with the observations during the

¹<http://www.2cesm.ucar.edu/working-groups/wawg>

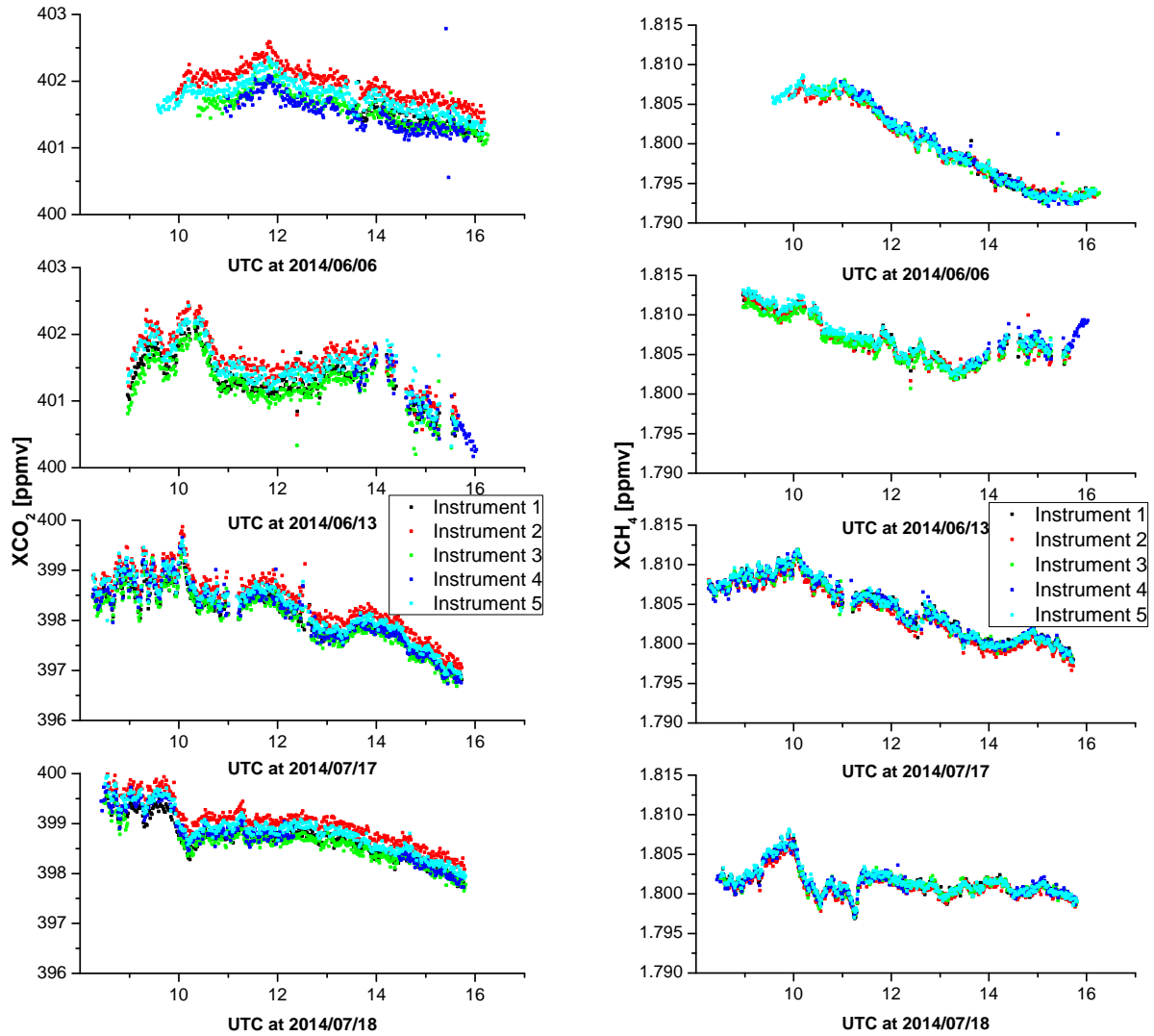


Figure 6.3: In the left panel uncalibrated XCO_2 values for all instruments used in the Berlin campaign are depicted. The right panel shows calibrated XCH_4 values. Experiments and measurement days are the same as in Figure 6.1.

Berlin campaign or during the Polarstern campaign (Klappenbach et al., 2015). Its origin can mainly be attributed to oxygen line intensity errors (Washenfelder et al., 2006). The scatter between the different instruments is smaller than 0.02 %. In Figure 6.2 the pressure values obtained from the total columns are scaled to the barometric data for better comparability. The record of the dry ground pressure is compatible with the retrieved water vapour and molecular oxygen column.

6.1.4 Column-averaged dry air mole fraction

The left panel of Figure 6.3 shows the column-averaged DMF of CO_2 . In this representation, systematic errors tend to cancel out, which leads to a high degree of reproducibility in the time series difference between the instruments. Until this point, no post calibration has been performed between the instruments, only the individual ILS of each instrument has been taken into account. Table 6.3 shows the intercalibration factor for XCO_2 and XCH_4 before and after the campaign. The method to derive the factors is the same that was used for the O_2 column

Instr.	XCO ₂ June	XCO ₂ July	XCH ₄ June	XCH ₄ July
2	0.9993 (0.03)	0.9992 (0.03)	0.9993 (0.03)	0.9994 (0.03)
3	1.0002 (0.03)	1.0002 (0.03)	0.9998 (0.04)	0.9997 (0.04)
4	0.9999 (0.03)	0.9998 (0.03)	0.9989 (0.05)	0.9988 (0.03)
5	0.9995 (0.03)	0.9996 (0.03)	0.9990 (0.03)	0.9990 (0.03)

Table 6.3: Calibration factor for XCO₂ and XCH₄ for the different instruments with respect to instrument 1. Measurements were performed in Karlsruhe during June and July 2014, in between the spectrometers were transported for campaign measurements. All spectrometers are scaled to instrument 1 because it is also the reference EM27/SUN used in the long term comparison in chapter 5. Values in parentheses denote the percent 1σ precision of the ratio.

calibration. For XCO₂ an agreement before and after the campaign within the measured noise level is obtained. For each individual instrument, the difference before and after the campaign is below 0.01 % or 0.04 ppmv. This means an intercalibration factor can be applied for each instrument which is valid before and after the Berlin measurements. This is an important prerequisite for campaign observations. For XCH₄ the same level of agreement is found (0.01 % or 0.2 ppbv). In the right panel of Fig. 6.3 the calibrated XCH₄ time series for the calibration measurements is depicted. Note that one global intercalibration factor is applied for all measurement days. The scatter is very low for both species. Variations during the day stem from real signals, for example the XCO₂ peaks on 16 July 2014 were also measured by a co-located TCCON instrument (see Figure 6.4). The diurnal variation of the EM27/SUN measurements matches the TCCON daily cycle remarkably well for XCO₂ and XCH₄. For this comparison, the global calibration factor derived from the 3.5 years long time comparison presented in chapter 5 was applied. Note that due to the much lower spectral resolution of the EM27/SUN a very high spectral signal to noise ratio is achieved, so the noise level of the resulting XCO₂ data is even smaller as compared to the data generated by the TCCON spectrometer.

Because of the high level of stability of the spectrometers demonstrated in this work, this calibration routine allows the unambiguous detection of X_{gas} enhancements in the sub-ppmv range for XCO₂ and ppbv range for XCH₄. Therefore, this approach will be used in the following sections for the detection and quantification of the Berlin city CO₂ emission source.

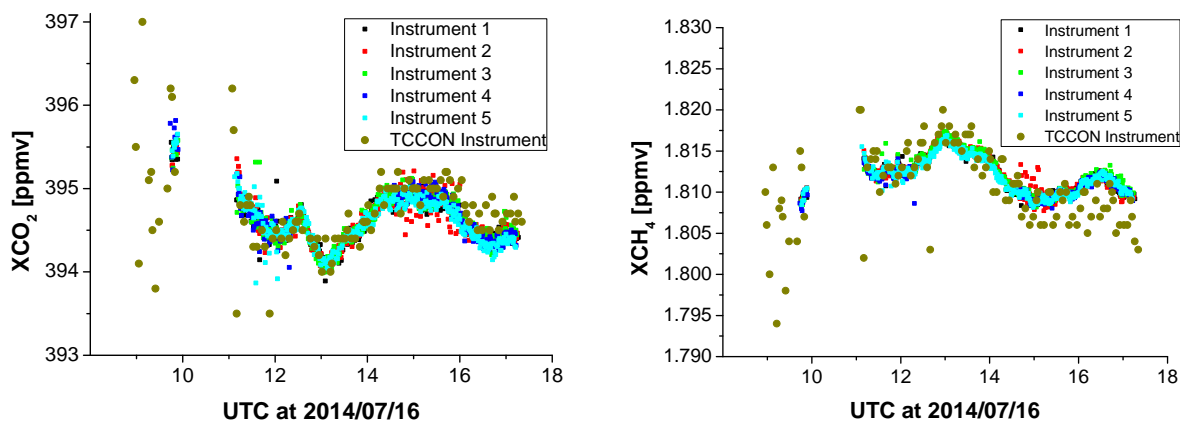


Figure 6.4: Calibrated XCO₂ and XCH₄ values for the EM27/SUN spectrometers participating in the Berlin campaign on 16 July 2014. Golden dots show data from a co-located TCCON instrument.

6.2 Campaign considerations and overview

The demonstration campaign took place in the periphery of Berlin from 23 June to 11 July 2014, five EM27/SUN spectrometers were deployed. Berlin was chosen as the target city because (1) Berlin is a major city, a prerequisite for measuring detectable enhancements (2) Berlin is not in the vicinity of other sources, simplifying the attribution of CO₂ emissions to the city (3) the flat topography facilitates the interpretation of the measurements. Figure 6.5 shows a map with the five stations, together with pictures from the sites, mostly during operations. Four spectrometers were placed along a circle with 12 km radius around the city centre. The Charlottenburg instrument (number 2) is situated closer to the city centre, inside the Berlin motorway ring. Coordinates and altitude of the different stations are given in Table 6.4. Coordinates were derived using a GPS receiver, for the determination of the altitudes time-averaged GPS measurements performed repeatedly at Mahlsdorf were combined with the average differences between the time series of ground pressures recorded at each site. The values show excellent agreement with topographic data from the website <https://www.sonnenverlauf.de/>.

Location	ID	Latitude (° N)	Longitude (° E)	Altitude (m)
Mahlsdorf	MAH	52.486	13.589	39.0
Charlottenburg	CHA	52.505	13.302	47.7
Heiligensee	HEI	52.622	13.228	34.5
Lindenberg	LIN	52.601	13.519	63.3
Lichtenrade	LIC	52.391	13.392	44.8

Table 6.4: Locations and altitudes of the measurement sites during the Berlin field campaign. Coordinates were derived from GPS sensors. The altitudes were derived from continuous GPS measurements performed in Mahlsdorf in conjunction with average differences between sites according to ground pressure data from the MHB data loggers. The altitudes were checked against topographic data (<https://www.sonnenverlauf.de/>) and excellent agreement was found.

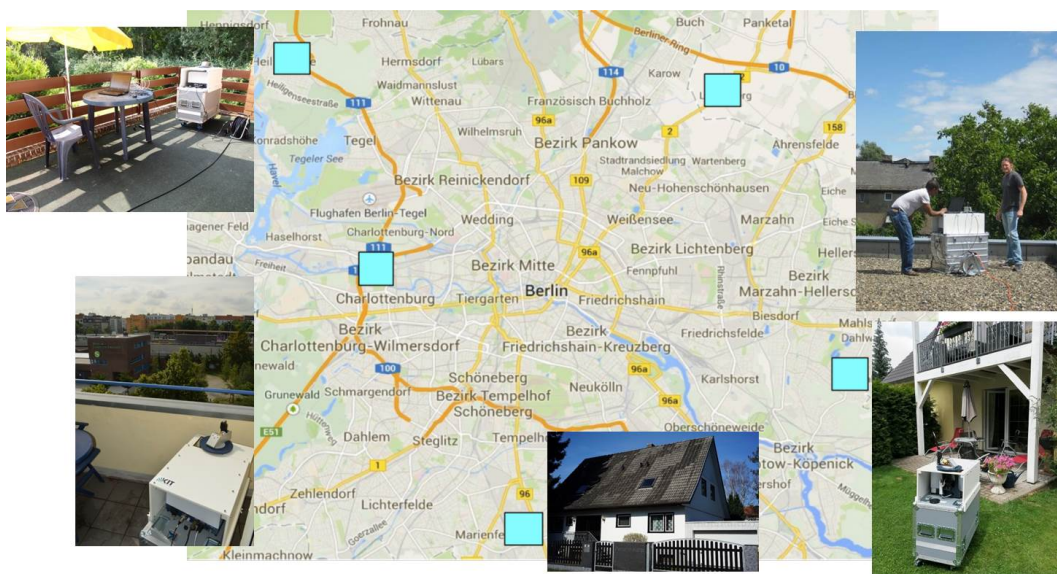


Figure 6.5: Map showing the measurement stations around Berlin together with pictures of the locations, mostly during operations. Map source: <http://www.maps.google.de/>.

Date	No. of observations					Quality	Wind speed [m s ⁻¹]	Wind direction
26 June 2014 (Th)	76	70	89	28	116	++	2-4	NNE
27 June 2014 (Fr)	273	233	237	186	182	++++	5	S-SSE
28 June 2014 (Sa)	0	37	0	0	0	+	7	SSW
01 July 2014 (Tu)	203	189	158	122	224	+++	8	W
02 July 2014 (We)	106	128	92	76	129	++	9	W
03 July 2014 (Th)	316	358	320	354	357	++++	7	W
04 July 2014 (Fr)	545	509	545	652	511	++++	7	SW-S
05 July 2014 (Sa)	0	93	0	0	0	+	5	SSW-SSE
06 July 2014 (Su)	329	265	346	252	385	+++	5	W-SW
07 July 2014 (Mo)	10	74	28	98	130	++	8	SE-NW
08 July 2014 (Tu)	0	21	0	0	0	+	6	NE-E
09 July 2014 (We)	35	29	40	0	10	+	6-10	E-SSW
10 July 2014 (Th)	248	306	411	188	245	+++	6-12-6	NE-E
11 July 2014 (Fr)	257	248	212	243	253	++	8	NE

Table 6.5: Main characteristics of each measurement day. The measurement date, number of observations at each site, wind speed and wind direction in the boundary layer are given. Additionally, a quality flag is provided, based on the overall temporal coverage and number of measurements (ranging from poor to perfect: +, ++, +++, +++++).

Table 6.5 summarises the data coverage and conditions for each site. The number of observations per day, wind speed and prevailing direction in the boundary layer as well as a quality ranking describing the quality of the measurement day (depending on the general data coverage) are given. As can be seen from the quality filter and also the measurement gap between 28 June 2018 and 01 July 2018, measurement conditions were not optimal over the whole course of the campaign. The best conditions prevailed on 27 June, 03 July and 04 July with measurements throughout the day. With 06 July also a Sunday is covered, interesting because of the possible different CO₂ emission pattern between weekdays and weekends due to different traffic characteristics. Throughout the campaign, the wind speeds were ranging mostly between 5 - 9 m s⁻¹, with prevailing westerly to southwesterly winds (as can be seen from Table 6.5, there are exceptions).

For the estimation of an emission strength, the knowledge of the boundary layer height is important. During the campaign, continuous measurements with a ceilometer were performed for this purpose by IMK-IFU in Berlin Neukölln (52.4895° N, 13.4309° E). The ceilometer CL51 from Vaisala GmbH is a mini-lidar system. Normally, ceilometers detect the cloud height, but with certain software packages up to five distinct height layers, including the planetary boundary layer, can be retrieved from vertical gradients of laser density backscatter data (Münkel et al., 2007). For sunny conditions, a prerequisite for EM27/SUN solar observations, with this method the boundary layer height can be determined very well. In Fig. 6.6 the ceilometer results for 27 June 2014 are depicted. During night, a stable nocturnal layer at 50 m can be seen, as well as the developing boundary layer during the day, with a height of around 2200 m in the afternoon. There were also radiosonde launches in Lindenberg providing relative humidity and virtual potential temperature profiles, which can in principle also be used for the estimation of the boundary layer (Emeis et al., 2012). As these were only performed twice a day, this information is too sparse to gain knowledge about the boundary layer. The radiosonde data were, however, used for the construction of temperature profiles, as will be explained in the next section.

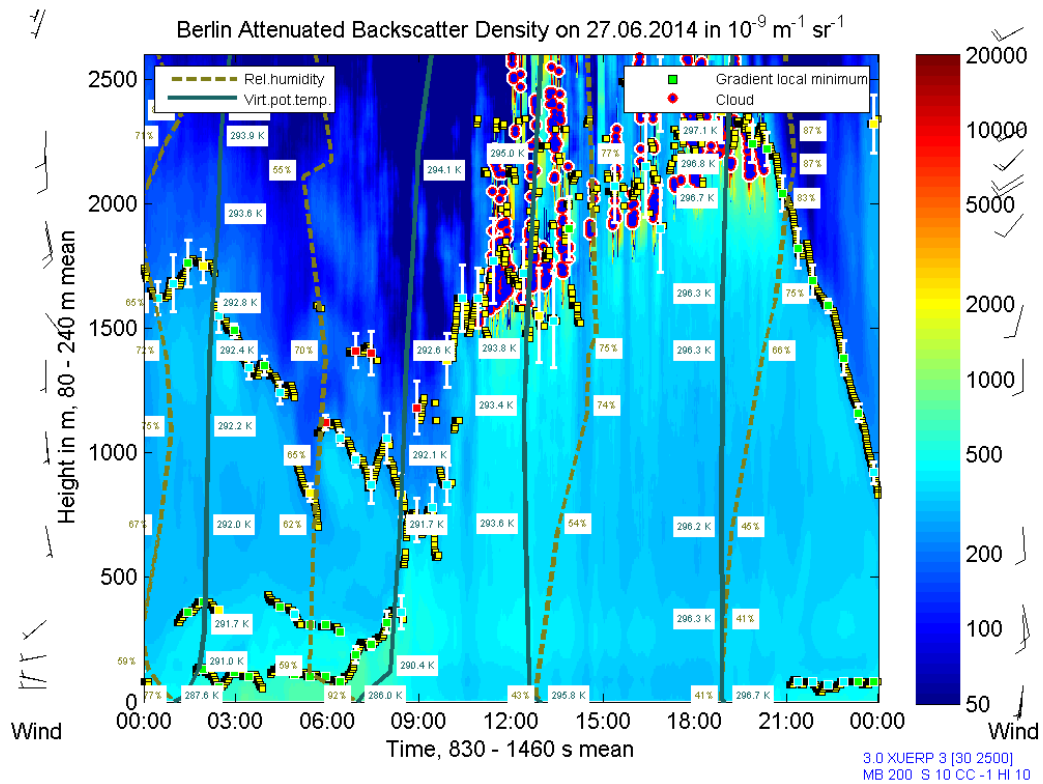


Figure 6.6: Ceilometer measurements showing the development of the boundary layer height on 27 June 2014 in Berlin-Neukölln. Ceilometer measurements were performed by IMK-IFU. Figure taken from Hase et al. (2015).

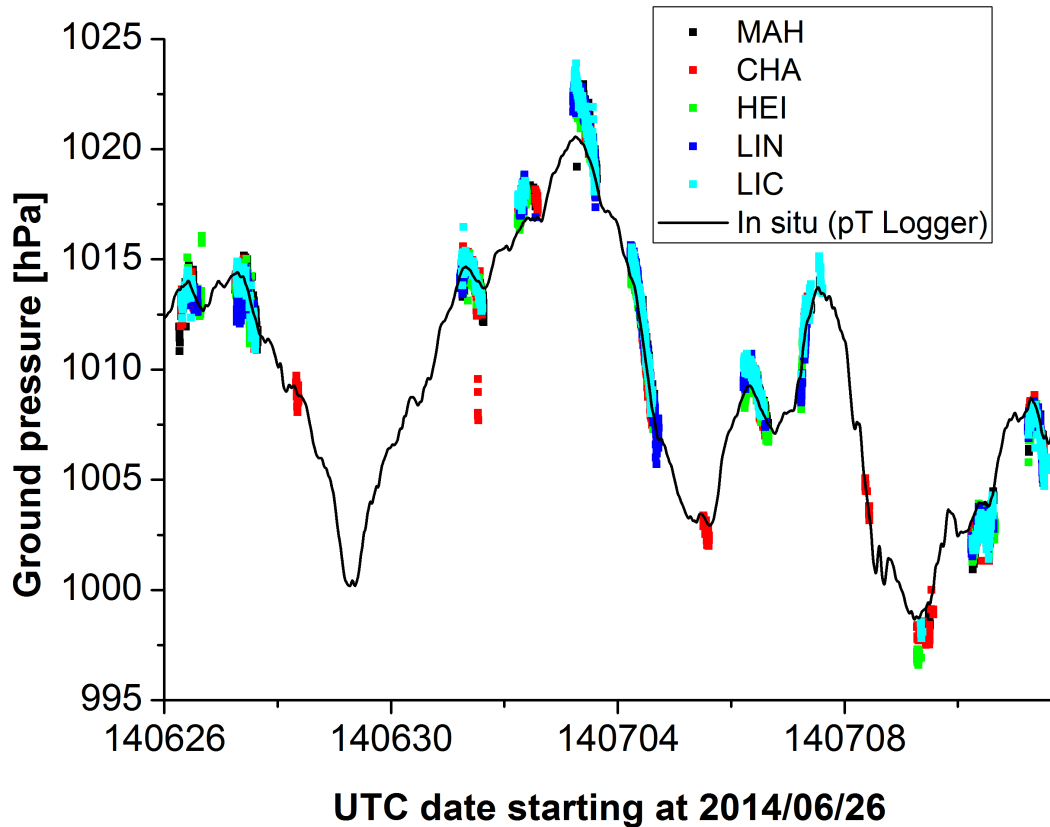


Figure 6.7: Time series of in situ pressure data from the MHB data logger measurements (black line, all sites have been merged to one time series) in comparison with spectroscopically derived pressure data (coloured squares), which have been calculated from total column amounts of O_2 and H_2O . All data have been reduced to a common height of 30 m. For better comparability, the spectroscopic data is scaled with a factor of 0.9713. Figure adopted from Hase et al. (2015).

6.3 Berlin X_{gas} measurements

The general measurement routine has been described in section 4.2, the calibration measurements prior to and after the campaign were analysed in section 6.1. For the construction of pressure profiles, ground pressure data from the MHB-382SD data logger are used, thereby providing an intraday variability. For the temperature profiles, NCEP model profiles together with radiosonde temperature data from the meteorological observatory Lindenberg are used. Starting point are the NCEP UTC noon profiles, for the height levels below 4 km a linear temperature increase is then applied resulting from the difference of the 12:00 and 18:00 LT radiosonde data. Above 4 km the original NCEP data is used, as the intraday changes are insignificant. One common pressure-temperature profile is applied for the analysis of the different stations, as the stations are situated within 25 km distance.

As a first sensitive measure of the agreement of the instruments, in Fig. 6.7 the ground pressure time series recorded by the MHB data loggers (the data from the five sites are merged to one averaged time series, reduced to a common reference altitude of 30 m) is compared to ground pressure data derived from the EM27/SUN measurements, where the analysis was performed according to section 6.1.3. The spectroscopic pressure was also reduced to a common height of 30 m. The interday and intraday pressure changes derived from the spectroscopic measurements

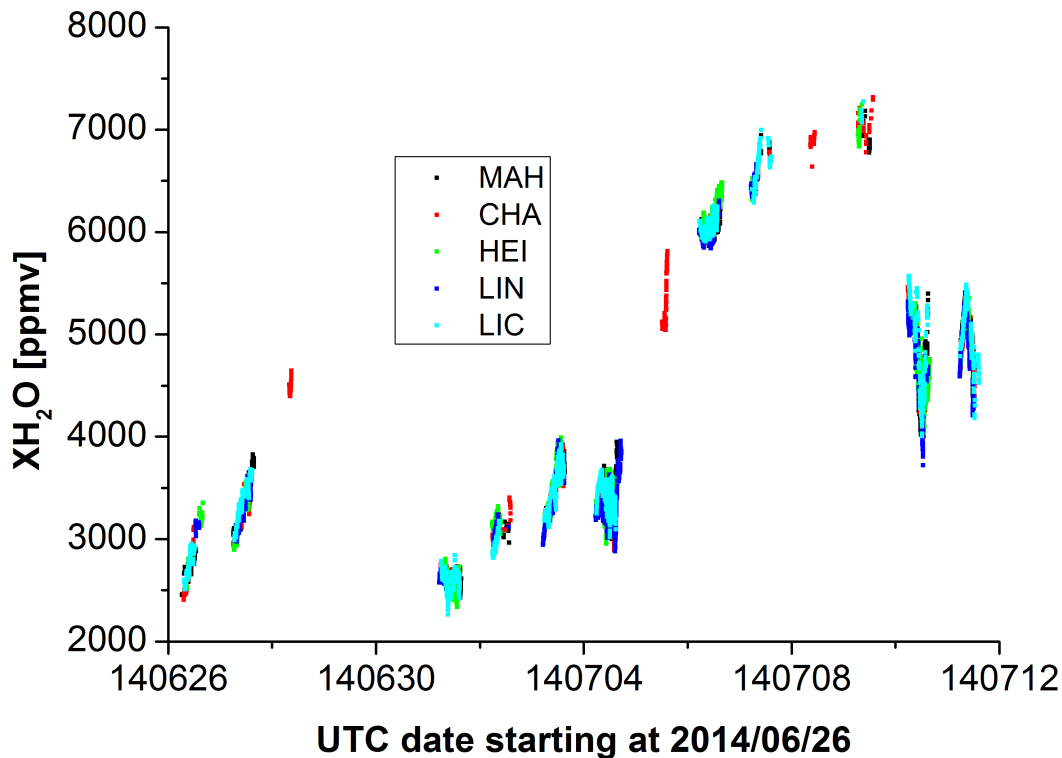


Figure 6.8: Time series of X_{H_2O} for the Berlin campaign from 26 June 2014 to 11 July 2014. The colours denote the different measurement sites. Figure adopted from Hase et al. (2015).

are in good agreement with the in situ measurements at all sites. There is a systematic offset between the in situ data and the spectroscopically derived values, this is why a scaling factor of 0.9713 was applied for the comparison. This factor is in good agreement with the calibration factor found for the calibration measurements, 0.9700, and also the factor found in Klappenbach et al. (2015), 0.9717.

Figures 6.8, 6.9 and 6.10 show the X_{H_2O} , X_{CO_2} and X_{CH_4} time series of different stations for the duration of the Berlin campaign. Focussing first on X_{H_2O} in Fig. 6.8, the time series of the different sites show the same pattern. The column averaged DMF ranges from 2000 ppmv to 7000 ppmv, a change by a factor of more than 3 during a two week period. Differences between the stations are negligible, demonstrating the uniform character of the probed area with respect to surface evaporation (localised sources of humidity would lead to larger differences between the sites). As the H_2O mainly stems from the boundary layer, this indicates that the selected area is well ventilated, justifying the use of a common pressure-temperature profile for all sites. Figs. 6.9 and 6.10 depict the time series of X_{CO_2} and X_{CH_4} , respectively. For both species, the largest variations, in the order of 1.0 - 1.5 %, are on the scale of several days due to synoptic changes and seen for all stations. Furthermore, there is a common intraday pattern for all sites, a mixture of real variability and artefacts of the analysis. While for X_{CO_2} it is sensible to attribute the decrease of roughly 0.5 % during the day to photosynthesis, for X_{CH_4} there are some symmetric features around noon common to all sites which seem to be artefacts of the retrieval. As discussed in section 4.2.3, a postprocessing was applied to correct the airmass dependency of the retrieval. However, this artefact partly stems from the smoothing error of the retrieval. As for this analysis constant a priori profiles were used, while the atmospheric profiles vary from day to day, part of the airmass dependency probably remains (and varies from day

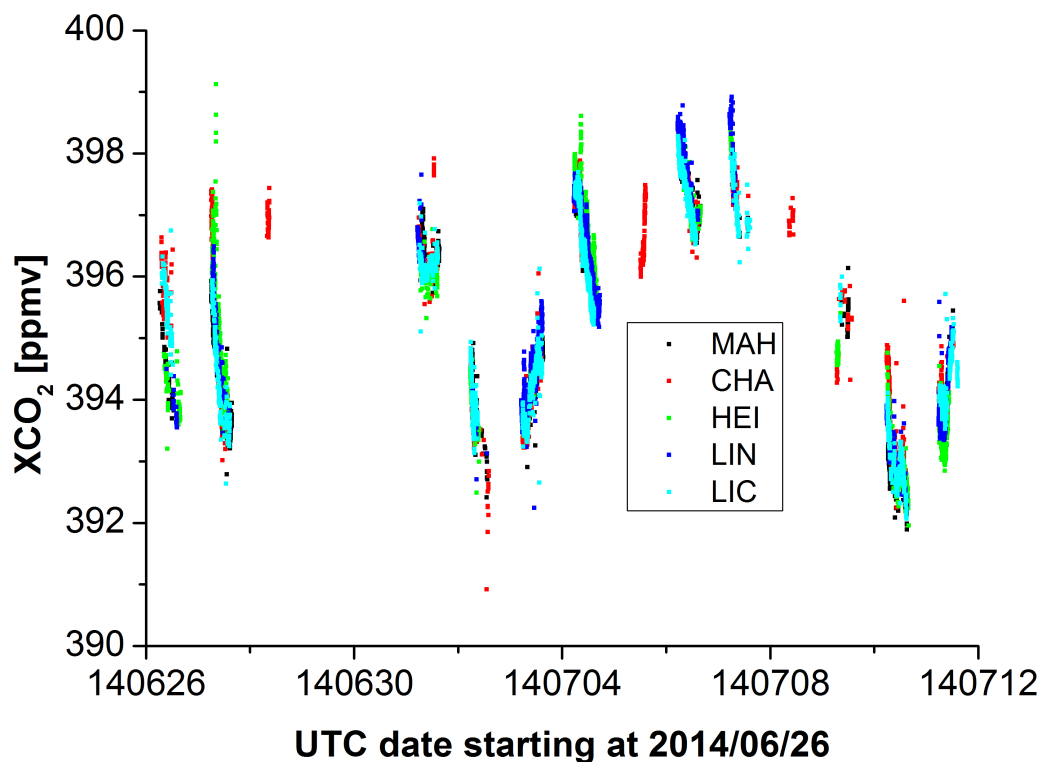


Figure 6.9: Time series of XCO₂ for the Berlin campaign from 26 June 2014 to 11 July 2014. The colours denote the different measurement sites. Figure adopted from Hase et al. (2015).

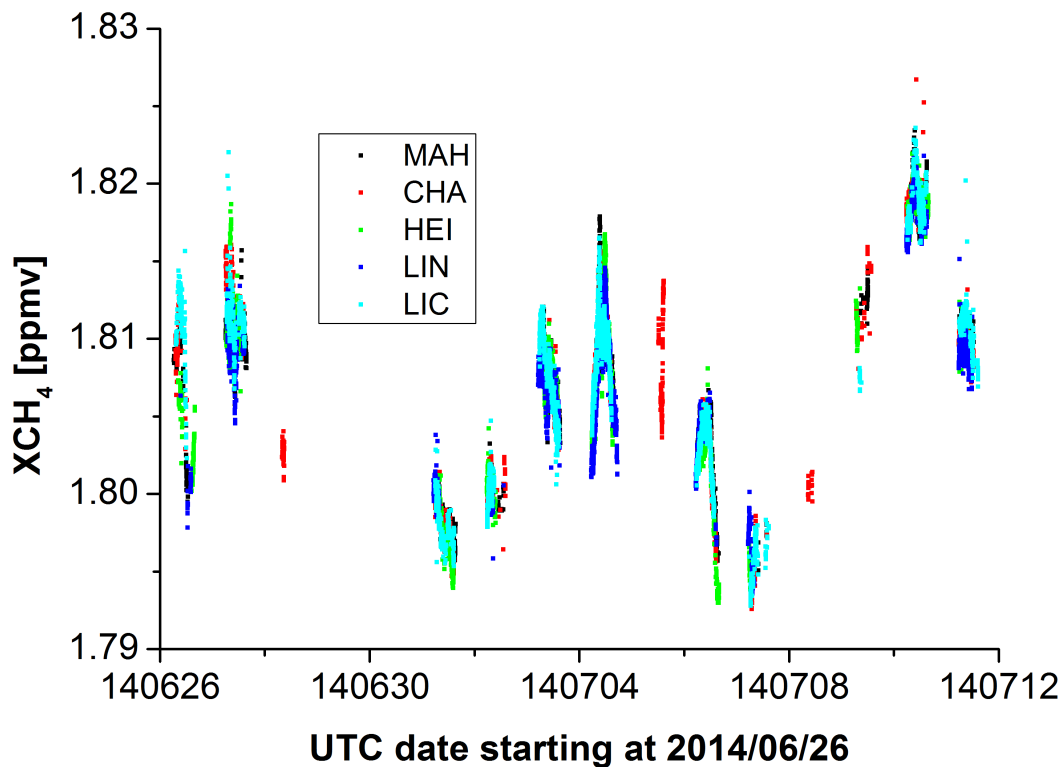


Figure 6.10: Time series of XCH₄ for the Berlin campaign from 26 June 2014 to 11 July 2014. The colours denote the different measurement sites. Figure adopted from Hase et al. (2015).

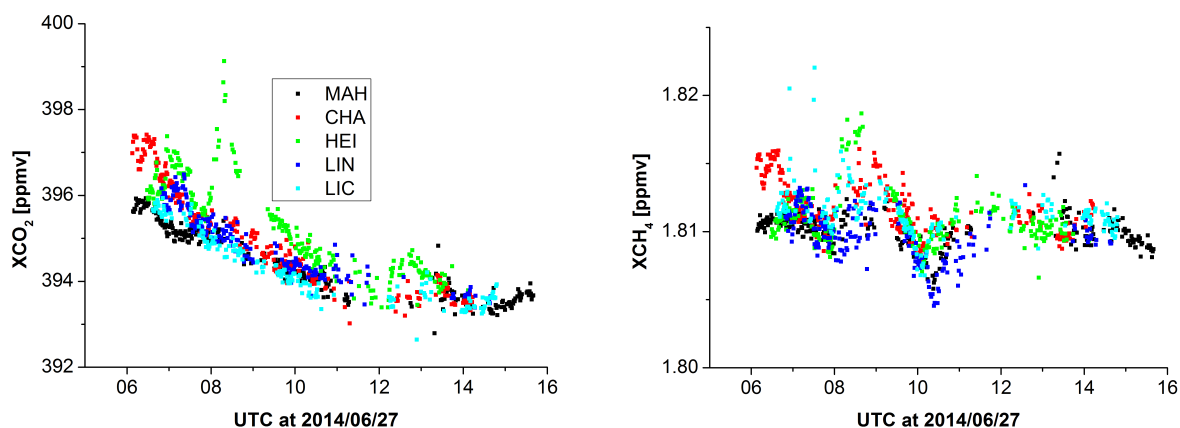


Figure 6.11: XCO₂ and XCH₄ measurements for 27 June 2014. For XCO₂, the Heiligensee station records enhanced XCO₂ values as compared to other stations. Figure adopted from Hase et al. (2015).

to day). Up to now, the discussed patterns were uniform for all sites. Additionally, there is a contribution in the order of 1 - 2 ‰ only seen at some stations and varying for the different days. This enhancement, though significantly smaller than the common intraday variability, can be unambiguously attributed to local emissions of CO₂ and CH₄. This is due to the rigorous calibration routine described in section 6.1 and the fact that all sites perform measurements under nearly the same elevation angle and similar atmospheric conditions, significantly reducing retrieval biases between the stations.

As an example day, in Fig. 6.11 XCO₂ and XCH₄ values for 27 June 2014 are depicted. Focussing first on XCO₂, the Heiligensee site sees clearly higher CO₂ concentrations when compared to the other sites, in the order of 1 %. Later this finding will be checked against a simple dispersion model. For the moment, qualitatively this makes sense as Heiligensee is the north western site, and the wind was coming from S - SSE according to Table 6.5. With this knowledge, it is also good to note that the two southern sites Mahlsdorf and Lindenberg show the lowest XCO₂ values, as would be expected under these meteorological conditions. For XCH₄ the overall variability during the day is higher as compared to XCO₂. This is not surprising, as there are rural sources of CH₄, dairy farms, around Berlin. Moreover, it is hard to attribute any CH₄ enhancements to the city of Berlin itself. To investigate this, a rather complex model would be needed, taking into account the many different sources of methane. In the following sections the focus lies on the attribution of CO₂ emissions with the help of a dispersion model.

6.4 Dispersion model

In order to estimate XCO₂ enhancements due to emissions from the Berlin city source, a dispersion model was developed by Frank Hase. The model separates the city of Berlin into five source regions, each with an individual emission strength. The geographical position and contribution of each area is given in Table 6.6, and a visual representation is shown in Fig. 6.12. Here the red areas denote the source regions according to Table 6.6, the white circles denote the positions of the different spectrometers. The spatial extent and the contribution are based on public data from the Statistical Office Berlin-Brandenburg².

²<http://www.stadtentwicklung.berlin.de>

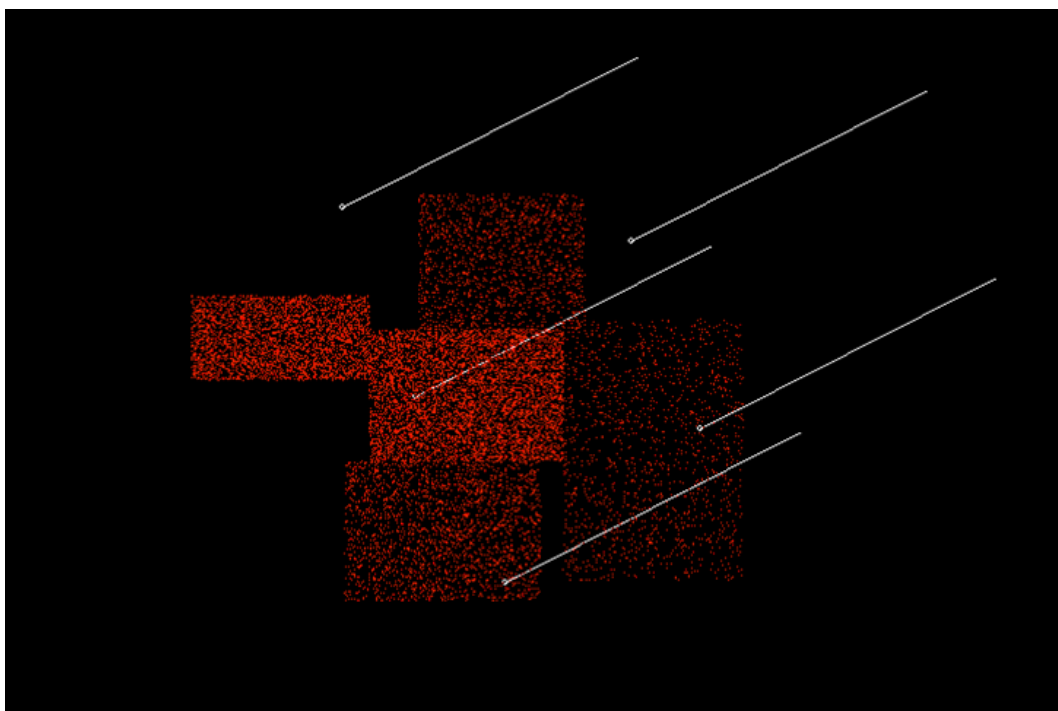


Figure 6.12: Visual representation of the dispersion model. The red areas denote the five source regions used in the model. The white circles show the position of the measurement sites, the white line represents the spectrometers line of sight at one time of the day.

Very important model input data are the wind fields. Here the COSMO-DE wind fields, the convective-scale regional component of the numerical weather prediction system of the German Weather Service (DWD) are utilised (Baldauf et al., 2011). The full resolution of COSMO-DE is $2.8 \text{ km} \times 2.8 \text{ km}$ horizontally with a temporal resolution of one hour. For this study, five wind profiles from the edges and the centre of a square centred on the observed Berlin area with an edge length of approximately 20 km are used. In between, the wind fields are linearly interpolated in time, while horizontally a Shepard inverse distance weighting with a power of 2 is applied (Shepard, 1968).

In this Lagrangian model, emitted particles are moved from their present locations according to the interpolated wind fields. For the particle creation the rate of generation is defined by the emission strength of the different source regions given in Table 6.6. Each new particle is randomly generated in one of the regions according to the contribution of the area. Inside the area, a particle creation position is chosen randomly with an equal probability for each area element. The vertical transport, a fast mixing over the whole boundary layer height in around 10 minutes is assumed, in the model is implemented with a fast erratic diffusion on the vertical axis. For the definition of the model boundary layer height, the ceilometer data presented in Fig. 6.6 is used. Fast variations in the boundary layer height on the time scale of minutes are not considered, only the overall development of the boundary layer during the day is taken into account. The ceilometer data were piecewise fitted linearly.

For the detection of the particles, the model analyses if the particle is inside a cylinder representing the line of sight of the EM27/SUN. As the variation of the line of sight during the day with respect to the investigated area is not negligible, the orientation of the cylinder is updated throughout the day with respect to astronomical calculations.

Box region	NW corner	SE corner	% contribution
Charlottenburg and Spandau	52.5677 13.0753	52.5159 13.2550	25
Tempelhof and Schönefeld	52.4657 13.2304	52.3800 13.4275	
Marzahn-Hellersdorf and Treptow-Köpenick	52.5531 13.4502	52.3927 13.6316	10
Reinickendorf and Pankow	52.6302 13.3046	52.5472 13.4721	
City centre	52.5472 13.2550	52.4657 13.4502	40

Table 6.6: Name, position and contribution in % of the five emission regions used in the dispersion model.

Simulations were run individually for all days starting midnight, no emissions from the previous day were considered. This is a sensible assumption, as normally the aged particles have left the region of interest, only for days with very low wind speeds the residence time of the particles might exceed 6 hours. Another scenario where particles from the previous day could be detected would be changing winds, this effect is also neglected here, particles are only followed up to a distance of 40 km from the city centre, from there on they are discarded. During each time step of 1 s, a particle is emitted and the other particles are transported. The detection of particles is performed for solar elevation angles above 20° along the line of sight of the spectrometer in periods of 450 s. Subject to the wind speed, between 20000 and 40000 particles are followed at one point in time. For the later comparison the simulations were run 500 times and then averaged, so that the statistical noise contribution is negligible. The atmospheric background concentrations of CO_2 are not accounted for in this model, only the enhancement due to the five source regions representing the Berlin city source is included.

6.5 Comparison of model predictions and EM27/SUN time series

For this comparison, the three measurement days with the best conditions according to Table 6.5 are investigated, 27 June, 03 July and 04 July. The results are depicted in Fig. 6.13. The source strength of Berlin is fixed to 800 kg s^{-1} , although in reality one would expect variable intraday emissions due to e.g. traffic, and also interday variations with a weekday weekend pattern. However, to include these effects is beyond the scope of the simple model used here. As the background CO_2 concentrations are not included in the model, for the comparison days the average values of the background stations were added to the model output. This approach only works for the first two days. On the third day, the upstream sites are too variable so that a constant value of 390 ppmv was superimposed.

The three days will be discussed individually. On 27 June, the model prediction agrees reasonably well with the observations. The enhancement in Charlottenburg from morning until noon is nicely reproduced. For Heiligensee, the first enhancement at 07:00 UTC is not captured in the model whereas the second enhancement from 08:00 UTC to 11:00 UTC is also seen by the model. The peak in the observations at 8:30 UTC is much sharper compared to the model, probably due to a localised source in the Berlin region. As discussed in the previous section, the model

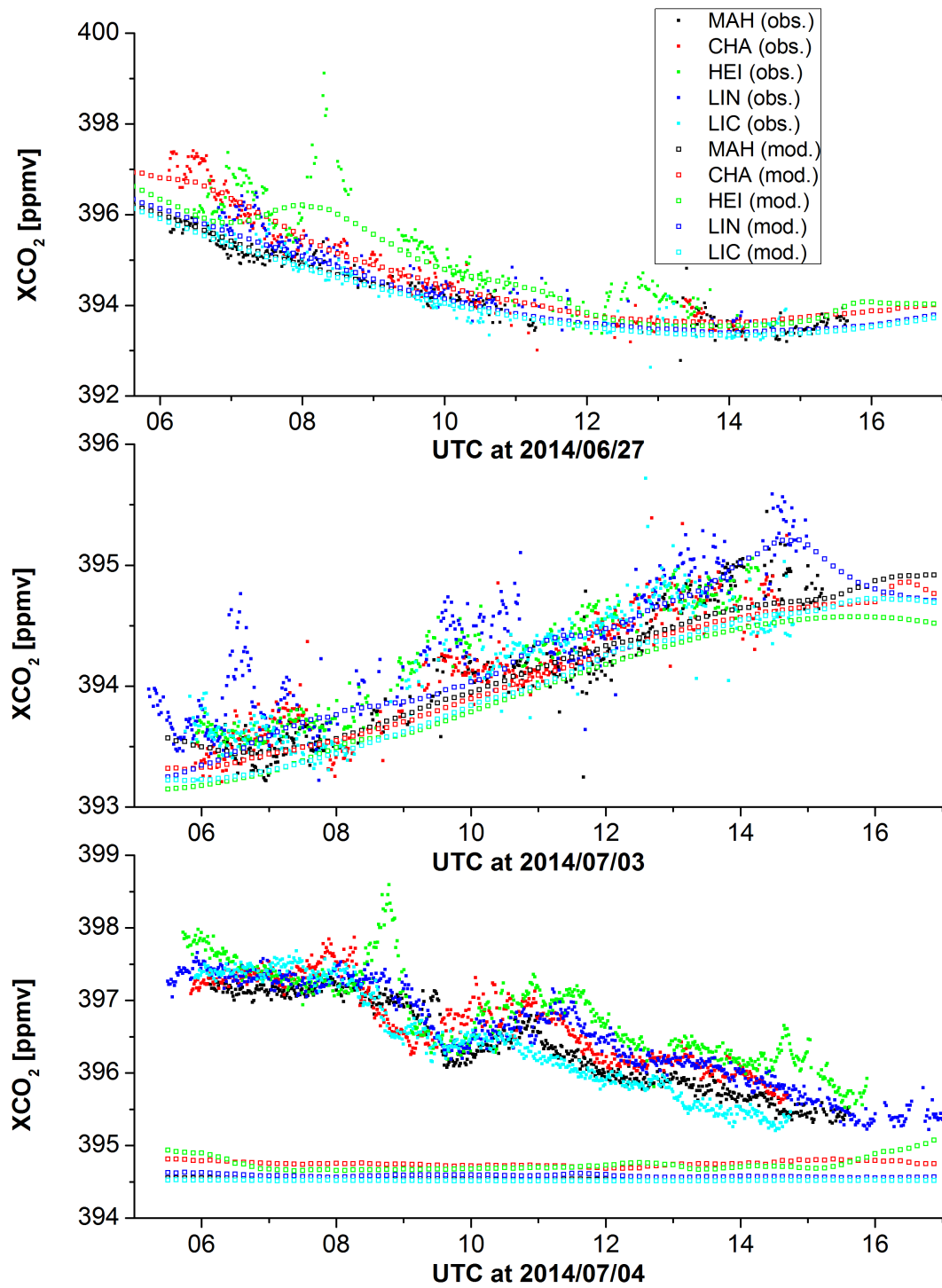


Figure 6.13: Observed and predicted XCO₂ for 27 June, 03 July and 04 July. For the first two days, the average of the upstream stations were added to the predicted XCO₂, for the third day, due to the varying background stations, a constant value of 390 ppmv was added. Figure adopted from Hase et al. (2015).

divides Berlin into five emissions regions and does not take point sources into account, thereby it is not expected to reproduce these very localised emissions. Prevailing winds on 27 June were from the south so the enhancements in the Heiligensee observations most likely stem from the Charlottenburg and Spandau region. There is a heat- and power-generating coal-fired plant named Reuter West³ with a peak thermal power of 774 MW in this area. It seems reasonable to assume that this is the source of the sharp enhancement seen in the Heiligensee observations. Later in the day at around 13:00 UTC the model fails to reproduce another enhancement in Heiligensee. Although not very pronounced, the model also predicts an enhancement for the Lindenberg site in the morning, which is supported by the observations.

On 03 July the enhancements are smaller than on 27 June. This is in accordance with the finding that the wind speed on 03 July is higher, so that lower enhancements at the downwind site would be expected. Increases at the Lindenberg site can be seen both in the model and in the observations. While the observations show pronounced peaks at 06:30 UTC and 10:00 UTC, the model enhancements are smeared out and also show a time lag of approximately half an hour compared to the observations. The last increase is very well reproduced by the model. For the other stations the agreement between model and observations is not convincing. While the observations show small enhancements for the Heiligensee and Lichtenrade sites at different times of the day, the model predicts these stations to be background stations throughout the entire day. Westerly winds prevailed on this day, so that the enhancement at the Lichtenrade site can probably be attributed to emissions from Potsdam, which are not included in the model. The bottom graph of Figure 6.13 shows the measured and predicted XCO₂ values for 04 July. Wind direction changed from south west in the morning to south later in the day. This change is one reason for the varying background stations. These variations inhibit the construction of a common background value from the observations. For this day, a fixed background value of 390 ppmv was used. In general, the observations on this day show a large variability, which is not seen by the model predictions. An M-shaped curvature lasting 5 hours from early morning to noon, common at all sites, dominates the scene. This disturbance first appears at the upwind stations Lichtenrade and Charlottenburg, and with a time lag of about 45 minutes at the downwind stations Lindenberg and Heiligensee. This time lag coincides almost perfectly with a disturbance of the background XCO₂ signal being advected with the wind speed of this day, 7 m s⁻¹, across the distance between upwind and downwind stations, approximately 20 km. The model predicts an enhancement of around 0.5 ppmv for the Charlottenburg and Heiligensee stations. However, due to the strongly varying background, a sensible comparison with the observations is not possible.

04 July shows the limitations of the simple dispersion model used in this study. The background XCO₂ signal is not modeled, only regional emission sources, so that the analysis of a complex atmospheric scene as seen on 04 July is very difficult. For a thorough investigation of the Berlin campaign data set, highly refined models are needed. This kind of analysis will be presented in chapter 7. There another measurement campaign conducted in the Paris megacity 2015 is analysed utilising a complex chemical transport model.

³<https://powerplants.vattenfall.com/de/reuter-west>

6.6 Conclusions

In this chapter, the first worldwide case study using a set of EM27/SUN spectrometers for the quantification of GHG emissions from a local source is presented. The outstanding network precision of the instruments is demonstrated. This high degree of precision and stability allows the non-ambiguous detection of small gradients superimposed over background concentrations of around 400 ppmv between measurement sites during the campaign. After a description of the general campaign design the results of the campaign are presented, where XCO₂ gradients between upwind and downwind sites are mostly between 1 - 2 ‰ XCO₂. The measurement results are compared with a Lagrangian dispersion model, which uses high resolution wind fields from the convective-scale regional component of the numerical weather prediction system of the German Weather Service with a full resolution of 2.8 km × 2.8 km horizontally and a time resolution of one hour. Using the EM27/SUN measurements in conjunction with the model, the emission strength of Berlin is estimated to amount to approximately 800 kg s⁻¹ or 25 Mt year⁻¹.

Chapter 7

Paris campaign

In chapter 6 a first test campaign utilising five EM27/SUN spectrometers is described and analysed. Using the measurement results in conjunction with a simple dispersion model a CO₂ emission strength for Berlin is derived. However, the limitations of this simple model are apparent. The background CO₂ is not modelled and in the model Berlin only consists of five emission areas, an admittedly coarse choice.

In this chapter, a campaign with the aim to investigate the CO₂ emission strength of the Paris megacity is discussed. For this campaign, the measurement results are compared with the high resolution state of the art CHIMERE atmospheric chemistry transport model (Menut et al., 2013). CHIMERE encompasses a highly resolved emission inventory of the Paris region, which will be verified using the five EM27/SUN that were also deployed for the Berlin campaign. The results of this campaign have been published in Vogel et al. (2018), from which parts were adopted for this chapter.

7.1 Campaign design

For the Paris field campaign from 28 April to 12 May 2015 five portable EM27/SUN FTIR spectrometers were positioned in the Parisian Ile-de-France region and within the city of Paris. The campaign was conducted in early spring. At this time of the year the cloud cover is typically low. Additionally, the time between sunrise and sunset is more than 14 hours. Similar to Berlin, the topography is relatively flat and the city is isolated which simplifies the interpretation of the measurements. The campaign is a French German collaboration between KIT, Laboratoire des Sciences du Climat et de l'Environnement (LSCE), Laboratoire Inter-Universitaire des Systèmes Atmosphériques (LISA) and Laboratoire d'Études du Rayonnement et de la Matière en Astrophysique et Atmosphères (LERMA).

Approximately 11 million people live in the Paris metropolitan area with about 2.2 million inhabiting the Paris city centre. With around 1,000 people per km² in the metropolitan area and over 21,000 people per km² in the city of Paris (INSEE 2016¹), it is by far the most densely inhabited region in France. The predicted CO₂ emissions from the Ile-de-France region are 39 Mt year⁻¹. Largely responsible for this total emission strength are on-road traffic emissions and residential and the tertiary sector (accounting for over 75 %). Minor contributors below 10 % include other sectors such as industrial sources and airports (AIRPARIF 2016²). To optimally position the instruments it is important to recognise the spatial distribution of these CO₂ emission sources. In order to accomplish this, the Institut für Energiewirtschaft und Rationelle Energieanwendung

¹<https://www.insee.fr/en/accueil>

²https://www.airparif.asso.fr/_pdf/publications/inventaire-emissions-idf-2012-150121.pdf

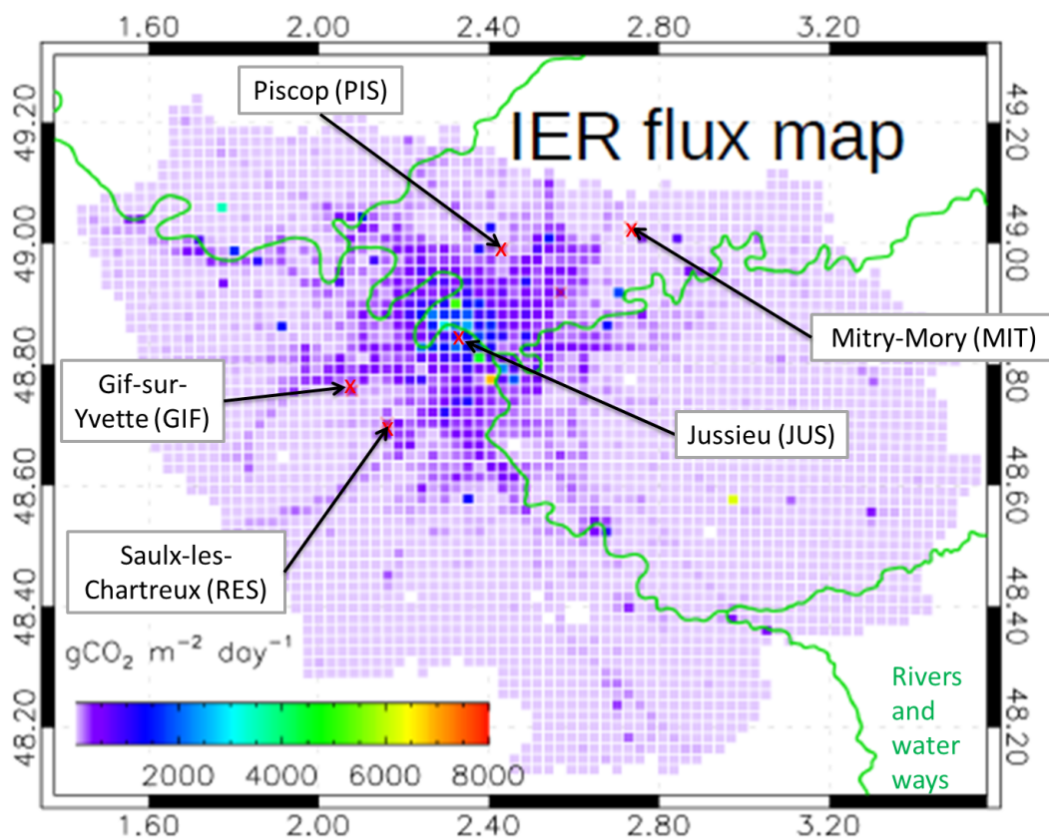


Figure 7.1: CO₂ emission map of the Paris metropolitan region as reported by the IER emission inventory (Latoska, 2009). The spatial resolution of the inventory is 1 km × 1 km. The red crosses denote the EM27/SUN measurement sites during the Paris campaign in April/May 2015. The increased emission values in the Paris city centre around the Jussieu site are clearly visible. Strongly enhanced single pixels are point sources, e.g. oil refineries, power plants and airports. Figure taken from Vogel et al. (2018).

(IER) emission model with a 1 km × 1 km resolution for France (Latoska, 2009) is used, which is based on the available activity data. These include e.g. traffic counts, housing statistics and energy use. The temporal resolution is implemented following Vogel et al. (2013). In summary, by rescaling the total emissions of the IER model were matched with the temporal components for the various emission types in accord with acknowledged national temporal emission profiles.

Whereas for the Berlin campaign the spectrometers were placed in a circle around the city centre, for this campaign a different spatial deployment was chosen. For the optimal quantification of urban XCO₂ emissions the EM27/SUN spectrometers were positioned along the typical dominant wind directions in the Ile-de-France region in April and May i.e. southwest (Staufner et al., 2016) to be able to measure upwind and downwind air masses. For a visual representation, see Figure 7.1. The stations Gif-Sur-Yvette (GIF) and Saulx-les-Chartreux (RES) are positioned in the southwestern part of the Ile-de-France region, the Jussieu (JUS) site is located directly in the city centre. The high emission region encompasses the city centre and stretches out northwards and eastwards. The two northeasterly stations Piscop (PIS) and Mitry Mory (MIT) were placed downwind of the emission region. Apart from this general emission pattern, some strongly enhanced pixels are visible in the emission map, which can be attributed to point sources, in this

Location	ID	Latitude (° N)	Longitude (° E)	Altitude (m)
Mitry-Mory	MIT	48.984	2.626	65
Gif-Sur-Yvette	GIF	48.708	2.148	162
Piscop	PIS	49.019	2.347	143
Saulx-les-Chartreux	RES	48.688	2.284	90
Jussieu	JUS	48.846	2.356	62

Table 7.1: Coordinates and altitudes of the measurement sites during the Paris field campaign. Coordinates were derived from GPS sensors. The altitudes were derived from topographic data (<https://www.sonnenverlauf.de>).

case an oil refinery (yellow dot far south east), the airport Paris-Orly (yellow dot a bit south east of the Paris city centre) and a gas-fired power plant (green dot in the far north west). The Charles de Gaulle airport is just outside the region the emission map encompasses. Coordinates and altitude of the different stations are given in Table 7.1. Measurements routinely began 5:00 - 6:00 UTC and continuously observed XCO₂ until 17:00 - 18:00 UTC.

7.2 The atmospheric chemistry transport model CHIMERE

For this study, the chemistry transport model CHIMERE is used (Menut et al., 2013) to model CO₂ emissions in the Ile-de-France region. Currently, there is no CH₄ emission module implemented for CHIMERE, so that the comparison focuses on CO₂. The time step of the model is 10 minutes and hourly output is provided. The horizontal grid, or spatial resolution, is depicted in Fig. 7.2. For the main region of interest, the Paris city centre, the resolution is 2 km × 2 km. In the outer model domain, the resolution becomes coarser, first 2 km × 10 km and then 10 km × 10 km at the edges of the model domain, which overall consists of 118 × 118 pixels corresponding to an area of 500 km × 500 km. CHIMERE features 20 terrain-following pressure levels up to a pressure of 500 hPa, thereby ranging from the surface to the middle of the troposphere. The model uses operational meteorological reanalysis data from the European Centre for Medium Range Weather Forecast (ECMWF) Integrated Forecasting System with a temporal resolution of three hours and a horizontal resolution of 15 km × 15 km. Prior work by Staufer et al. (2016) showed that the resulting wind speeds and directions in the CHIMERE model are in excellent agreement with meteorological observations. The model does not account for the special topography of the city area and it was found in a prior study (Bréon et al., 2015) comparing this CHIMERE setup with a model including a special surface parameterisation in the city area (Lac et al., 2013) that the above mentioned effect is negligible.

Opposed to the model setup described in Bréon et al. (2015) and Staufer et al. (2016), in this model run no atmospheric data is assimilated, in other words the simulations are based on a forward run from 25 April to 12 May 2015. The simulation starts some days before the campaign because in the initialisation phase the model results are prone to artefacts. For the Parisian region the anthropogenic fossil fuel (FF) CO₂ emissions are based on the IER inventory depicted in Fig. 7.1. Outside the Paris area, the FF emissions in the CHIMERE domain are based on the Emission Database for Global Atmospheric Research (EDGAR) V4.2 database for the year 2010 available at 10 km × 10 km resolution (Janssens-Maenhout et al., 2012). EDGAR provides annual mean fluxes and does not take a diurnal or seasonal cycle into account. The net ecosystem exchange (NEE), the natural fluxes, used here are provided by the land surface component of the ECMWF forecasting system, C-TESSSEL (Boussetta et al., 2013) with a temporal and spatial resolution of 3 hours and 15 km × 15 km, respectively. For the CO₂ boundary conditions at the

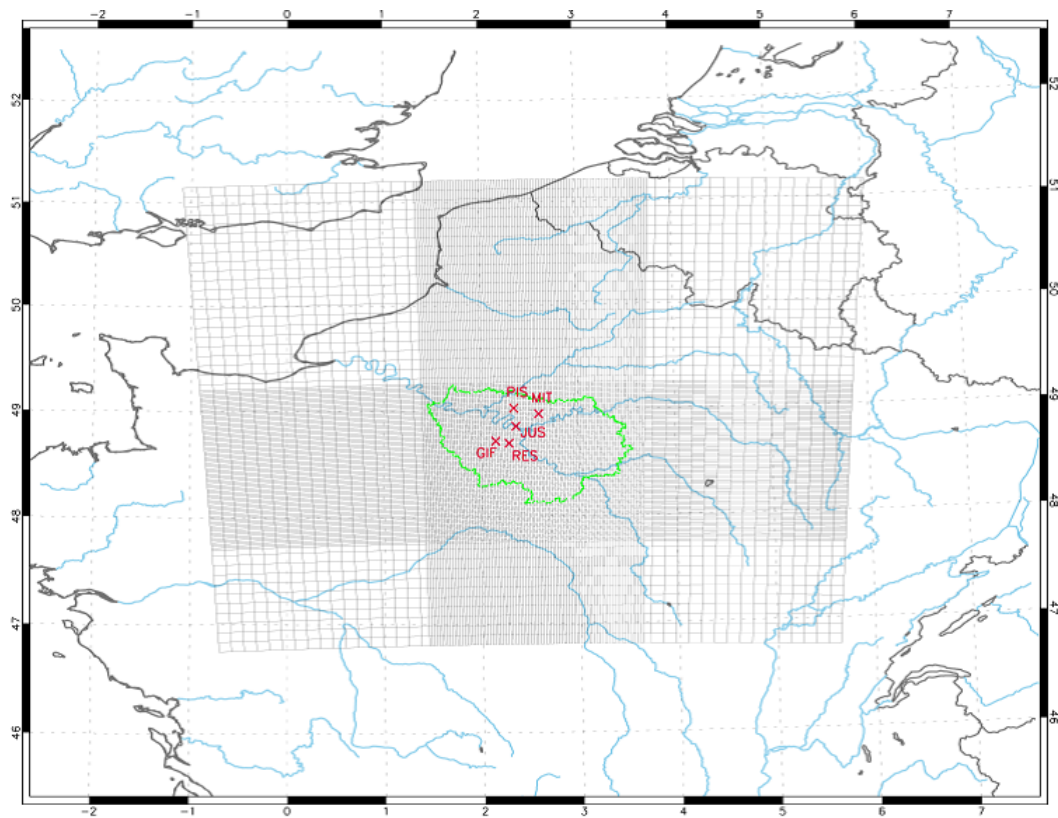


Figure 7.2: Map of the CHIMERE modelling domain showing the different horizontal resolution in the different regions of the domain. The boundaries of the IER emission inventory are shown in green. Red crosses denote the measurement sites. Figure adopted from Bréon et al. (2015).

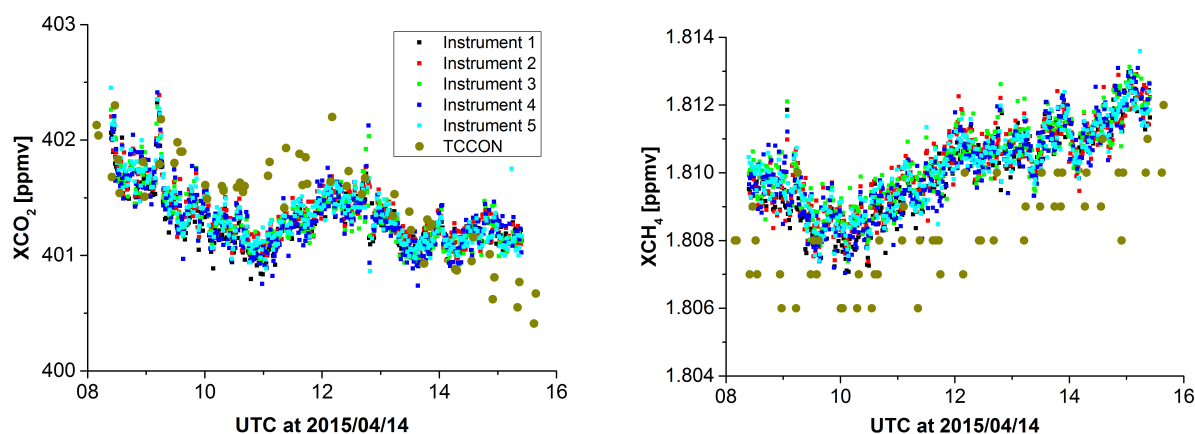


Figure 7.3: Calibrated XCO_2 and XCH_4 values for the EM27/SUN spectrometers participating in the Paris campaign on 14 April 2015. Golden dots show data from a co-located TCCON instrument.

border of the CHIMERE model domain and the initial CO_2 concentrations the CO_2 forecast by the Copernicus Atmosphere Monitoring Service (CAMS³) with a $15\text{ km} \times 15\text{ km}$ global resolution is utilised (Agustí-Panareda et al., 2014).

Due to the fact that the upper boundary of the CHIMERE model is at 500 hPa, to derive XCO_2 data, the CAMS CO_2 forecasts from 500 hPa up to the TOA are added to the CHIMERE CO_2 simulations. Model simulations for this study were performed by Johannes Stauer from LSCE.

7.3 Calibration measurements

As mentioned before, the five EM27/SUN used during this campaign were also deployed during the Berlin campaign. Therefore, the O_2 , XCO_2 and XCH_4 calibration factors deduced before (seven days between 09 and 23 April 2015) and after (18 and 21 May 2015) the Paris campaign will also be compared against the calibration factors found for the Berlin campaign to further investigate the instrumental stability of the EM27/SUN. The measurement routine for the calibration measurements as well as the processing of the interferograms has been performed exactly as described in chapter 6. The O_2 , XCO_2 and XCH_4 calibration factors are given in Table 7.2. "before" and "after" denote calibration measurements before or after the campaign, "all" encompasses all measurements. The instrumental stability is remarkable, all calibration factors for the Paris campaign are within 1σ precision with respect to the factors found for the Berlin campaign. The biggest change in the calibration factor is observed for XCH_4 for instrument 4 with a drift of 0.0005 or 0.9 ppbv, respectively. Due to the impressive stability of this ensemble over one year the calibration factors found for the Berlin campaign are also used for the Paris study.

One day of the calibration measurements is shown in Fig. 7.3. Golden dots denote measurements from the TCCON Karlsruhe instrument. The diurnal variation of the EM27/SUN measurements matches the TCCON daily cycle for XCO_2 and XCH_4 . For this comparison, the global calibration factor derived from the 3.5 years long time comparison presented in chapter 5 was applied to scale the EM27/SUN results to the TCCON results. There is a small offset between TCCON and the EM27/SUN measurements, which is not unexpected as the long term comparison showed a seasonal variability of the difference between the two data sets, see Fig. 5.1.4 and 5.1.5.

³<http://atmosphere.copernicus.eu>

Instr.	O ₂ all Berlin	O ₂ before Paris	O ₂ after Paris	O ₂ all Paris
2	0.9998 (0.05)	0.9995 (0.04)	0.9997 (0.03)	0.9995 (0.04)
3	1.0003 (0.03)	1.0000 (0.05)	1.0002 (0.07)	1.0001 (0.05)
4	1.0019 (0.05)	1.0015 (0.04)	1.0013 (0.03)	1.0015 (0.04)
5	1.0011 (0.03)	1.0014 (0.04)	1.0014 (0.03)	1.0014 (0.04)
Instr.	XCO ₂ Berlin	XCO ₂ before Paris	XCO ₂ after Paris	XCO ₂ all Paris
2	0.9992 (0.03)	0.9991 (0.03)	0.9992 (0.03)	0.9992 (0.03)
3	1.0002 (0.03)	1.0001 (0.04)	1.0000 (0.05)	1.0001 (0.05)
4	0.9999 (0.03)	1.0000 (0.04)	1.0000 (0.04)	1.0000 (0.04)
5	0.9996 (0.03)	0.9995 (0.03)	0.9995 (0.03)	0.9995 (0.03)
Instr.	XCH ₄ Berlin	XCH ₄ before Paris	XCH ₄ after Paris	XCH ₄ all Paris
2	0.9994 (0.03)	0.9995 (0.03)	0.9994 (0.03)	0.9995 (0.03)
3	0.9997 (0.04)	0.9999 (0.05)	0.9999 (0.03)	0.9999 (0.05)
4	0.9988 (0.03)	0.9993 (0.04)	0.9994 (0.04)	0.9993 (0.04)
5	0.9990 (0.03)	0.9989 (0.04)	0.9990 (0.03)	0.9990 (0.04)

Table 7.2: O₂, XCO₂ and XCH₄ calibration factors for the different EM27/SUN with respect to instrument 1. Measurements were performed in Karlsruhe during April and May 2015. Between April and May, the spectrometers were transported for the Paris campaign measurements. Values in parentheses denote the percent 1 σ precision of the ratio.

7.4 Campaign results

The campaign took place from 28 April to 13 May 2015 in the greater Paris region. Table 7.3 sums up the main characteristics and meteorological conditions during the campaign. It gives the number of observations at each site, wind speed as well as wind direction in the boundary layer. To guide the eye, an overall quality flag for each day of observation is provided. Meteorological conditions were not favourable for measurements during a large part of the campaign, as can be seen directly from the data gap between 29 April and 04 May, when it was cloudy and rainy. Also for other days (e.g. 04 May until 06 May) conditions were not optimal, with a cloudy and turbid scene. Despite these complications, throughout the campaign over 10000 interferograms were recorded, the best measurement period being between 07 May and 12 May. The dominant wind directions were southwesterly with low synoptic variations. The windspeed is over 3 m s⁻¹ during essentially the whole campaign period. A windspeed of above 3 m s⁻¹ has been identified as the meteorological condition under which the CHIMERE model performs best (Bréon et al., 2015; Staufer et al., 2016).

7.4.1 Measurement results

The procedure for processing of the interferograms has been explained before, see section 4.2.3. The only difference here is the construction of the temperature profiles utilising the ECMWF operational analysis data also used by the CHIMERE model, to be consistent with the model and avoid an artificial bias.

Figure 7.4 and 7.5 show the time series of the observed XCO₂ and XCH₄ during the Paris campaign. Focussing first on XCO₂, it ranges from 397 ppmv to 405 ppmv. A similar general pattern as seen for the Berlin campaign is observed. A diurnal variation with a strong decrease is observed at all sites due to uptake of CO₂ from the biosphere. Moreover, synoptic interday

Date	No. of observations					Quality	Wind speed [m s ⁻¹]	Wind direction
28 Apr 2015 (Tu)	179	102	178	199	234	++	2-4	W
29 Apr 2015 (We)	110	124	0	161	53	+	5	SW-W
04 May 2015 (Mo)	194	85	96	163	83	+	7	S-SE
05 May 2015 (Tu)	77	27	85	185	92	+	8	S-SW
06 May 2015 (We)	81	88	87	139	0	+	9	SW
07 May 2015 (Th)	169	313	252	286	238	+++	7	SW
09 May 2015 (Sa)	179	0	181	289	149	++	7	W
10 May 2015 (Su)	325	478	362	542	282	++++	5	S
11 May 2015 (Mo)	410	431	251	298	413	++++	5	SSW
12 May 2015 (Tu)	324	222	230	326	203	+++	8	NNW
13 May 2015 (We)	159	18	182	28	56	+	6	NE

Table 7.3: Main characteristics of each measurement day. The measurement date, number of observations at each site (MIT, GIF, PIS, RES, JUS), wind speed and wind direction in the boundary layer are given. Additionally, a quality flag is provided, based on the overall temporal coverage and number of measurements (ranging from poor to perfect: +, ++, +++, +++++).

differences are observed common to all sites. On top of these patterns uniform at all sites, there are enhancements seen at the downwind stations in the order of 2 - 4 ‰, differing from day to day, which are attributed to the emission of CO₂ by the Paris source. For XCH₄, ranging from 1.79 ppmv to 1.84 ppmv, the situation is nearly identical, see Fig. 7.5.

To investigate the influence of the Paris emission source, the intraday variability of XCO₂ and XCH₄ for 07 May 2015 and 10 May 2015 are shown in Fig. 7.6. For 07 May southwesterly winds prevailed, in compliance with the Mitry Mory site showing enhanced XCO₂ and XCH₄ values with gradient strengths of $\Delta XCO_2 \approx 1.3$ ppmv and $\Delta XCH_4 \approx 6$ ppbv. For Piscop and Jussieu the enhancement is halved with respect to Mitry Mory. As Jussieu is directly in the city centre, it would also be expected to record approximately the halved enhancement with respect to the downwind stations. The background sites Gif-Sur-Yvette and Saulx-les-Chartreux show nearly identical values, as expected. For this day, the enhancement patterns is almost similar for XCO₂ and XCH₄. A difference is that the Piscop site shows an enhancement throughout the day for XCH₄, while for XCO₂ the enhancement builds up only at late morning (09:00 UTC).

On 10 May southerly winds prevailed. For XCO₂ the Piscop site, being downwind of the Paris urban area, shows the largest enhancements starting from 12:00 UTC. In the morning before noon, measurements especially in PIS are sparse due to clouds. With respect to the background sites GIF and RES, also MIT and JUS show enhancements. For this day, XCH₄ shows a large variability at all sites. The most prominent feature is an M-shaped enhancement seen first at the background stations and approximately one hour later at MIT and PIS. The distance between the downwind and upwind stations is about 35 km, so a velocity of 10 m s⁻¹ is needed to travel this distance in one hour. The surface wind speed derived from the CHIMERE model is only around 2 m s⁻¹, so the detected air mass probably originates from higher altitudes. Furthermore, it is interesting to note that opposed to XCO₂, PIS does not show higher enhancements with respect to JUS and MIT. This hints to the assumption that sources of CO₂ and CH₄ differ and are not spatially identically distributed.

A quantitative analysis of the measured gradients ΔXCH_4 is not possible because the CHIMERE model does not encompass a CH₄ module at the moment. As a qualitative approach, the CH₄ emission flux for Paris is estimated using a simple differential column model:

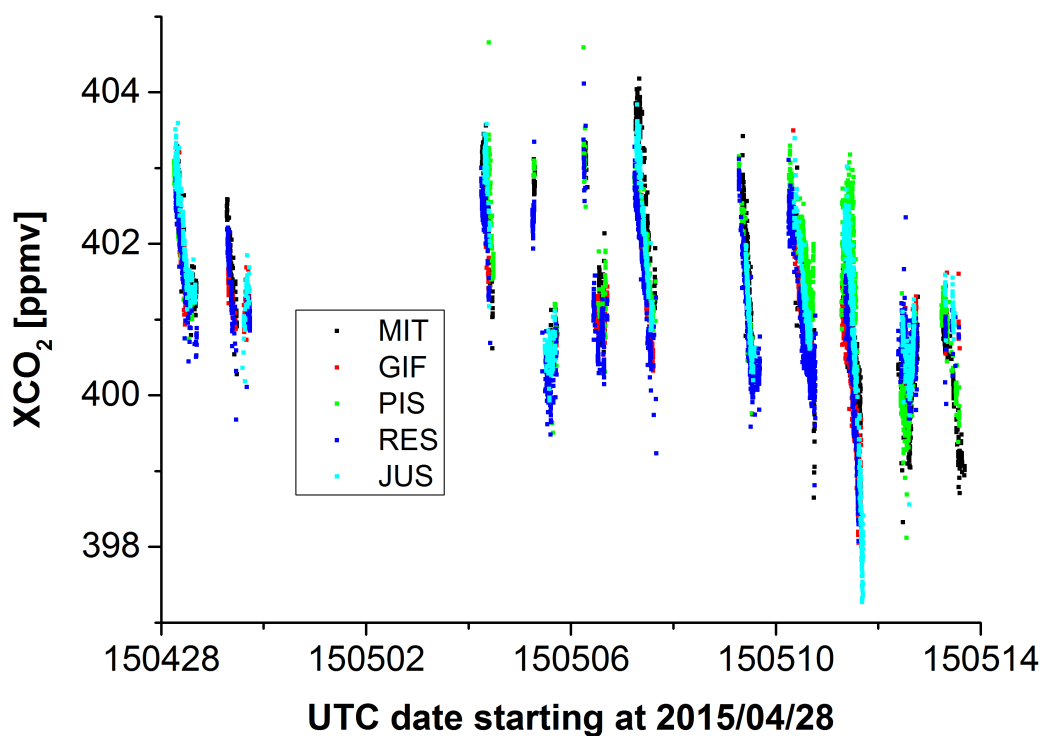


Figure 7.4: Time series of observed XCO_2 for the Paris campaign from 28 April 2015 to 13 May 2015. The colours denote the different measurement sites.

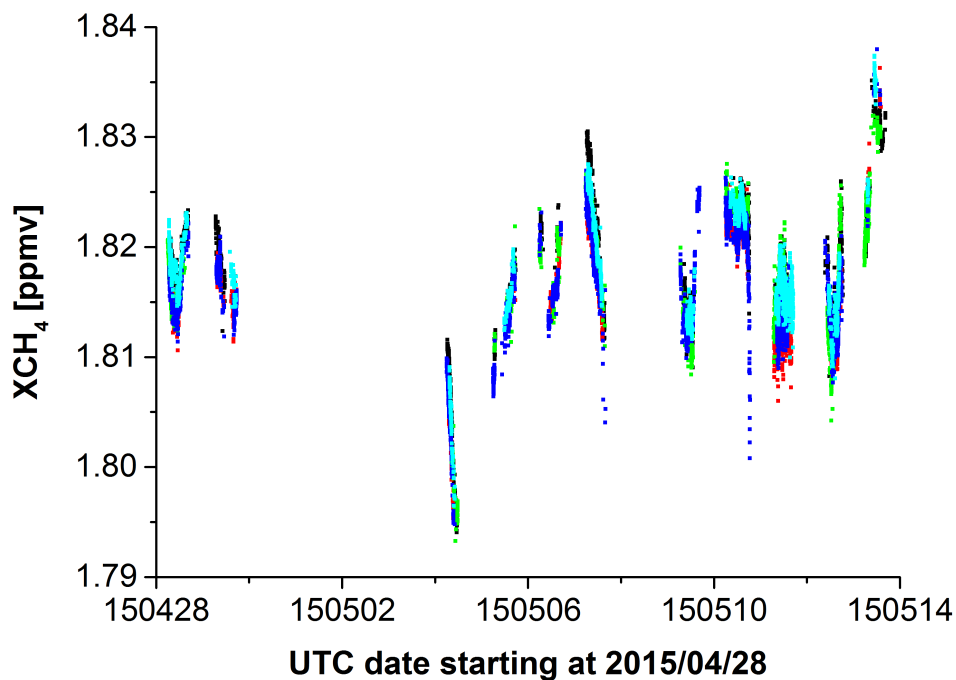


Figure 7.5: Time series of observed XCH_4 for the Berlin campaign from 26 June 2014 to 11 July 2014. The colours denote the different measurement sites.

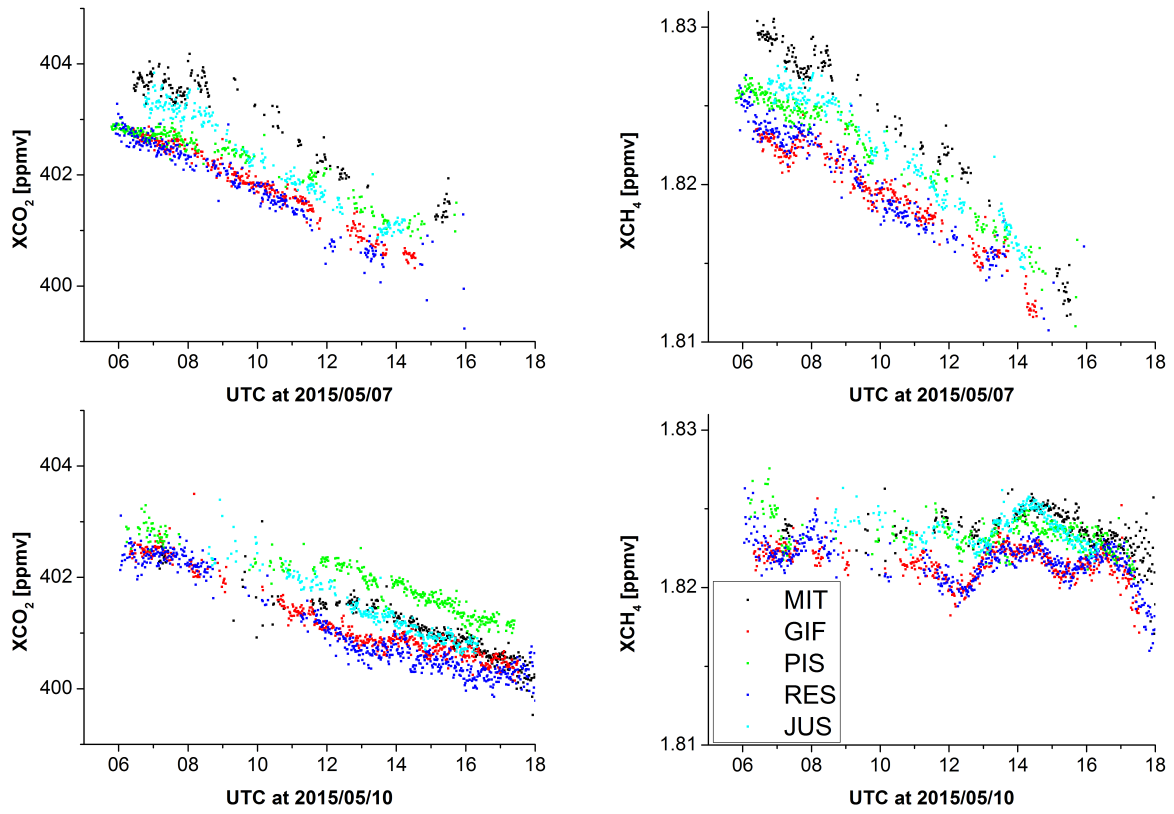


Figure 7.6: XCO₂ and XCH₄ measurements for 07 May and 10 May 2015. For 07 May both XCO₂ and XCH₄ record enhanced values at the Mitry Mory station compared to the other stations. For 10 May, the relative concentration differences between the sites are slightly different for XCO₂ and XCH₄.

$$E_{Gas} = \frac{U}{D} \Delta X_{Gas} V C_{dryair} = \frac{U}{D} \Delta X_{Gas} V C_{CO_2} \quad (7.1)$$

Here U is the wind speed, D is the length of the transect between downwind and upwind sites on which emissions occur and ΔX_{Gas} the gradient strength between the sites. The total column of dry air $V C_{Dryair}$ can be derived from the EM27/SUN O₂ column measurements. As an example day 07 May is chosen. On that day the surface wind speed was $U = 2 \text{ m s}^{-1}$ according to the CHIMERE model output, the transect length is $D = 20 \text{ km}$, the gradient strength $\Delta X_{CH_4} = 6 \text{ ppbv}$ and $V C_{Dryair}$ is $2.2 \cdot 10^{29} \text{ molecules m}^{-2}$. The resulting emission flux is $E_{CH_4} = 1.3 \cdot 10^{17} \text{ molecules s}^{-1} \text{ m}^{-2}$. Integrated over the Paris area ($20 \text{ km} \times 20 \text{ km}$) with the molar mass of methane ($M_{CH_4} = 16.04 \text{ g mol}^{-1}$) yields an emission strength of $E_{CH_4} (\text{kg s}^{-1}) = 1.4 \text{ kg s}^{-1}$. Assuming a $\Delta X_{CO_2} = 1.5 \text{ ppmv}$ gradient, the resulting emission strength using the molar mass of carbon dioxide ($M_{CO_2} = 44.01 \text{ g mol}^{-1}$) is $E_{CO_2} (\text{kg s}^{-1}) = 1000 \text{ kg s}^{-1}$. For CO₂ this value is quite close to the value from the IER emission inventory, $E_{CO_2} (\text{kg s}^{-1}) = 1200 \text{ kg s}^{-1}$. This exercise is of course rather qualitative and is expected to set a lower boundary for the emission strength. This is due to the fact that for this calculation surface wind speeds are used while for a more realistic analysis a mean wind speed, calculated from the different altitudes weighted with the vertical distribution of the CH₄ molecules, should be used. This mean wind speed would be faster than the surface wind speed, thereby leading to larger E_{Gas} . For a quantitative analysis, in the next section CHIMERE model results are presented.

7.4.2 Modelling results

In this section, the CHIMERE model results for XCO_2 are analysed. To correctly attribute gradients of XCO_2 , it is of utmost importance that the model accurately describes the meteorological parameters, e.g. the wind direction and wind speed. Errors for these parameters would disturb the modelled XCO_2 gradients. In Fig. 7.7 model and observational wind speed and direction for the Gif-Sur-Yvette site are depicted. Overall, the model reproduces the observational data very well, the wind speed is sometimes slightly overestimated by the model, most prominently seen on 30 April. The prediction of the wind direction is in general very good, only for sudden changes the model does not follow the observed change of wind direction to its full extent, see 04 May and 10 May.

Fig. 7.8 depicts the modelled XCO_2 time series at the different measurement sites. The general pattern is similar for all stations, as already seen by the observations. The model is not limited to solar observations and therefore delivers XCO_2 also at night time. A diurnal pattern is seen with accumulation of XCO_2 during night time and a decrease during the day due to photosynthesis. Furthermore, a synoptic pattern similar at all sites can be observed. Additionally, clear differences between the stations are visible, for example on 29 April or 10 May. Typically during this study, the northerly sites PIS and MIT as well as the JUS site in the city centre exhibit enhanced XCO_2 values with respect to the southerly sites. In the following it will be shown that these differences in the model between the stations can be mainly attributed to fossil fuel CO_2 emissions.

Fig. 7.9 shows the influence of the biosphere (blue line) and the FF CO_2 emissions (green line) on the modelled time series of XCO_2 , where the red line neglects the influence of FF CO_2 emissions and NEE, whereas the black line includes it. The left panel depicts the conditions for the RES site, which was upwind of Paris during most of the campaign. For this site, the pattern of the modelled XCO_2 is dominated by the NEE, the correlation between the black and green curve is apparent. The influence of FF CO_2 emissions is negligible most of the time. For the PIS site, downwind of Paris during considerable parts of the campaign, the influence of FF CO_2 emissions is important. The enhancements due to FF CO_2 emissions of up to 2 ppmv in the green curve are also found in the XCO_2 time series, although sometimes the uptake of CO_2 from plants negates the FF CO_2 emissions (08, 09 and 11 May). It is interesting to note that the effect of the biosphere is very similar for the different sites, the correlation between the blue lines in the left and right panel is apparent. Therefore, it is expected that this effect mostly cancels out when looking at the gradients between the stations.

The XCO_2 gradients of the different sites with respect to RES are depicted in Fig. 7.10. RES is chosen as the comparison site as it was upwind of the Paris emission source during most of the campaign. The upper panel shows the total gradients taking into account the different possible causes, namely the fossil fuel emissions, the net ecosystem exchange and the boundary conditions. For the investigation of the isolated influence of the FF, the middle panel focusses on this effect. The bottom panel illustrates the influence of the NEE. Focussing first on the total resulting gradient, it can be seen that MIT, PIS and JUS show enhanced XCO_2 values with respect to RES throughout most of the campaign when southerly and southwesterly winds prevail, whereas GIF and RES values are mainly alike. Looking at the middle panel, it is apparent that the XCO_2 gradients are driven by FF CO_2 emissions. The JUS-RES gradient (blue line), for example, is strikingly similar in the upper and middle panel. The same holds true for the gradients of the other sites. Although the effect of NEE often cancels out in the gradient representation, there are times when the gradient strength due to NEE is up to 1 ppmv.

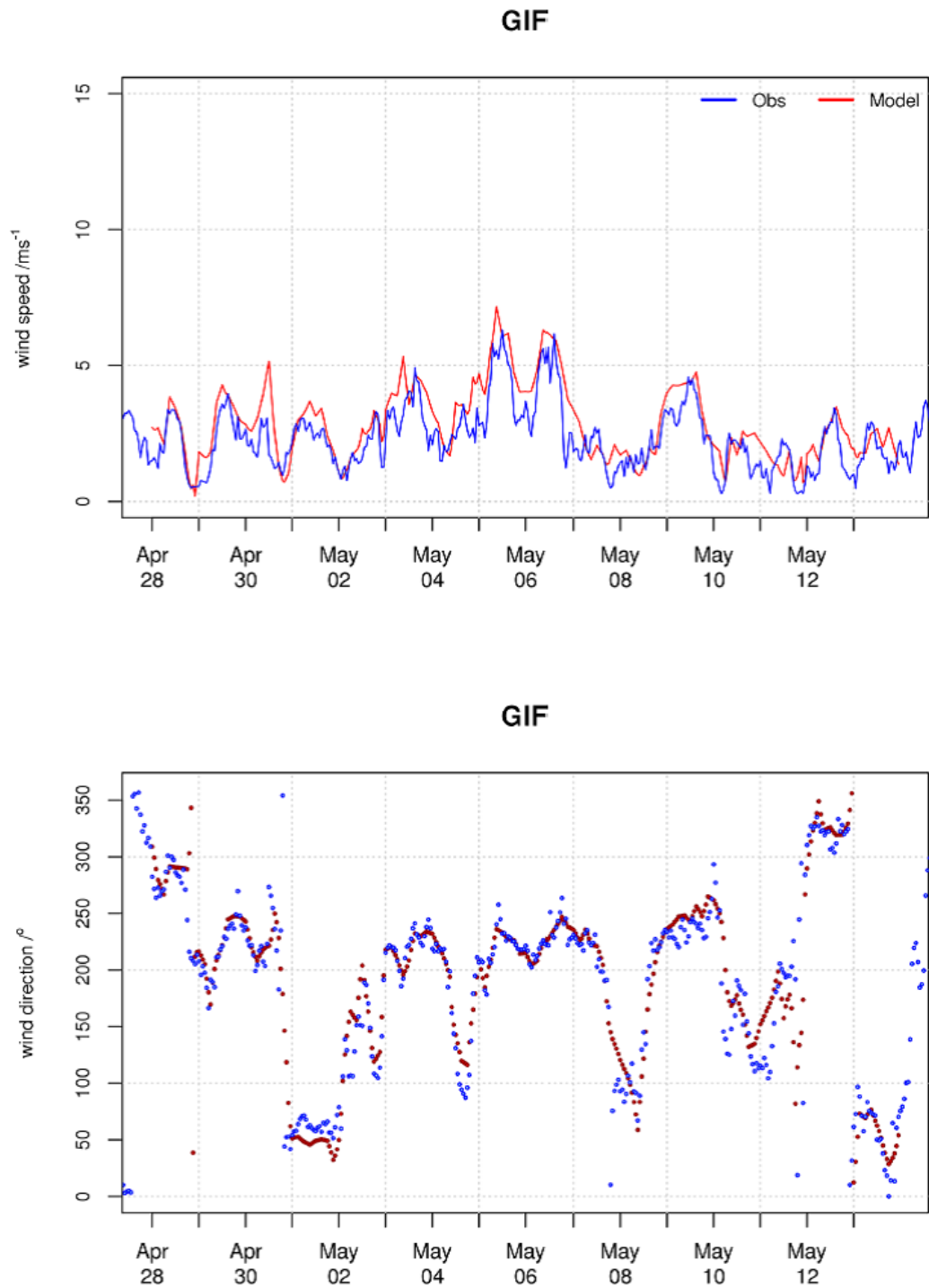


Figure 7.7: Comparison of observed and modelled wind speed and wind direction at the Gif-Sur-Yvette site. Figure taken from Vogel et al. (2018).

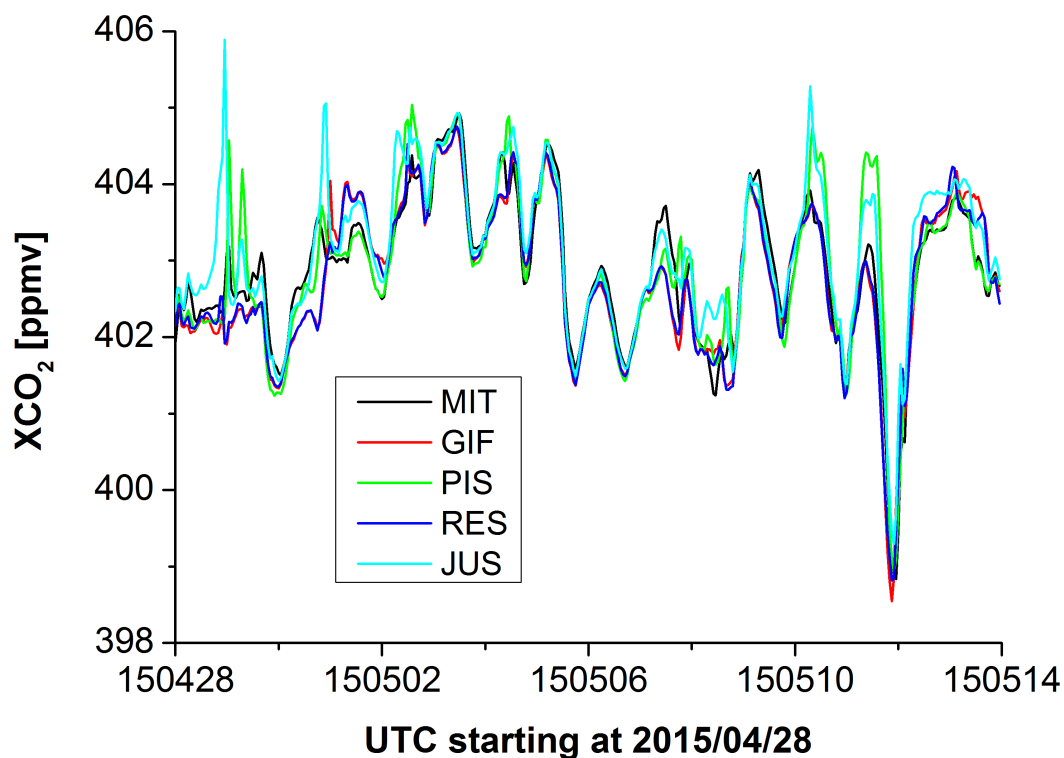


Figure 7.8: Time series of modelled XCO_2 for the Paris campaign from 28 April 2015 to 13 May 2015. The colours denote the different measurement sites. Figure adopted from Vogel et al. (2018).

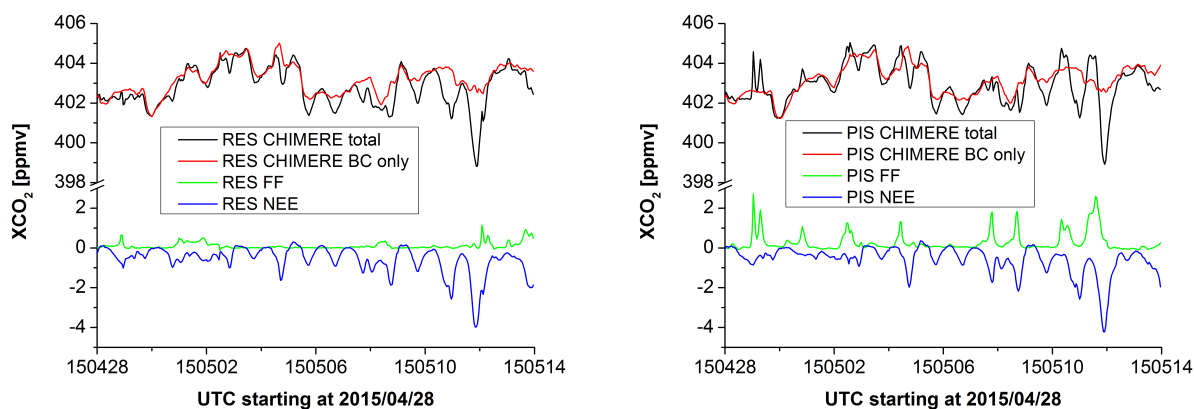


Figure 7.9: Time series of the total modelled XCO_2 (black line) and modelled XCO_2 neglecting the influence of the fossil fuel CO_2 emissions (green line) and net ecosystem exchange (blue line), resulting in the red line. The left panel shows the conditions for RES, typically a background site during the campaign, the right panel depicts the situation for PIS, which was downwind of Paris during large parts of the campaign.

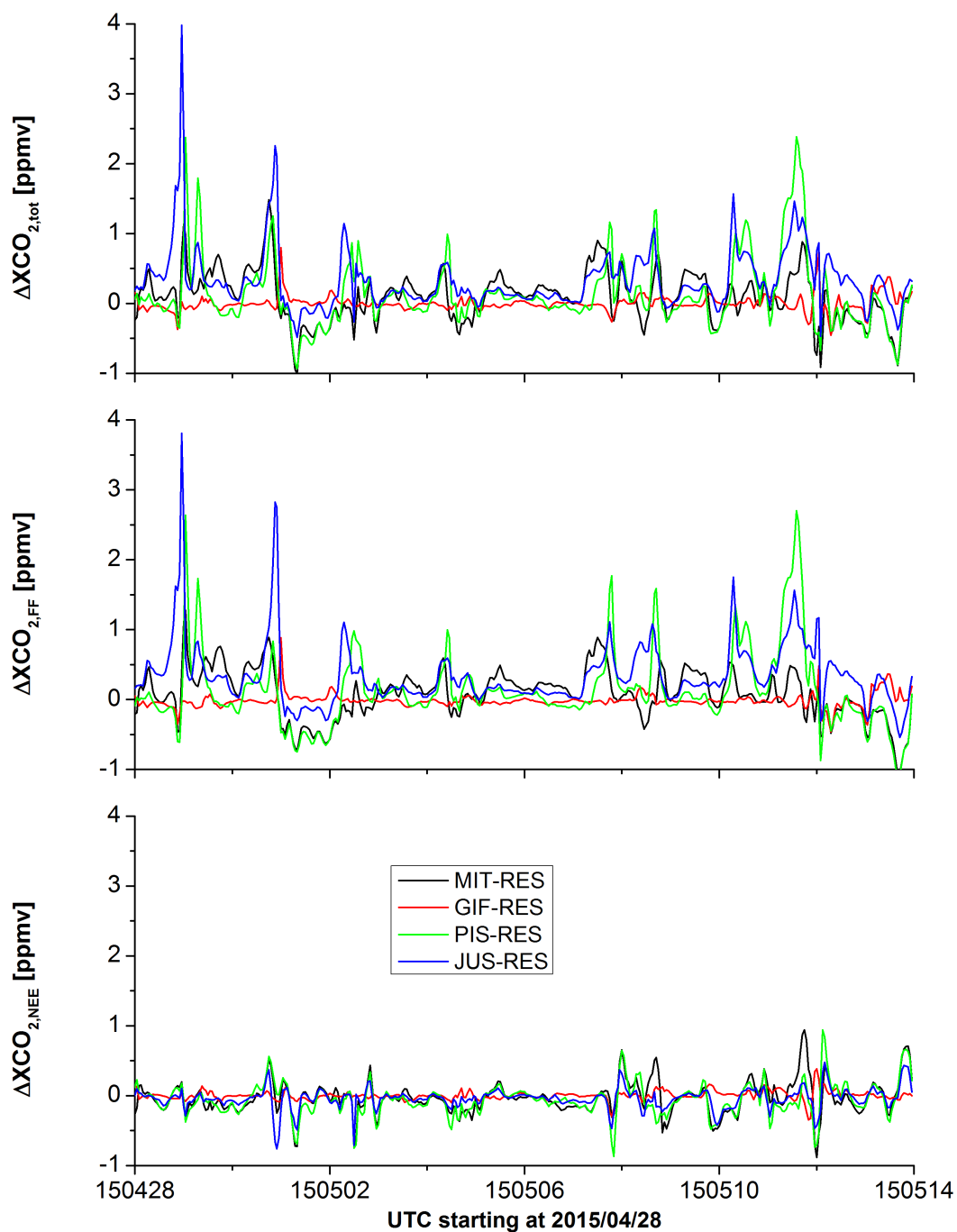


Figure 7.10: ΔXCO_2 gradients of the different measurement sites with respect to RES, which served as a background site during most of the Paris campaign. The top panel shows the total ΔXCO_2 gradient, taking into account FF and NEE. The middle panel separately depicts the gradients only due to FF. In the bottom panel ΔXCO_2 gradients resulting from the influence of NEE are shown. Figure adopted from Vogel et al. (2018).

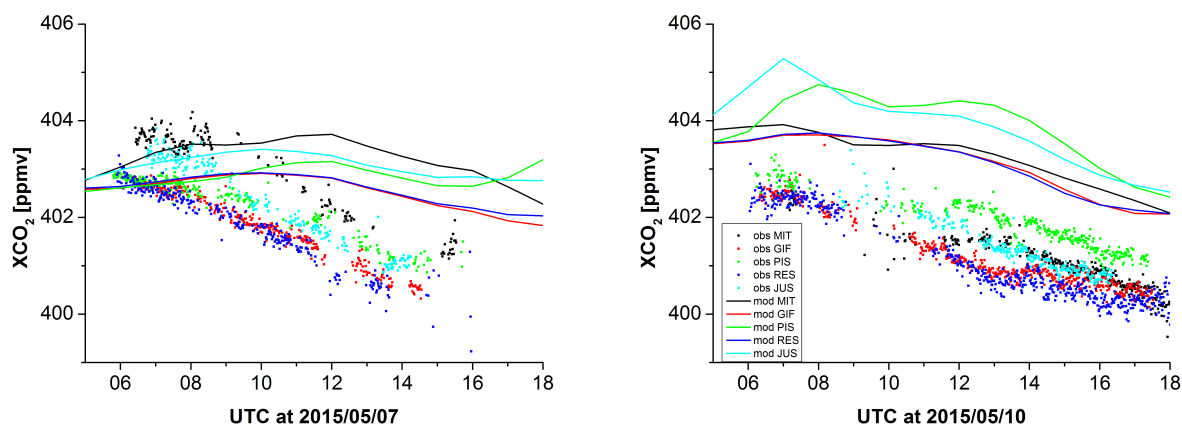


Figure 7.11: Observed and modelled XCO_2 time series for 07 May and 10 May.

7.4.3 Comparison of observational and model data sets

In Fig. 7.11 the observed and modelled XCO_2 time series for 07 May and 10 May are depicted. These two days are selected exemplary, they are representative for the whole campaign period. The model results are biased high with respect to the EM27/SUN observations. As the absolute calibration of the EM27/SUN with respect to the WMO scale is expected to be well within 0.5 ppmv, see chapter 5, this is a clear indication that the model overestimates the background CO_2 concentrations. Apart from this bias, the agreement of the intraday variability of measured and observed XCO_2 is of acceptable quality, for 07 May the reduction of CO_2 due to photosynthesis is underestimated in the model. The relative concentrations between the sites are captured very well in the model, e.g. for 07 May MIT shows the highest XCO_2 both in the model and observations. Furthermore, the concentration of JUS with respect to MIT and PIS is in excellent agreement. The background sites show the lowest XCO_2 values in both data sets. The relative differences between the sites seen in the observations are also reproduced well for 10 May. For this day, also the general daytime variability is in good agreement between model and observations.

The relative XCO_2 concentrations between model and observations were found to be in good agreement. For a detailed analysis the observed and modelled gradients between the typical downwind sites PIS and MIT with respect to the typical background station RES are presented in Fig. 7.12, the observed values were binned into hourly mean values. The error bars denote standard deviations of the averaged hourly data. To allow for a better assessment of the data, the values are colour coded with the wind direction at the time of measurement. Focussing first on the gradient between PIS and RES in the left panel (representative for the western part of Paris), a good agreement between observations and model is found with a slope of 0.97 ± 0.08 and a Pearson's correlation coefficient of $R = 0.82$. Negative gradients depict situations where the wind direction is deviating from the predominant southerly direction and thereby RES is not a background site. The XCO_2 gradient between MIT and RES in the right panel of Fig. 7.12 is representative for the eastern part of Paris. Here the observed XCO_2 gradients are significantly higher compared to the modelled gradients with a slope of 1.71 ± 0.11 and $R = 0.88$. This hints at a strong underestimation of CO_2 emissions in the underlying IER emission inventory in the eastern suburbs of Paris. This finding is also true for northerly winds with negative XCO_2 gradients. Another explanation for lower modelled XCO_2 gradients is overestimated horizontal dispersion in the model. However, this should also affect the gradient between PIS and RES, therefore this cause seems unlikely. In Fig. 7.13 the gradients from the downwind sites with

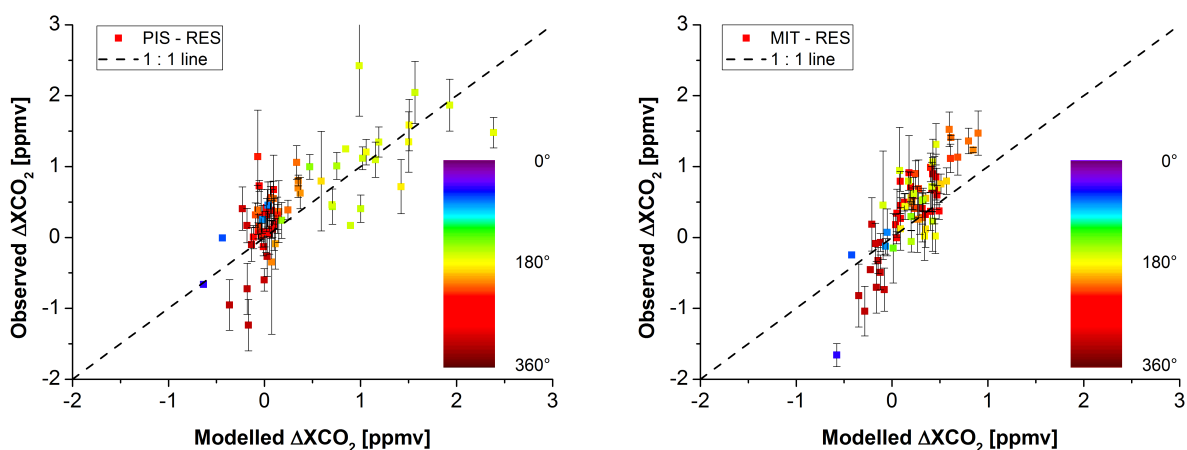


Figure 7.12: Comparison of hourly averaged modelled and observed gradients ΔXCO_2 between PIS and RES (left panel) as well as MIT and RES (right panel). The error bars are standard deviations of the observational data.

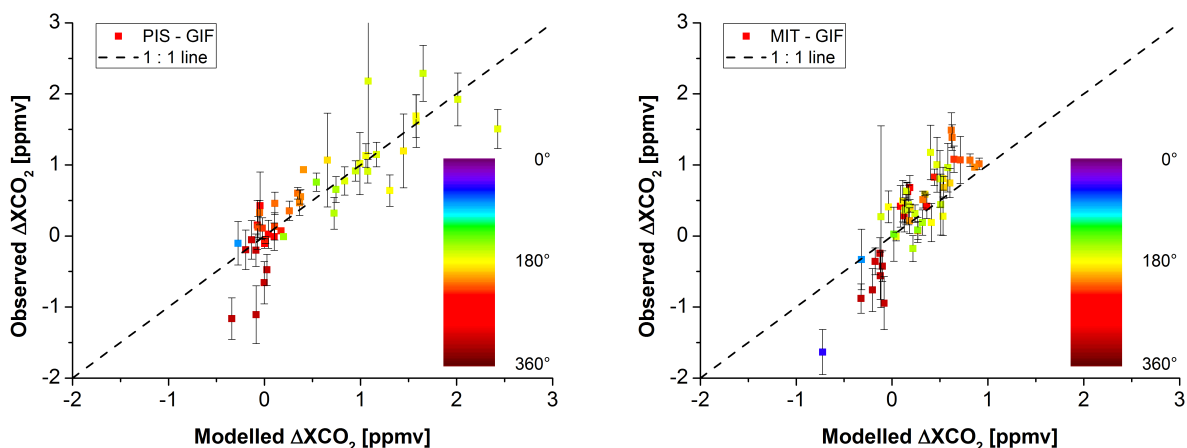


Figure 7.13: Comparison of hourly averaged modelled and observed gradients ΔXCO_2 between PIS and GIF (left panel) as well as MIT and GIF (right panel). The error bars are standard deviations of the observational data.

respect to the other downwind station GIF is shown. The observed and modelled gradient between PIS and GIF in the left panel agree well with a slope of 0.98 ± 0.07 and $R = 0.90$. As for the other background site RES, the gradient representative for the eastern part of Paris, MIT - GIF, differs between model and observation with a slope of 1.54 ± 0.11 and $R = 0.89$. This is a further indication that the IER emission inventory underestimates the CO_2 emissions in the eastern outskirts of Paris.

7.5 Conclusions

In this chapter, a campaign performed in April and May 2015 with an ensemble of EM27/SUN spectrometers has been analysed. Calibration factors of O_2 , XCO_2 and XCH_4 found for the Paris campaign agree with the factors found for the Berlin campaign (June and July 2014) within the measured noise level. After the Berlin test campaign, this is the first measurement of this kind in a megacity. Despite unfavourable meteorological conditions due to clouds and hazy conditions (in total there were only 6 good measurement days), over 10000 spectra were recorded.

XCO₂ gradients in the order of 1.0 - 1.5 ppmv were found between upwind and downwind sites from EM27/SUN measurements. Opposed to the Berlin campaign, for Paris XCH₄ gradients were detected unambiguously. A simple differential column model yields an emission strength of $E_{CO_2} = 1000 \text{ kg s}^{-1}$ and $E_{CH_4} = 1.4 \text{ kg s}^{-1}$. For CO₂ this emission strength is close to the value from the IER emission inventory, $E_{CO_2} = 1200 \text{ kg s}^{-1}$.

For a quantitative analysis the XCO₂ measurement results are compared to the CHIMERE high resolution chemistry transport model utilising the IER emission inventory. For CHIMERE it is found that fossil fuel CO₂ emissions are the dominant effect for XCO₂ gradients between the sites in the order of 1.0 - 1.5 ppmv. The influence of the biosphere is not negligible, even for the XCO₂ gradients, although the impact is greatly reduced compared to the XCO₂ values themselves. Comparing model and observations, it is found that the model overestimates the background XCO₂ concentration by about 2 ppmv. The shape and especially the relative concentrations between the sites are nicely reproduced by the model with respect to the observations. A comparison of the observed and modelled XCO₂ gradients with RES as the background station shows that for the western part (PIS is the downwind site) of Paris the agreement is good with a slope of 0.97 ± 0.08 and $R = 0.82$, while for the eastern part (downwind site MIT) the model underestimates the gradient strength (slope = 1.71 ± 0.11 and $R = 0.88$). This finding also holds true for the GIF background site, where for the PIS - GIF gradient a slope of 0.98 ± 0.07 and $R = 0.90$ and for the MIT - GIF gradient a slope of 1.54 ± 0.11 and $R = 0.89$ is found. The reason for this difference is probably an underestimation of eastern Paris emissions in the underlying IER emission inventory. Another possible explanation for this effect, overly horizontal dispersion of CO₂ in the model, seems unlikely as it would affect also the western gradients. The correlation coefficients found are impressive as even for optimised fluxes from the inversion of surface observations only $R = 0.91$ is achieved (Bréon et al., 2015). Therefore, this campaign shows the additional benefit of using total column measurements for the verification of emission inventories.

Due to the short duration of the campaign in conjunction with the unfavourable weather conditions, a robust interpretation of the daytime changes of XCO₂ gradients is not possible. Nevertheless, the capacity of the EM27/SUN to independently assess emission inventories is demonstrated. It is shown that total column measurements offer additional benefits for model evaluations compared to in situ measurements, because they are insensitive to the details of the vertical mixing and very local, unrepresentative sources.

Permanent installations of EM27/SUN surrounding cities are desirable for a further quantitative analysis of Paris CO₂ and CH₄ emissions. This is now possible due to the development of an automated shelter (Heinle and Chen, 2018), which enables measurements without the need for a human operator. In the future, a possible inversion scheme for the optimisation of fluxes based on total column measurements, already existing for in situ observations (Staufner et al., 2016), will further help to constrain emission inventories from cities, or other sinks and sources, and thereby help to construct highly accurate emission inventories.

Chapter 8

Tokyo campaign

In chapter 6 and chapter 7 measurement campaigns were presented and compared to model simulations. For this campaign, conducted in Tokyo 2016, additional possible applications of the EM27/SUN are shown. The EM27/SUN is used as a verification instrument for satellite measurements. In addition, the TCCON instruments in Karlsruhe and Tsukuba are compared, using the EM27/SUN as a transfer standard.

8.1 Campaign design

The Tokyo campaign took place in the periphery of Tokyo from 16 February to 06 April 2016. Two EM27/SUN spectrometers were deployed, one belonging to KIT (SN 38), the other one (SN 44) to the Japanese Aerospace Agency (JAXA). Both sites were equipped with weather stations recording among others wind speed and wind direction. At the beginning of March, an additional EM27/SUN (SN 63) from the National Institute of Environmental Studies (NIES), calibrated at KIT before shipping, arrived in Tsukuba. Before (03 February to 10 February) and after (11 April to 20 April) the campaign calibration measurements were performed in Tsukuba together with a co-located TCCON instrument. Additionally, before and after being shipped to Japan, the KIT EM27/SUN was compared to the Karlsruhe TCCON instrument. Thereby, the possibility of the EM27/SUN to act as a transfer standard between TCCON sites is investigated.

Compared to the prior campaign locations Berlin and Paris, the city of Tokyo poses some additional challenges. (1) The definition of the Tokyo city area is complicated due to the large and non-uniform spatial extent. (2) Tokyo is located at the seaside, the wind fields are therefore expected to show small scale variations, exacerbating interpretation of the measurements. (3) On the northern and western borders the city is surrounded by mountains up to 1800 m elevation. This leads to funneling of wind on the ground level. At higher altitudes the wind is not funneled, leading to wind shear between the different altitudes and thereby complicating the analysis of the measurement data. (4) Around the Tokyo bay several power plants and refineries are located, therefore XCO_2 and XCH_4 gradients between the sites are a superposition of the Tokyo city emissions and the power plants and refineries emissions.

Figure 8.1 shows a map with the measurement stations (red stars). Yellow stars denote the position of power plants. The GOSAT satellite also routinely takes measurements over Tokyo (yellow circles). From the map, the difficult topography is clearly visible. Directly south of Tokyo the Tokyo Bay and the Pacific ocean are situated, west and north of Tokyo mountains up to 1800 m are located.

The KIT EM27/SUN was located at Saitama University, northwest of the Tokyo city centre.



Figure 8.1: Map showing the measurement stations around Tokyo (red stars). Map source: <http://www.maps.google.de/>.

The JAXA EM27/SUN was operated at the Sodegaura city hall on the other side of the Tokyo bay. Starting from 03 March, the NIES instrument was stationed in Tsukuba. Coordinates and altitude of the different stations are given in Table 8.1.

8.2 Calibration measurements

8.2.1 ILS measurements

First the ILS measurements performed before and after the Tokyo campaign are presented, see Table 8.2. In addition to the measurements performed in Tsukuba directly before and after the campaign on 12 February and 13 April, ILS measurements were performed in Karlsruhe before and after shipping of the KIT EM27/SUN. On 19 January the NIES instrument was calibrated at KIT and ILS measurements were carried out. Focussing first on the KIT instrument, the

Location	ID	Latitude ($^{\circ}$ N)	Longitude ($^{\circ}$ E)	Altitude (m)
Tsukuba	TSU	36.051	140.121	43
Saitama	SAI	35.864	139.609	31
Sodegaura	SOD	35.430	139.954	13

Table 8.1: Locations and altitudes of the measurement sites during the Tokyo field campaign. Coordinates were derived from GPS sensors. The altitudes were derived from topographic data (<https://www.sonnenverlauf.de>).

Instrument	19 Jan.	12 Feb.	13 Apr.	09 Sep.
KIT	0.9803	0.9808	0.9811	0.9811
JAXA		0.9382	0.9377	
NIES	0.9853		0.9855	

Table 8.2: Compilation of ILS modulation efficiencies measured at maximum OPD = 1.8 cm. Measurements were performed in Karlsruhe in January and September 2016 as well as in Tsukuba February and April 2016.

ME at MOPD is very stable, the shipping to and from Japan did not affect the instrumental characteristics. Also for the JAXA EM27/SUN the ILS is stable before and after the Tokyo campaign. The absolute value of the modulation efficiency is however very low (≈ 0.9380), by far the lowest value ever observed for any EM27/SUN. This instrument was not checked at KIT prior to deployment to the customer JAXA. Due to the lack of appropriate tools no attempt was undertaken in Tsukuba to optimise the ILS. This instrument was upgraded in 2017 at Bruker Optics and then sent to KIT for calibration measurements. At this time the instrumental line shape was optimised and drastically improved (ME at MOPD: 0.9714) (Frey et al., 2018). As for the KIT instrument, the ILS of the NIES EM27/SUN is unchanged before and after shipping of the spectrometer.

8.2.2 Comparison measurements in Tsukuba

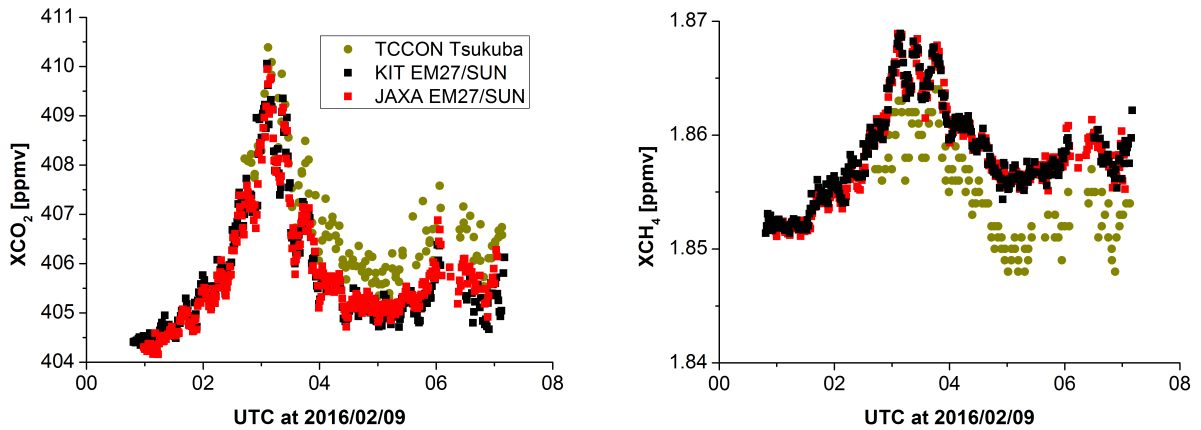


Figure 8.2: Calibrated XCO₂ and XCH₄ values for the JAXA and KIT EM27/SUN spectrometers on 09 February before the Tokyo campaign. Golden dots show data from a co-located TCCON instrument. To scale the KIT EM27/SUN to the TCCON Tsukuba the universal calibration factors derived in chapter 5 from a comparison between the reference EM27/SUN and the TCCON Karlsruhe are applied.

Before and after the Tokyo campaign comparison measurements between the KIT, NIES (only after the campaign) and JAXA EM27/SUN together with a co-located TCCON instrument were performed in Tsukuba from 03 February to 10 February and from 11 April to 20 April. Fig. 8.2 depicts calibration measurements on 09 February. The JAXA EM27/SUN is scaled to the KIT EM27/SUN, the calibration factors are given in Table 8.3. The EM27/SUN spectrometers are not explicitly scaled to the TCCON Tsukuba, rather the calibration factors derived in chapter 5 from a comparison between the reference EM27/SUN and the TCCON Karlsruhe are applied. Because the calibration factors show a seasonal variability, it is not surprising that the absolute

Instr.	XCO ₂ before Tokyo	XCO ₂ after Tokyo	XCO ₂ all Tokyo
JAXA	0.9942 (0.08)	0.9944 (0.07)	0.9943 (0.08)
NIES		1.0014 (0.06)	1.0014 (0.06)
Instr.	XCH ₄ before Tokyo	XCH ₄ after Tokyo	XCH ₄ all Tokyo
JAXA	0.9977 (0.08)	0.9973 (0.04)	0.9975 (0.07)
NIES		1.0008 (0.06)	1.0008 (0.06)

Table 8.3: XCO₂ and XCH₄ calibration factors for the JAXA and NIES EM27/SUN with respect to the KIT instrument. Measurements were performed in Tsukuba February and April 2016, in between the spectrometers were transported for the Tokyo campaign measurements. Values in parentheses denote the percent 1 σ precision of the ratio.

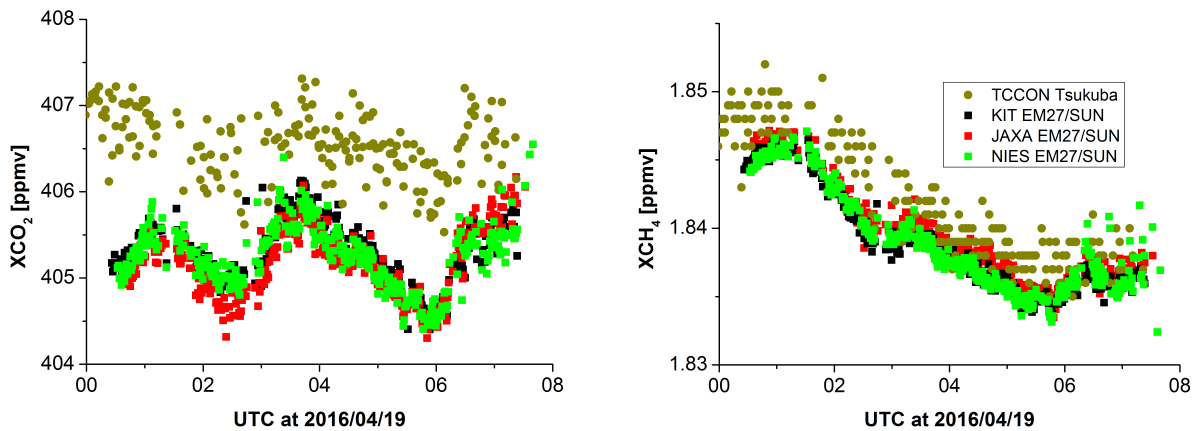


Figure 8.3: Calibrated XCO₂ and XCH₄ values for the JAXA, NIES and KIT EM27/SUN spectrometers on 19 April after the Tokyo campaign. Golden dots show data from a co-located TCCON instrument.

values do not fit perfectly. This effect is described in detail in section 5.1.5. The intraday variability of the EM27/SUN spectrometers and the TCCON Tsukuba is almost similar. On this day there is a very large enhancement both in XCO₂ (≈ 5 ppmv) and XCH₄ (≈ 15 ppbv) from 2:00 UTC to 4:30 UTC. As there is no point source of both CO₂ and CH₄ situated in close vicinity to the Tsukuba measurement site, this enhancement is probably originating from the city of Tokyo.

Fig. 8.3 shows the calibration measurements after the Tokyo campaign on 19 April. On this day there is a significant offset between the EM27/SUN and TCCON XCO₂ absolute values, whereas there is a good agreement for XCH₄. As for 09 February, the shape of EM27/SUN and TCCON measurements is similar. Although not very pronounced, for both days the XCO₂ intraday shape of the KIT and JAXA EM27/SUN is not exactly identical. This effect is also observed for the other days of the calibration measurements. Its origin is probably the highly non-ideal ILS of the JAXA EM27/SUN, which cannot be fully corrected by the ILS correction scheme.

8.2.3 The EM27/SUN as a transfer standard between TCCON stations

Up to this point the calibration measurements performed in Tsukuba serve the same purpose as the calibration measurements performed for the Berlin and Paris campaign, i.e. ensuring unbiased XCO₂ and XCH₄ values. To add additional value, comparison measurements carried

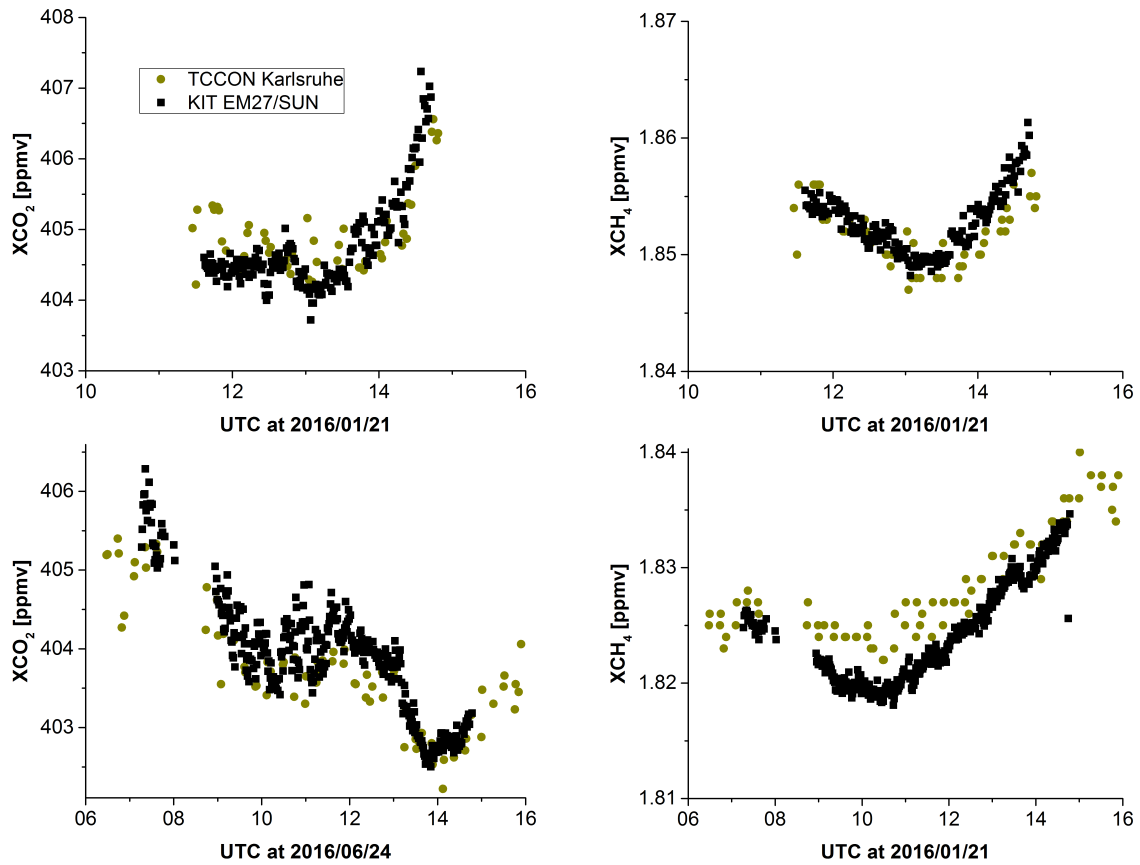


Figure 8.4: Comparison of XCO_2 and XCH_4 values between the KIT EM27/SUN and the TCCON Karlsruhe on 21 January and 24 June 2016.

out in Karlsruhe in January 2016 and 11 May as well as 23 - 24 June 2016 before and after shipping of the KIT EM27/SUN to Japan between the TCCON Karlsruhe and the KIT EM27/SUN are taken into account. The EM27/SUN acts as a transfer standard between the two TCCON instruments in Karlsruhe and Tsukuba. This technique can also be applied for the calibration of TCCON spectrometers where the common TCCON calibration routine, namely aircraft overflights, is not possible.

Fig. 8.4 shows XCO_2 and XCH_4 values of the KIT EM27/SUN and the TCCON Karlsruhe on 21 January and 24 June 2016. On first sight, the agreement between KIT EM27/SUN and the TCCON Karlsruhe is better than the agreement between KIT EM27/SUN and the TCCON Tsukuba. For a quantitative analysis, the calibration factors for XCO_2 and XCH_4 are calculated and given in Table 8.4. KIT EM27/SUN and the TCCON Karlsruhe show an excellent agreement, well within the 1σ precision of the ratio. Opposed to this, there are significant differences between KIT EM27/SUN and the TCCON Tsukuba for XCO_2 , see Figs. 8.2 and 8.3.

For a robust analysis, as performed in chapter 5, the next step is to truncate the TCCON Tsukuba raw interferograms in order to eliminate the uncertainty caused by the different sensitivity of the instruments. It is planned to perform this study in the future. Here, it can only be concluded that differences between the two TCCON instruments are observed for XCO_2 . The origin of this difference, problems in the instrumental alignment of one TCCON instrument or uncertainties caused by the different sensitivity between EM27/SUN and TCCON retrieval, cannot precisely be determined at this point.

Instr.	Dates	No. co.	XCO ₂ factor	XCH ₄ factor
TCCON Karlsruhe	160114 - 160121, 160511 - 160624	276	0.9999 (0.13)	1.0001 (0.25)
TCCON Tsukuba	160203 - 160210, 160411 - 160420	1256	0.9973 (0.19)	1.0010 (0.26)

Table 8.4: XCO₂ and XCH₄ calibration factors between the KIT EM27/SUN and the TCCON Karlsruhe and TCCON Tsukuba. respectively. Values in parentheses denote the percent 1 σ precision of the ratio.

8.3 Campaign results

The duration of the Tokyo campaign (16 February to 06 April) is longer with respect to the prior campaigns discussed in this thesis. Given the difficulties concerning the topography and many different sources in the Tokyo area together with the fact that during most of the campaign only two EM27/SUN are deployed, therefore restricting the successful application of the gradient approach to only one wind direction, a long campaign is helpful to obtain a sufficient number of measurements.

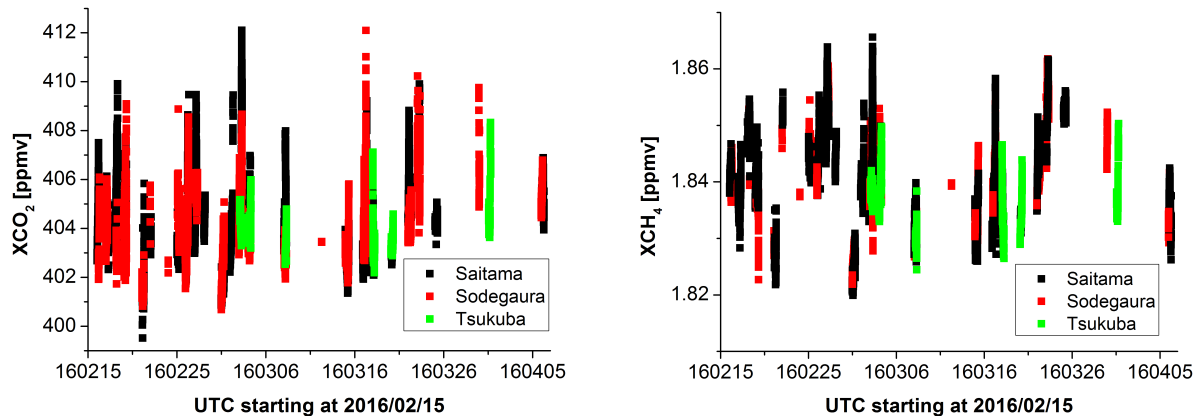


Figure 8.5: Evolution of XCO₂ (left panel) and XCH₄ (right panel) during the campaign at the Saitama, Sodegaura and Tsukuba site.

Fig. 8.5 shows the XCO₂ and XCH₄ time series as observed by the EM27/SUN in Saitama University (black squares), Sodegaura (red squares) and Tsukuba (green squares). The instrument in Tsukuba did not arrive until the beginning of March and serves as a background site. XCO₂ values range from 400 ppmv to 412 ppmv, with intraday changes of up to 9 ppmv. For XCH₄ values from 1820 ppbv up to 1865 ppbv are observed with intraday variations reaching 30 ppbv.

Before presenting one day of the Tokyo campaign in more detail, first the general challenges of this campaign are discussed by the example of 19 February, see upper panel of Fig. 8.6. On this day the wind speed was very low throughout the day, with surface wind speeds mostly below 1 m s⁻¹. Trying to disentangle the different contributions to the XCO₂ signal, an underlying gradient of ≈ 2 ppmv is identified, with Saitama showing enhanced values. Superimposed to this gradient are other signals. From 02:00 UTC to 04:00 UTC an additional enhancement is seen at Saitama. This signal is also seen amplified from 03:00 UTC to 05:00 UTC at Sodegaura. Only at Sodegaura another short, sharp increase of XCO₂ in the order of ≈ 6 ppmv is detected at 06:00 UTC. Between 05:00 UTC and 06:00 UTC, the surface wind direction at Sodegaura

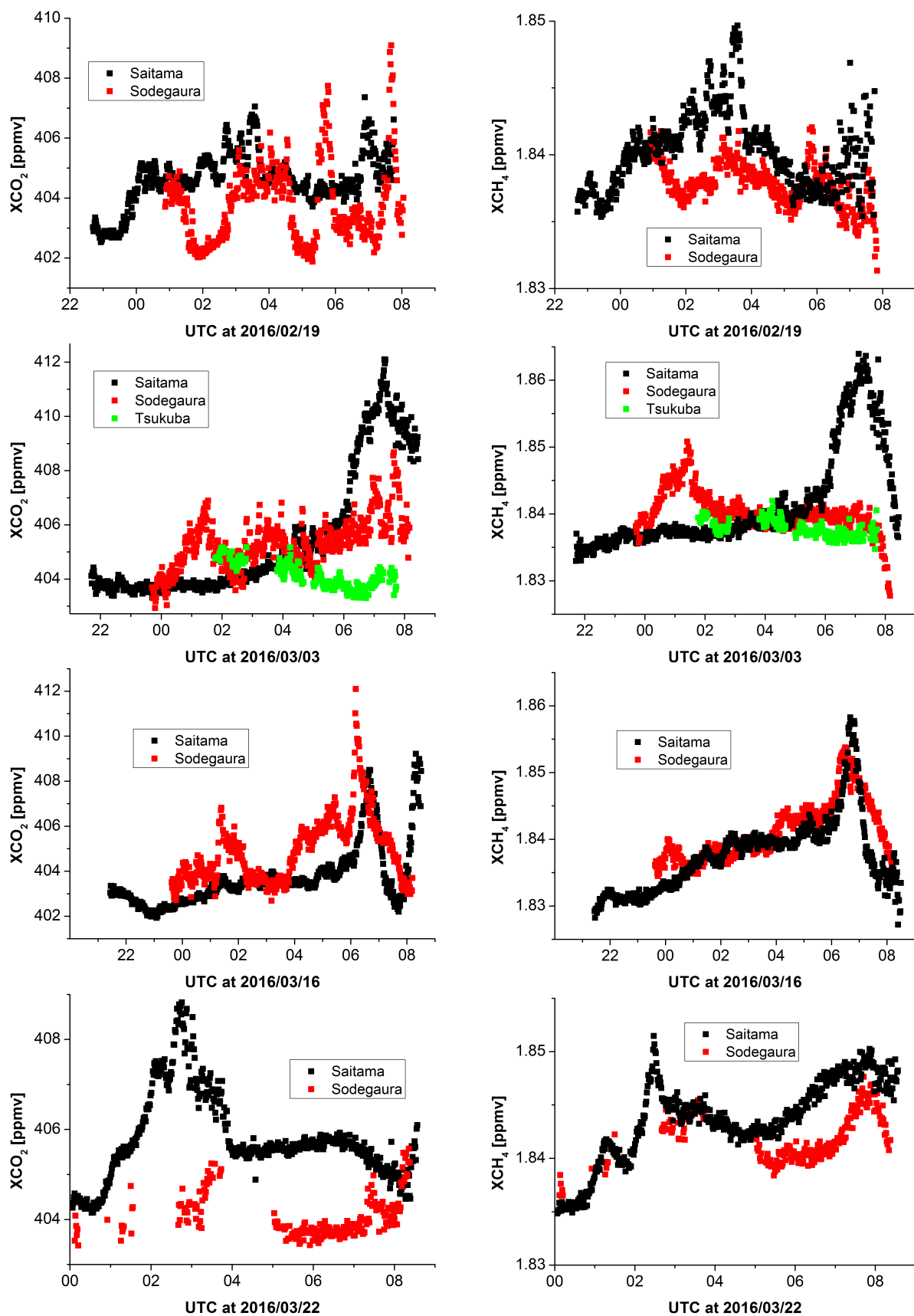


Figure 8.6: XCO₂ and XCH₄ values for several days of the Tokyo campaign.

changed from easterly to westerly winds. The observed signal at that time is probably caused by the exhaust plume of a nearby power plant, see Fig. 8.1. Later, there is another signal seen at Saitama and later enhanced at Sodegaura near the end of the measurement day. For XCH_4 the general pattern is quite similar, although there are noticeable differences. Whereas a stable underlying gradient can be identified for XCO_2 , for XCH_4 this underlying gradient of ≈ 5 ppbv disappears at around 05:00 UTC. Moreover, the last XCO_2 peak seen in Saitama and Sodegaura cannot clearly be identified for XCH_4 . The XCO_2 and XCH_4 pattern for this day are especially complicated, but also for other days gradients from the Tokyo city source are often superimposed by other signals. Furthermore, on some days like 03 March, the wind direction changed, reversing the upwind and downwind station, see second panel of Fig. 8.6. For the higher altitudes, the prevailing wind direction are westerly winds. Some XCO_2 and XCH_4 enhancements seen for both sites, see e.g. 16 March between 06:00 UTC and 07:00 UTC, are therefore probably originating from western Japan or the east coast of China (Isamu Morino, priv. comm.).

8.4 Comparison of EM27/SUN and OCO-2 data

On 01 March 2016 the OCO-2 satellite overpassed the Tokyo area. Coincident measurements were performed at Saitama and Sodegaura on this day, see Fig. 8.7. The dotted line denotes the time of the OCO-2 overpass. The prevailing wind direction was northwesterly, with a surface wind speed of approximately 5 m s^{-1} throughout the entire day. In agreement with the wind direction, the Sodegaura site observes enhanced XCO_2 and XCH_4 values with respect to the Saitama site. For XCO_2 , an additional enhancement of ≈ 1.5 ppmv is seen at Sodegaura at 05:30 UTC, without any corresponding XCH_4 enhancement. The XCO_2 enhancement increases in the morning until it reaches a value of 1.5 ppmv at 03:00 UTC, whereas there is a constant enhancement in XCH_4 of about 4 ppbv from 00:00 UTC to 06:00 UTC.

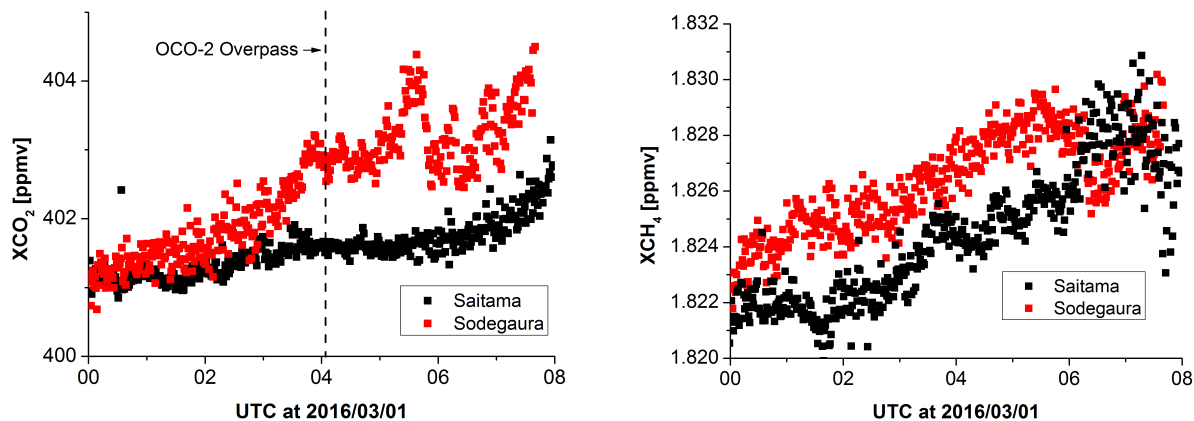


Figure 8.7: XCO_2 (left panel) and XCH_4 (right panel) measurement values on 01 March 2016. Sodegaura (red squares) shows enhanced values with respect to Saitama (black squares), in accord with the predominant wind direction on that day (NW). The dotted line denotes the time of a coincident OCO-2 overpass.

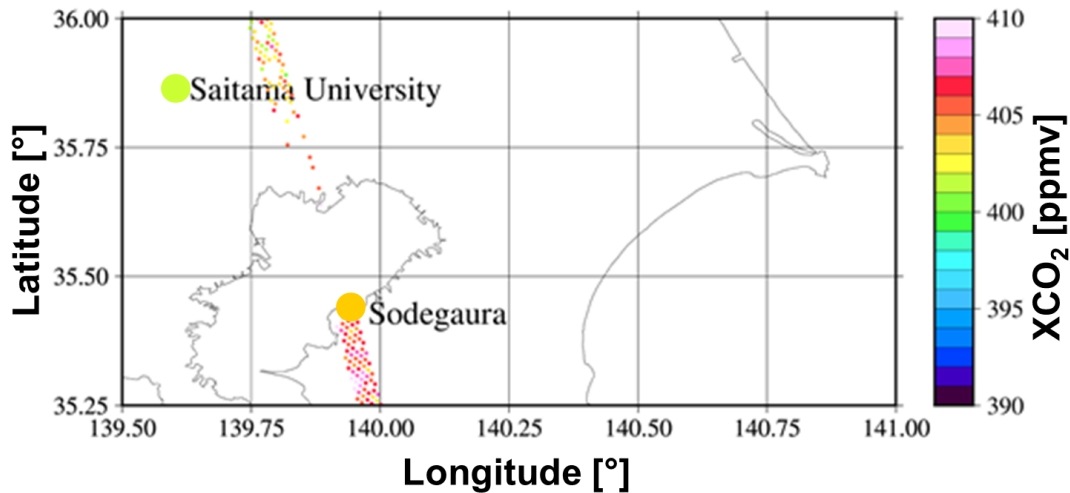


Figure 8.8: Comparison of EM27/SUN X_{CO_2} values at Saitama and Sodegaura with coincident X_{CO_2} measurements from the OCO-2 satellite on 01 March.

In Fig. 8.8, the flight path of the OCO-2 overpass is shown, together with the EM27/SUN measurement sites Saitama and Sodegaura. Colour coded are the X_{CO_2} values at 04:15 UTC, the time of the overpass. The Sodegaura site is directly in the flight path of OCO-2, the Saitama site is 10 km apart from the flight path. Because the Tokyo metropolitan area is very heterogeneous, see Fig. 8.1, this distance of 10 km might bias the gradients seen by the EM27/SUN and the OCO-2 satellite. This would be the case if the Saitama site is not really a background site but still detects emissions from areas northwest of Saitama, whereas the area OCO-2 overpasses acts as a real background site, or vice versa.

For Saitama, the EM27/SUN detects X_{CO_2} values of 401.5 ppmv at the time of the overpass, for the area closest to Saitama, OCO-2 observes 403 - 404 ppmv. For Sodegaura, the EM27/SUN records X_{CO_2} values of 403 ppmv, for OCO-2 406 ppmv is detected. Between the EM27/SUN results there is a bias, also the gradient strength differs. The EM27/SUN observes a gradient of 1.5 ppmv, whereas the gradient detected by OCO-2 is 2 - 3 ppmv.

Unfortunately, during the whole campaign of seven weeks, only this coincident measurement between OCO-2 and the EM27/SUN is recorded. This is due to the long repeat cycle of OCO-2 (16 days) and unfavourable weather conditions. Therefore, the comparison presented here remains qualitative.

With the empirical differential column formula from Eq. 7.1 introduced in section 7.4.1, the emission strength of Tokyo is qualitatively estimated here. For the length of the transect the distance $D = 30$ km between the Saitama site and the beginning of the Tokyo bay is assumed, not the distance between the two measurement sites as no uptake of X_{CO_2} or X_{CH_4} is expected over the Tokyo bay. Using a surface wind speed of $U = 5$ m s⁻¹ as recorded by the on-site weather station, $\Delta X_{CO_2} = 1.5$ ppmv, $VC_{Dryair} = 2.2 \cdot 10^{29}$ molecules m⁻² and a Tokyo emission area of 30 km \times 30 km, a CO_2 emission strength of E_{CO_2} (kg s⁻¹) = 3600 kg s⁻¹ is predicted. For Paris, this estimate yielded E_{CO_2} (kg s⁻¹) = 1000 kg s⁻¹. This factor of 3.6 is close to the factor of 3.5 obtained when comparing the inhabitants of the Paris metropolitan area (11 million people) and the Tokyo metropolitan area (38 million people)¹. For CH_4 , an emission strength of E_{CH_4} (kg s⁻¹) = 3.5 kg s⁻¹ is estimated.

¹<https://www.un.org/en/development/desa/population/publications/>

8.5 Conclusions

In this chapter, a campaign performed from 16 February until 06 April 2016 in the Tokyo metropolitan area is presented. Before and after the campaign calibration measurements are carried out in Tsukuba with a co-located TCCON instrument. Before shipping the KIT EM27/SUN additional calibration measurements with the TCCON Karlsruhe spectrometer were performed. Using the KIT EM27/SUN as a transfer standard the TCCON Karlsruhe and the TCCON Tsukuba instrument are compared. For XCO_2 a significant difference between the two instruments is detected, whereas for XCH_4 no significant difference is observed. Two reasons for this difference are supposed, errors in the alignment of one spectrometer or uncertainties caused by the different sensitivity of the instruments. To eliminate the second possibility, in the future additional tests will be performed utilising the truncated interferograms of the TCCON Tsukuba, not available at this time.

During the campaign XCO_2 values ranging from 400 ppmv to 412 ppmv and XCH_4 values from 1820 ppbv up to 1865 ppbv are detected. The intraday variability of XCO_2 reaches up to 9 ppmv, for XCH_4 intraday changes of up to 30 ppbv are observed. These variations are much higher compared to the variations observed during the previously presented campaigns in Berlin and Paris. With a simple differential column model the CO_2 emission strength of the Tokyo metropolitan area is estimated to E_{CO_2} ($kg\ s^{-1}$) = 3600 $kg\ s^{-1}$. The ratio of 3.6 between the Tokyo and Paris emission strength is in good agreement with the ratio of 3.5 obtained when comparing the number of inhabitants from both cities.

On 01 March, in addition to the EM27/SUN measurements, the OCO-2 satellite overpassed the Tokyo area. It is found that the satellite observes higher gradients (2 - 3 ppmv) compared to the EM27/SUN measurements. A possible explanation for this difference is the fact that one of the measurement sites, Saitama, is situated not directly in the flight path of OCO-2, but 10 km apart. Given the heterogeneous population distribution in the Tokyo area, this different locations might bias the gradient strength.

If in the future a permanent EM27/SUN network is planned in the Tokyo area, it is therefore recommended to put two EM27/SUN in the flight path of the OCO-2 satellite, thereby enabling permanent observations of the Tokyo emission strength as well as a direct verification method for the satellite.

Chapter 9

Summary and outlook

This thesis contributes to the precise and accurate quantification of CO₂ and CH₄ sinks and sources. In the first part of this work, a calibration procedure for a newly developed solar absorption spectrometer (EM27/SUN) is established. A central part of the calibration routine is the accurate estimation of the spectrometers instrumental line shape. This ILS of the EM27/SUN is found to be exceptionally stable over the observed time period of 3.5 years with a modulation efficiency of 0.9862 ± 0.0015 at MOPD. The established calibration routine described here is now used routinely by groups worldwide before and after conducting campaigns for the quantification of GHGs.

To assess the long term stability of the EM27/SUN, the instrument is compared to a reference spectrometer which is part of the TCCON network in a 3.5 years long time series (Frey et al., 2018). For a better comparability and to be able to distinguish instrumental drifts from resolution dependent differences, the high resolution data of the TCCON instrument are truncated to the resolution of the EM27/SUN. The instrumental stability of the EM27/SUN is found to be excellent, the yearly trend in the ratio between the instruments is -5×10^{-5} for XCO₂ (1×10^{-4} for XCH₄) and well within the 1σ precision of the ratio (1.1×10^{-3} for XCO₂, 8×10^{-4} for XCH₄, respectively). Additionally, the ensemble performance of the EM27/SUN is investigated. From 2014 to 2018, 30 instruments were optimised and tested at KIT prior to deployment. In addition, they were compared to the reference EM27/SUN as well as the co-located TCCON instrument. The ensemble mean ratio with respect to the reference EM27/SUN of the 30 tested EM27/SUN is 0.9993 (corresponding to an averaged bias of 0.20 ppmv) for XCO₂ and 0.9997 (0.8 ppbv) for XCH₄ with average standard deviations of 0.13 ppmv and 0.6 ppbv, respectively. This finding is comparable with results from Hedelius et al. (2017), where northern American TCCON sites are compared using an EM27/SUN spectrometer.

The presented ensemble study and the optimisation work contribute to the establishment and expansion of the COCCON network (Frey et al., 2018), which uses EM27/SUN spectrometers and aims to aid and complement TCCON. Due to the closeness of the EM27/SUN manufacturer, Bruker OpticsTM, to the KIT and a close collaboration between the two parties, new instruments are now routinely checked at KIT. This check includes among others correction of imperfections from non-ideal alignment, double-passing and channelling. Together with the comparison measurements this helps to achieve a high level of conformity between the instruments, essential especially for long term observations at remote sites and deployment of multiple EM27/SUN for campaign use.

In the second part of this thesis, the ability of the EM27/SUN of quantifying anthropogenic CO₂ and CH₄ emissions is investigated. In June and July 2014 a campaign with five EM27/SUN was carried out in the major city Berlin (Hase et al., 2015). This campaign constitutes the first investigation of CO₂ emissions from regional sources with EM27/SUN spectrometers worldwide.

In the mean time, this technique is quite established and used for the quantification of CO_2 and CH_4 from various sources (Butz et al., 2017; Viatte et al., 2017). Before and after the campaign, calibration measurements were carried out at KIT. The instrumental drifts between the different EM27/SUN are small (below 0.04 ppmv for XCO_2 and 0.2 ppbv for XCH_4) and well within the measured standard deviation (Frey et al., 2015). During the campaign XCO_2 gradients are observed between the stations downwind and upwind of the Berlin emission source. Due to the comprehensive calibration routine presented in the first part of this thesis, these gradients in the order of 0.5 ppmv over a background concentration of 400 ppmv can unambiguously be attributed to the emission of CO_2 from Berlin. For an estimation of the Berlin CO_2 emission source, the measured gradients are compared to a dispersion model, which divides the city of Berlin into five source regions based on the number of inhabitants. The model utilises COSMO-DE wind fields from the convective-scale regional component of the numerical weather prediction system of the German Weather Service. From this comparison an emission strength $E_{\text{CO}_2} = 800 \text{ kg s}^{-1}$ is derived. With this campaign the possibility of creating an emission inventory (in this case the five source regions) and estimating the emission strength of a regional source solely based on the EM27/SUN observations and wind fields is demonstrated.

In another campaign performed in the Paris megacity in April and May 2015, a slightly different goal is pursued. Here, an existing emission inventory (IER) is verified against the EM27/SUN measurements (Vogel et al., 2018). For this campaign, the spectrometers used also for the Berlin campaign are utilised. The instrumental drifts between the two campaigns are negligible, further showing the excellent stability of the EM27/SUN. During the campaign, despite unfavourable cloudy and rainy conditions throughout large parts of the campaign, not only XCO_2 , also XCH_4 gradients between upwind (Gif-Sur-Yvette and Saulx-les-Chartreux) and downwind (Piscop and Mitry Mory) sites are observed. This is opposed to the Berlin campaign, where no CH_4 gradients are detected. For XCO_2 , a quantitative model and observation comparison is performed. Whereas for the western part of Paris measured and modelled XCO_2 gradients agree well with a ratio not significantly deviating from 1 (Piscop - Gif-Sur-Yvette gradient ratio: 0.98 ± 0.07 , Piscop - Saulx-les-Chartreux gradient ratio: 0.97 ± 0.08), for the eastern part of the city there are significant differences (Mitry Mory - Gif-Sur-Yvette gradient ratio: 1.54 ± 0.11 , Mitry Mory - Saulx-les-Chartreux gradient ratio: 1.71 ± 0.11), with observed gradients higher than the modelled gradients. This implies that the IER emission inventory underestimates the CO_2 emission strength in the eastern suburbs of Paris. For all comparisons between measured and observed gradients an Pearson's correlation coefficient R between 0.82 and 0.90 is obtained.

This campaign shows an important field of application for the EM27/SUN. The instruments can be used for the independent assessment of emission inventories. This work therefore enables an accurate and precise quantification of sinks and sources of CO_2 and CH_4 using solar absorption spectrometers, important for the evaluation of mitigation goals set by the Paris COP21 agreement. This goal is also recognised by the European Union with the initialisation of the VERIFY project in the framework of the Horizon 2020 research and innovation program.

A third campaign carried out in the Tokyo metropolitan area between February and April 2016 with two spectrometers investigates two additional applications for the EM27/SUN. The EM27/SUN is used as a transfer standard for the intercomparison of the TCCON Karlsruhe and the TCCON Tsukuba instruments. When directly comparing the TCCON and EM27/SUN results, for XCO_2 a significant difference between the two TCCON sites is found, whereas no significant bias is observed for XCH_4 .

During the campaign on 01 March 2016 the OCO-2 satellite overpassed the Tokyo area. A direct comparison between the gradients derived from the EM27/SUN and satellite measurements encounters difficulties due to the fact that one of the EM27/SUN is not directly in the flight path of the OCO-2 satellite, but 10 km apart. Given the heterogeneous population distribution

in the Tokyo area, this different locations might bias the gradient strength. For the EM27/SUN a X_{CO_2} gradient of 1.5 ppmv is observed, while for the satellite a gradient of 2 - 3 ppmv is detected. Using the EM27/SUN gradient between the two measurement sites in conjunction with a simple differential column estimate, a CO_2 emission strength of E_{CO_2} ($kg\ s^{-1}$) = 3600 $kg\ s^{-1}$ is derived. The ratio of 3.6 between the Tokyo and Paris emission strength from this estimate is in good agreement with the ratio of 3.5 obtained when comparing the number of inhabitants from both cities.

A drawback of the campaigns is obviously the short measurement period and therefore the dependence on favourable meteorological conditions. For a robust detailed analysis a permanent deployment of EM27/SUN spectrometers is desirable. A permanent installation is facilitated by the recent development of an automated shelter (Heinle and Chen, 2018). The automated shelter is not only useful for the investigation of regional sinks and sources, but also for the deployment of the EM27/SUN at remote sites. In combination with a custom-built tracker (Klappenbach et al., 2015) it can even be permanently installed on a ship, enabling measurements over the ocean. A resulting continuous interhemispheric transect data set would be valuable to identify model deficiencies between the representation of the northern and southern hemisphere.

To fully exploit the EM27/SUN data in the future a possible inversion scheme for the optimisation of fluxes based on total column measurements will further help to constrain emissions from cities, or other sinks and sources, and thereby help to construct highly accurate emission inventories. For the analysis of the Paris campaign the CHIMERE model is used, whereas for Berlin a simple dispersion model is used. Given the in-house modelling expertise at the IMK-ASF, it is highly desirable to utilise the recently developed global ICON-ART model (Schröter et al., 2018), for which an emission module has been developed (Weimer et al., 2017). This model is able to define refined horizontal areas of interest and evaluate them at a high spatial resolution, which is needed for the analysis of regional to local sources.

Furthermore, the work that has been put into the establishment of the EM27/SUN COCCON network will hopefully lead to a better worldwide coverage of FTIR spectrometers, especially in remote areas. The author of this thesis set up an EM27/SUN in a desert research facility in Namibia during January 2015, where measurements were taken for two years. Recently, the instrument was sent back for routinely checking the performance of this instrument. A continuous operation of the instrument in Namibia is intended. This site is especially interesting for satellite and model validation as it is a high albedo site in the desert.

List of Figures

2.1	Schematic representation of the vertical structure of the atmosphere.	6
2.2	Schematic depiction of the greenhouse effect	8
2.3	Schematic depiction of the Harmonic potential and the Morse-potential	9
2.4	Illustration of rotational-vibrational energy transitions	11
2.5	The four vibration modes of the CO ₂ molecule	12
2.6	Atmospheric transmission spectrum of CO ₂	13
2.7	Schematic depiction of a Michelson interferometer	15
3.1	Map of previous, operational and future TCCON stations	19
4.1	Inner body of the EM27/SUN spectrometer	24
4.2	Images of the solar disk on the aperture of the EM27/SUN	25
4.3	Illustration of a sampling artefact	26
4.4	Depiction of double passing	26
4.5	Depiction of channelling artefact	27
4.6	Setup of the lamp system	28
4.7	Transmission spectrum of 4 m lab air	30
4.8	Insensitivity of retrieved ILS parameters w.r.t. the probed H ₂ O column	30
4.9	Spectral windows of the target species	33
4.10	Calibration measurements at the KIT	34
5.1	ILS time series of the reference EM27/SUN	36
5.2	Total column time series for O ₂ , CO ₂ , CH ₄ and H ₂ O	38
5.3	X _{air} time series	40
5.4	XCO ₂ time series	41
5.5	XCO ₂ scatterplots	42
5.6	XCH ₄ time series	43
5.7	XCH ₄ scatterplots	43
5.8	XCH ₄ anomaly in March 2016	44
5.9	Modulation efficiencies for all EM27/SUN calibrated in Karlsruhe	46
5.10	Correlation of O ₂ and X _{gas} calibration factors	49
6.1	Total columns of O ₂ , CO ₂ and CH ₄ during the calibration measurements	53
6.2	Comparison of in situ and spectroscopically derived pressure data	54
6.3	XCO ₂ and XCH ₄ calibration measurements	55
6.4	Calibrated XCO ₂ and XCH ₄ values on 16 July 2014	56
6.5	Map showing the measurement stations around Berlin	57
6.6	Ceilometer measurements on 27 June 2014 in Berlin-Neukölln	59
6.7	Berlin campaign pressure time series	60

6.8	Berlin campaign XH ₂ O time series	61
6.9	Berlin campaign XCO ₂ time series	62
6.10	Berlin campaign XCH ₄ time series	62
6.11	Berlin campaign XCO ₂ and XCH ₄ measurements for 27 June 2014	63
6.12	Visual representation of the dispersion model	64
6.13	Observed and predicted XCO ₂ for 27 June, 03 July and 04 July	66
7.1	CO ₂ emission map of the Paris metropolitan region	70
7.2	Map of the CHIMERE modelling domain	72
7.3	Calibration measurements of XCO ₂ and XCH ₄ for the Paris campaign	73
7.4	Time series of observed XCO ₂ for the Paris campaign	76
7.5	Time series of observed XCH ₄ for the Paris campaign	76
7.6	XCO ₂ and XCH ₄ measurements for 07 May and 10 May 2015	77
7.7	Comparison of observed and modelled wind speed and wind direction	79
7.8	Time series of modelled XCO ₂ for the Paris campaign	80
7.9	Different contributions to the modelled XCO ₂	80
7.10	Δ XCO ₂ gradients of the different measurement sites	81
7.11	Observed and modelled XCO ₂ time series for 07 May and 10 May.	82
7.12	Comparison of modelled and observed gradients Δ XCO ₂ with RES as a back-ground site	83
7.13	Comparison of modelled and observed gradients Δ XCO ₂ with GIF as a back-ground site	83
8.1	Map showing the measurement stations around Tokyo (red stars). Map source: http://www.maps.google.de/	86
8.2	XCO ₂ and XCH ₄ calibration measurements before the Tokyo campaign	87
8.3	XCO ₂ and XCH ₄ calibration measurements after the Tokyo campaign	88
8.4	XCO ₂ and XCH ₄ calibration measurements at Karlsruhe	89
8.5	XCO ₂ and XCH ₄ time series during the Tokyo campaign	90
8.6	XCO ₂ and XCH ₄ values on several days of the Tokyo campaign	91
8.7	XCO ₂ and XCH ₄ measurement values on 01 March 2016	92
8.8	Comparison of EM27/SUN and OCO-2 XCO ₂ values	93

List of Tables

4.1	Target gases of the TCCON	22
4.2	Estimated uncertainties for various assumed error sources.	31
5.1	Sensitivity study on the effect of ILS changes on the retrieval	39
5.2	XCO ₂ biases between EM27/SUN and HR125 data sets.	42
5.3	XCH ₄ biases between EM27/SUN and HR125 data sets.	43
5.4	ILS parameters for all EM27/SUN calibrated in Karlsruhe.	45
5.5	Calibration factors for XCO ₂ , XCH ₄ and O ₂ with respect to the reference EM27/SUN	47
6.1	Compilation of ILS modulation efficiencies	52
6.2	Calibration factor for O ₂ for the different instruments	54
6.3	Berlin campaign XCO ₂ and XCH ₄ calibration factors	56
6.4	Locations and altitudes of the measurement sites during the Berlin field campaign	57
6.5	Main characteristics of each measurement day	58
6.6	Emission regions used in the dispersion model	65
7.1	Coordinates and altitudes of the measurement sites during the Paris field campaign	71
7.2	O ₂ , XCO ₂ and XCH ₄ calibration factors for the Paris campaign	74
7.3	Main characteristics of each measurement day during the Paris campaign	75
8.1	Coordinates and altitudes of the measurement sites during the Tokyo field campaign	86
8.2	Compilation of ILS modulation efficiencies during the Tokyo campaign	87
8.3	XCO ₂ and XCH ₄ calibration factors for the Tokyo campaign	88
8.4	XCO ₂ and XCH ₄ calibration factors between TCCON instruments	90

List of Acronyms

ADFC	Airmass-dependent correction factor
AIFC	Airmass-independent correction factor
BS	Beamsplitter
CAMS	Copernicus Atmosphere Monitoring Service
COCCON	Collaborative Carbon Column Observing Network
DMF	Dry air mole fraction
DOF	Degree of freedom
DWD	German weather service
ECMWF	European Centre for Medium Range Weather Forecast
FF	Fossil fuel CO ₂ emissions
FOV	Field of View
FTIR	Fourier transform infrared
FTS	Fourier transform spectrometer
FWHM	Full width half maximum
GHG	Greenhouse gas
GOSAT	Greenhouse Gases Observing Satellite
IER	Institut für Energiewirtschaft und Rationelle Energieanwendung
IFG	Interferogram
ILS	Instrumental line shape
IPCC	Intergovernmental Panel on Climate Change
IRWG	Infrared Working Group
JAXA	Japanese Aerospace Agency
KIT	Karlsruhe Institute of Technology
LERMA	Laboratoire d' Études du Rayonnement et de la Matière en Astrophysique et Atmosphères
LISA	Laboratoire Inter-Universitaire des Systèmes Atmosphériques
LSCE	Laboratoire des Sciences du Climat et de l'Environnement
ME	Modulation efficiency
MIR	Mid infrared
MOPD	Maximum optical path difference
NCEP	National Centers for Environmental Prediction
NDACC	Network for the Detection of Atmospheric Composition Change
NEE	Net ecosystem exchange
NIES	National Institute of Environmental Studies
NIR	Near infrared
OCO-2	Orbiting Carbon Observatory-2
RF	Radiative forcing
SEA	Solar elevation angle
SZA	Solar zenith angle

TCCON	Total Carbon Column Observing Network
TOA	Top of the atmosphere
TSI	Total solar irradiance

Bibliography

- Agustí-Panareda, A., Massart, S., Chevallier, F., Boussetta, S., Balsamo, G., Beljaars, A., Ciais, P., Deutscher, N. M., Engelen, R., Jones, L., Kivi, R., Paris, J.-D., Peuch, V.-H., Sherlock, V., Vermeulen, A. T., Wennberg, P. O., and Wunch, D.: Forecasting global atmospheric CO₂, *Atmospheric Chemistry and Physics*, 14, 11 959–11 983, <https://doi.org/10.5194/acp-14-11959-2014>, 2014.
- Andres, R. J., Boden, T. A., and Higdon, D.: A new evaluation of the uncertainty associated with CDIAC estimates of fossil fuel carbon dioxide emission, *Tellus B: Chemical and Physical Meteorology*, 66, 23 616, <https://doi.org/10.3402/tellusb.v66.23616>, 2014.
- Baldauf, M., Seifert, A., Förstner, J., Majewski, D., Raschendorfer, M., and Reinhardt, T.: Operational Convective-Scale Numerical Weather Prediction with the COSMO Model: Description and Sensitivities, *Monthly Weather Review*, 139, 3887–3905, <https://doi.org/10.1175/MWR-D-10-05013.1>, 2011.
- Beer, R.: *Remote Sensing by Fourier Transform Spectrometry*, Wiley Interscience publication, <https://doi.org/10.1080/01431169508954378>, 1992.
- Bernath, P. F., McElroy, C. T., Abrams, M. C., Boone, C. D., Butler, M., Camy-Peyret, C., Carleer, M., Clerbaux, C., Coheur, P.-F., Colin, R., DeCola, P., DeMazière, M., Drummond, J. R., Dufour, D., Evans, W. F. J., Fast, H., Fussen, D., Gilbert, K., Jennings, D. E., Llewellyn, E. J., Lowe, R. P., Mahieu, E., McConnell, J. C., McHugh, M., McLeod, S. D., Michaud, R., Midwinter, C., Nassar, R., Nichitiu, F., Nowlan, C., Rinsland, C. P., Rochon, Y. J., Rowlands, N., Semeniuk, K., Simon, P., Skelton, R., Sloan, J. J., Soucy, M.-A., Strong, K., Tremblay, P., Turnbull, D., Walker, K. A., Walkty, I., Wardle, D. A., Wehrle, V., Zander, R., and Zou, J.: Atmospheric Chemistry Experiment (ACE): Mission overview, *Geophysical Research Letters*, 32, <https://doi.org/10.1029/2005GL022386>, 115S01, 2005.
- Boon, A., Broquet, G., Clifford, D. J., Chevallier, F., Butterfield, D. M., Pison, I., Ramonet, M., Paris, J.-D., and Ciais, P.: Analysis of the potential of near-ground measurements of CO₂ and CH₄ in London, UK, for the monitoring of city-scale emissions using an atmospheric transport model, *Atmospheric Chemistry and Physics*, 16, 6735–6756, <https://doi.org/10.5194/acp-16-6735-2016>, 2016.
- Bösch, H., Deutscher, N. M., Warneke, T., Byckling, K., Cogan, A. J., Griffith, D. W. T., Notholt, J., Parker, R. J., and Wang, Z.: HDO/H₂O ratio retrievals from GOSAT, *Atmospheric Measurement Techniques*, 6, 599–612, <https://doi.org/10.5194/amt-6-599-2013>, 2013.
- Boussetta, S., Balsamo, G., Beljaars, A. C. M., Panareda, A. A., Calvet, J.-C., Jacobs, C., van den Hurk, B., Viterbo, P., Lafont, S., Dutra, E., Jarlan, L., Balzarolo, M., Papale, D., and van der Werf, G.: Natural land carbon dioxide exchanges in the ECMWF integrated

- forecasting system: Implementation and offline validation, *Journal of Geophysical Research: Atmospheres*, 118, 5923–5946, <https://doi.org/10.1002/jgrd.50488>, 2013.
- Brandt, A. R., Heath, G. A., Kort, E. A., O’Sullivan, F., Pétron, G., Jordaan, S. M., Tans, P., Wilcox, J., Gopstein, A. M., Arent, D., Wofsy, S., Brown, N. J., Bradley, R., Stucky, G. D., Eardley, D., and Harriss, R.: Methane Leaks from North American Natural Gas Systems, *Science*, 343, 733–735, <https://doi.org/10.1126/science.1247045>, 2014.
- Bréon, F. M., Broquet, G., Puygrenier, V., Chevallier, F., Xueref-Remy, I., Ramonet, M., Dieudonné, E., Lopez, M., Schmidt, M., Perrussel, O., and Ciais, P.: An attempt at estimating Paris area CO₂ emissions from atmospheric concentration measurements, *Atmospheric Chemistry and Physics*, 15, 1707–1724, <https://doi.org/10.5194/acp-15-1707-2015>, 2015.
- Butz, A., Guerlet, S., Hasekamp, O., Schepers, D., Galli, A., Aben, I., Frankenberg, C., Hartmann, J.-M., Tran, H., Kuze, A., Keppel-Aleks, G., Toon, G., Wunch, D., Wennberg, P., Deutscher, N., Griffith, D., Macatangay, R., Messerschmidt, J., Notholt, J., and Warneke, T.: Toward accurate CO₂ and CH₄ observations from GOSAT, *Geophys. Res. Lett.*, 38, <https://doi.org/10.1029/2011GL047888>, 2011.
- Butz, A., Dinger, A. S., Bobrowski, N., Kostinek, J., Fieber, L., Fischerkeller, C., Giuffrida, G. B., Hase, F., Klappenbach, F., Kuhn, J., Lübcke, P., Tirpitz, L., and Tu, Q.: Remote sensing of volcanic CO₂, HF, HCl, SO₂, and BrO in the downwind plume of Mt. Etna, *Atmospheric Measurement Techniques*, 10, 1–14, <https://doi.org/10.5194/amt-10-1-2017>, 2017.
- Chen, J., Viatte, C., Hedelius, J. K., Jones, T., Franklin, J. E., Parker, H., Gottlieb, E. W., Wennberg, P. O., Dubey, M. K., and Wofsy, S. C.: Differential column measurements using compact solar-tracking spectrometers, *Atmospheric Chemistry and Physics*, 16, 8479–8498, <https://doi.org/10.5194/acp-16-8479-2016>, 2016.
- Davis, S., Abrams, M. C., and Brault, J. W.: *Fourier Transform Spectrometry*, Academic press, 2010.
- de Laat, A. T. J., Gloudemans, A. M. S., Schrijver, H., Aben, I., Nagahama, Y., Suzuki, K., Mahieu, E., Jones, N. B., Paton-Walsh, C., Deutscher, N. M., Griffith, D. W. T., De Mazière, M., Mittermeier, R. L., Fast, H., Notholt, J., Palm, M., Hawat, T., Blumenstock, T., Hase, F., Schneider, M., Rinsland, C., Dzhola, A. V., Grechko, E. I., Poberovskii, A. M., Makarova, M. V., Mellqvist, J., Strandberg, A., Sussmann, R., Borsdorff, T., and Rettinger, M.: Validation of five years (2003–2007) of SCIAMACHY CO total column measurements using ground-based spectrometer observations, *Atmospheric Measurement Techniques*, 3, 1457–1471, <https://doi.org/10.5194/amt-3-1457-2010>, 2010.
- De Mazière, M., Thompson, A. M., Kurylo, M. J., Wild, J. D., Bernhard, G., Blumenstock, T., Braathen, G. O., Hannigan, J. W., Lambert, J.-C., Leblanc, T., McGee, T. J., Nedoluha, G., Petropavlovskikh, I., Seckmeyer, G., Simon, P. C., Steinbrecht, W., and Strahan, S. E.: The Network for the Detection of Atmospheric Composition Change (NDACC): history, status and perspectives, *Atmospheric Chemistry and Physics*, 18, 4935–4964, <https://doi.org/10.5194/acp-18-4935-2018>, 2018.
- Demtröder, W.: *Experimentalphysik 3: Atome, Moleküle und Festkörper*, Springer-Verlag Berlin heidelberg, <https://doi.org/10.1007/b139046>, 2010.
- Deutscher, N. M., Sherlock, V., Mikaloff Fletcher, S. E., Griffith, D. W. T., Notholt, J., Macatangay, R., Connor, B. J., Robinson, J., Shiona, H., Velasco, V. A., Wang, Y., Wennberg, P. O.,

- and Wunch, D.: Drivers of column-average CO₂ variability at Southern Hemispheric Total Carbon Column Observing Network sites, *Atmospheric Chemistry and Physics*, 14, 9883–9901, <https://doi.org/10.5194/acp-14-9883-2014>, 2014.
- Dhakal, S.: Urban energy use and carbon emissions from cities in China and policy implications, *Energy Policy*, 37, 4208 – 4219, <https://doi.org/10.1016/j.enpol.2009.05.020>, 2009.
- Dlugokencky, E. J., Masarie, K. A., Tans, P. P., Conway, T. J., and Xiong, X.: Is the amplitude of the methane seasonal cycle changing?, *Atmospheric Environment*, 31, 21–26, [https://doi.org/10.1016/S1352-2310\(96\)00174-4](https://doi.org/10.1016/S1352-2310(96)00174-4), 1997.
- Dlugokencky, E. J., Nisbet, E. G., Fisher, R., and Lowry, D.: Global atmospheric methane: budget, changes and dangers, *Atmospheric Environment*, 369, 2058–2072, <https://doi.org/10.1098/rsta.2010.0341>, 2011.
- Dohe, S.: Measurements of atmospheric CO₂ columns using ground-based FTIR spectra, Ph.D. thesis, Karlsruhe Institute of Technology, 2013.
- Dohe, S., Sherlock, V., Hase, F., Gisi, M., Robinson, J., Sepúlveda, E., Schneider, M., and Blumenstock, T.: A method to correct sampling ghosts in historic near-infrared Fourier transform spectrometer (FTS) measurements, *Atmospheric Measurement Techniques*, 6, 1981–1992, <https://doi.org/10.5194/amt-6-1981-2013>, 2013.
- Emeis, S., Schäfer, K., Münkler, C., Friedl, R., and Suppan, P.: Evaluation of the Interpretation of Ceilometer Data with RASS and Radiosonde Data, *Boundary-Layer Meteorology*, 143, 25–35, <https://doi.org/10.1007/s10546-011-9604-6>, 2012.
- Etheridge, D. M., Steele, L. P., Langenfelds, R. L., Francey, R. J., Barnola, J.-M., and Morgan, V. I.: Natural and anthropogenic changes in atmospheric CO₂ over the last 1000 years from air in Antarctic ice and firn, *Journal of Geophysical Research: Atmospheres*, 101, 4115–4128, <https://doi.org/10.1029/95JD03410>, 1996.
- Frankenberg, C., Pollock, R., Lee, R. A. M., Rosenberg, R., Blavier, J.-F., Crisp, D., O'Dell, C. W., Osterman, G. B., Roehl, C., Wennberg, P. O., and Wunch, D.: The Orbiting Carbon Observatory (OCO-2): spectrometer performance evaluation using pre-launch direct sun measurements, *Atmospheric Measurement Techniques*, 8, 301–313, <https://doi.org/10.5194/amt-8-301-2015>, 2015.
- Frey, M., Hase, F., Blumenstock, T., Groß, J., Kiel, M., Mengistu Tsidu, G., Schäfer, K., Sha, M. K., and Orphal, J.: Calibration and instrumental line shape characterization of a set of portable FTIR spectrometers for detecting greenhouse gas emissions, *Atmospheric Measurement Techniques*, 8, 3047–3057, <https://doi.org/10.5194/amt-8-3047-2015>, 2015.
- Frey, M., Sha, M. K., Hase, F., Kiel, M., Blumenstock, T., Harig, R., Surawicz, G., Deutscher, N. M., Shiomi, K., Franklin, J., Bösch, H., Chen, J., Grutter, M., Ohyama, H., Sun, Y., Butz, A., Mengistu Tsidu, G., Ene, D., Wunch, D., Cao, Z., Garcia, O., Ramonet, M., Vogel, F., and Orphal, J.: Building the COllaborative Carbon Column Observing Network (COCCON): Long term stability and ensemble performance of the EM27/SUN Fourier transform spectrometer, *Atmospheric Measurement Techniques Discussions*, 2018, 1–34, <https://doi.org/10.5194/amt-2018-146>, 2018.
- Geibel, M. C., Messerschmidt, J., Gerbig, C., Blumenstock, T., Chen, H., Hase, F., Kolle, O., Lavrič, J. V., Notholt, J., Palm, M., Rettinger, M., Schmidt, M., Sussmann, R., Warneke,

- T., and Feist, D. G.: Calibration of column-averaged CH₄ over European TCCON FTS sites with airborne in-situ measurements, *Atmospheric Chemistry and Physics*, 12, 8763–8775, <https://doi.org/10.5194/acp-12-8763-2012>, 2012.
- Gisi, M., Hase, F., Dohe, S., and Blumenstock, T.: Camtracker: a new camera controlled high precision solar tracker system for FTIR-spectrometers, *Atmospheric Measurement Techniques*, 4, 47–54, <https://doi.org/10.5194/amt-4-47-2011>, 2011.
- Gisi, M., Hase, F., Dohe, S., Blumenstock, T., Simon, A., and Keens, A.: XCO₂-measurements with a tabletop FTS using solar absorption spectroscopy, *Atmospheric Measurement Techniques*, 5, 2969–2980, <https://doi.org/10.5194/amt-5-2969-2012>, 2012.
- GLOBALVIEW-CO2: Cooperative Global Atmospheric Data Integration Project. 2013, updated annually. Multi-laboratory compilation of synchronized and gap-filled atmospheric carbon dioxide records for the period 1979-2012. Compiled by NOAA Global Monitoring Division: Boulder, Colorado, <https://doi.org/10.3334/OBSPACK/1002>, 2013.
- Gordon, I., S. Rothman, L., and C. Toon, G.: Revision of spectral parameters for the B and γ -bands of oxygen and their validation against atmospheric spectra, *Journal of Quantitative Spectroscopy & Radiative Transfer*, 112, 2310–2322, <https://doi.org/10.1016/j.jqsrt.2011.05.007>, 2011.
- Guerlet, S., Basu, S., Butz, A., Krol, M., Hahne, P., Houweling, S., Hasekamp, O., and Aben, I.: Reduced carbon uptake during the 2010 Northern Hemisphere summer from GOSAT, *Geophysical Research Letters*, 40, 2378–2383, <https://doi.org/10.1002/grl.50402>, 2013.
- Haken, H. and Wolf, H. C.: *Molekülphysik und Quantenchemie: Einführung in die experimentellen und theoretischen Grundlagen*, Springer-Verlag Berlin Heidelberg, <https://doi.org/10.1007/3-540-30315-4>, 2006.
- Hansen, J., Ruedy, R., Sato, M., and Lo, K.: Global surface temperature change, *Reviews of Geophysics*, 48, <https://doi.org/10.1029/2010RG000345>, 2010.
- Hase, F.: Improved instrumental line shape monitoring for the ground-based, high-resolution FTIR spectrometers of the Network for the Detection of Atmospheric Composition Change, *Atmospheric Measurement Techniques*, 5, 603–610, <https://doi.org/10.5194/amt-5-603-2012>, 2012.
- Hase, F., Blumenstock, T., and Paton-Walsh, C.: Analysis of the instrumental line shape of high-resolution Fourier transform IR spectrometers with gas cell measurements and new retrieval software, *Appl. Opt.*, 38, 3417–3422, <https://doi.org/10.1364/AO.38.003417>, 1999.
- Hase, F., Hannigan, J., T. Coffey, M., Goldman, A., Höpfner, M., Jones, N., P. Rinsland, C., and Wood, S.: Intercomparison of retrieval codes used for the analysis of high-resolution, ground-based FTIR measurements, *Journal of Quantitative Spectroscopy & Radiative Transfer*, 87, 25–52, <https://doi.org/10.1016/j.jqsrt.2003.12.008>, 2004.
- Hase, F., Drouin, B. J., Roehl, C. M., Toon, G. C., Wennberg, P. O., Wunch, D., Blumenstock, T., Desmet, F., Feist, D. G., Heikkinen, P., De Mazière, M., Rettinger, M., Robinson, J., Schneider, M., Sherlock, V., Sussmann, R., Té, Y., Warneke, T., and Weinzierl, C.: Calibration of sealed HCl cells used for TCCON instrumental line shape monitoring, *Atmospheric Measurement Techniques*, 6, 3527–3537, <https://doi.org/10.5194/amt-6-3527-2013>, 2013.

- Hase, F., Frey, M., Blumenstock, T., Groß, J., Kiel, M., Kohlhepp, R., Mengistu Tsidu, G., Schäfer, K., Sha, M. K., and Orphal, J.: Application of portable FTIR spectrometers for detecting greenhouse gas emissions of the major city Berlin, *Atmospheric Measurement Techniques*, 8, 3059–3068, <https://doi.org/10.5194/amt-8-3059-2015>, 2015.
- Hase, F., Frey, M., Kiel, M., Blumenstock, T., Harig, R., Keens, A., and Orphal, J.: Addition of a channel for XCO observations to a portable FTIR spectrometer for greenhouse gas measurements, *Atmospheric Measurement Techniques*, 9, 2303–2313, <https://doi.org/10.5194/amt-9-2303-2016>, 2016.
- Hedelius, J. K., Viatte, C., Wunch, D., Roehl, C. M., Toon, G. C., Chen, J., Jones, T., Wofsy, S. C., Franklin, J. E., Parker, H., Dubey, M. K., and Wennberg, P. O.: Assessment of errors and biases in retrievals of X_{CO₂}, X_{CH₄}, X_{CO}, and X_{N₂O} from a 0.5 cm⁻¹ resolution solar-viewing spectrometer, *Atmospheric Measurement Techniques*, 9, 3527–3546, <https://doi.org/10.5194/amt-9-3527-2016>, 2016.
- Hedelius, J. K., Parker, H., Wunch, D., Roehl, C. M., Viatte, C., Newman, S., Toon, G. C., Podolske, J. R., Hillyard, P. W., Iraci, L. T., Dubey, M. K., and Wennberg, P. O.: Intercomparability of X_{CO₂} and X_{CH₄} from the United States TCCON sites, *Atmospheric Measurement Techniques*, 10, 1481–1493, <https://doi.org/10.5194/amt-10-1481-2017>, 2017.
- Heinle, L. and Chen, J.: Automated enclosure and protection system for compact solar-tracking spectrometers, *Atmospheric Measurement Techniques*, 11, 2173–2185, <https://doi.org/10.5194/amt-11-2173-2018>, 2018.
- Humlicek, J.: An Efficient Method for Evaluation of the Complex Probability Function: The Voigt Function and its Derivatives, *Journal of Quantitative Spectroscopy and Radiative Transfer*, 21, 309–313, [https://doi.org/10.1016/0022-4073\(79\)90062-1](https://doi.org/10.1016/0022-4073(79)90062-1), 1979.
- International Energy Agency: World Energy Outlook, IEA Publications, <https://doi.org/10.1787/20725302>, 2017.
- IPCC-WG1: Climate Change 2013: The Physical Science Basis. Contribution of Working Group I for the Fifth Assessment Report of the Intergovernmental Panel on Climate Change [Stocker, T.F., D. Qin, G.-K. Plattner, M. Tignor, S.K. Allen, J. Boschung, A. Nauels, Y. Xia, V. Bex and P.M. Midgley (eds.)], Cambridge University Press, <https://doi.org/10.1017/CBO9781107415324>, 2013.
- IPCC-WG3: Climate Change 2014: Mitigation of Climate Change. Contribution of Working Group III to the Fifth Assessment Report of the Intergovernmental Panel on Climate Change [Edenhofer, O., R. Pichs-Madruga, Y. Sokona, E. Farahani, S. Kadner, K. Seyboth, A. Adler, I. Baum, S. Brunner, P. Eickemeier, B. Kriemann, J. Savolainen, S. Schlömer, C. von Stechow, T. Zwickel and J.C. Minx (eds.)], Cambridge University Press, <https://doi.org/10.1017/CBO9781107415416>, 2014.
- Janssens-Maenhout, G., Dentener, F., Aardenne, J., Monni, S., Pagliari, V., Orlandini, L., Klimont, Z., Kurokawa, J.-I., Akimoto, H., Ohara, T., Wankmüller, R., Battye, B., Grano, D., Zuber, A., and Keating, T.: EDGAR-HTAP: a harmonized gridded air pollution emission dataset based on national inventories, Publications Office of the European Union, <https://doi.org/10.2788/14069>, 2012.
- Kalnay, E., Kanamitsu, M., Kistler, R., Collins, W., Deaven, D., Gandin, L., Iredell, M., Saha, S., White, G., Woollen, J., Zhu, Y., Leetmaa, A., Reynolds, R., Chelliah, M., Ebisuzaki, W.,

- Higgins, W., Janowiak, J., Mo, K. C., Ropelewski, C., Wang, J., Jenne, R., and Joseph, D.: The NCEP/NCAR 40-Year Reanalysis Project, *Bulletin of the American Meteorological Society*, 77, 437–471, [https://doi.org/10.1175/1520-0477\(1996\)077<0437:TNYRP;2.0.CO;2](https://doi.org/10.1175/1520-0477(1996)077<0437:TNYRP;2.0.CO;2), 1996.
- Karion, A., Sweeney, C., Tans, P., and Newberger, T.: AirCore: An Innovative Atmospheric Sampling System, *Journal of Atmospheric and Oceanic Technology*, 27, 1839–1853, <https://doi.org/10.1175/2010JTECHA1448.1>, 2010.
- Keppel-Aleks, G., Toon, G. C., Wennberg, P. O., and Deutscher, N. M.: Reducing the impact of source brightness fluctuations on spectra obtained by Fourier-transform spectrometry, *Appl. Opt.*, 46, 4774–4779, <https://doi.org/10.1364/AO.46.004774>, 2007.
- Kiel, M., Hase, F., Blumenstock, T., and Kirner, O.: Comparison of XCO abundances from the Total Carbon Column Observing Network and the Network for the Detection of Atmospheric Composition Change measured in Karlsruhe, *Atmospheric Measurement Techniques*, 9, 2223–2239, <https://doi.org/10.5194/amt-9-2223-2016>, 2016a.
- Kiel, M., Wunch, D., Wennberg, P. O., Toon, G. C., Hase, F., and Blumenstock, T.: Improved retrieval of gas abundances from near-infrared solar FTIR spectra measured at the Karlsruhe TCCON station, *Atmospheric Measurement Techniques*, 9, 669–682, <https://doi.org/10.5194/amt-9-669-2016>, 2016b.
- Klappenbach, F., Bertleff, M., Kostinek, J., Hase, F., Blumenstock, T., Agusti-Panareda, A., Razingerg, M., and Butz, A.: Accurate mobile remote sensing of XCO₂ and XCH₄ latitudinal transects from aboard a research vessel, *Atmospheric Measurement Techniques*, 8, 5023–5038, <https://doi.org/10.5194/amt-8-5023-2015>, 2015.
- Lac, C., Donnelly, R. P., Masson, V., Pal, S., Riette, S., Donier, S., Queguiner, S., Tanguy, G., Ammoura, L., and Xueref-Remy, I.: CO₂ dispersion modelling over Paris region within the CO₂-MEGAPARIS project, *Atmospheric Chemistry and Physics*, 13, 4941–4961, <https://doi.org/10.5194/acp-13-4941-2013>, 2013.
- Lamouroux, J., Tran, H., Laraia, A., Gamache, R., Rothman, L., Gordon, I., and Hartmann, J.-M.: Updated database plus software for line-mixing in CO₂ infrared spectra and their test using laboratory spectra in the 1.5 - 2.3 μm region, *Journal of Quantitative Spectroscopy and Radiative Transfer*, 111, 2321 – 2331, <https://doi.org/https://doi.org/10.1016/j.jqsrt.2010.03.006>, 2010.
- Latoska, A.: Erstellung eines räumlich hoch aufgelösten Emissionsinventar von Luftschadstoffen am Beispiel von Frankreich im Jahr 2005, Master thesis, Master's thesis, Institut für Energiewirtschaft und Rationelle Energieanwendung, Universität Stuttgart, 2009.
- Lauvaux, T., Miles, N. L., Richardson, S. J., Deng, A., Stauffer, D. R., Davis, K. J., Jacobson, G., Rella, C., Calonder, G.-P., and DeCola, P. L.: Urban Emissions of CO₂ from Davos, Switzerland: The First Real-Time Monitoring System Using an Atmospheric Inversion Technique, *Journal of Applied Meteorology and Climatology*, 52, 2654–2668, <https://doi.org/10.1175/JAMC-D-13-038.1>, 2013.
- Le Quéré, C., Peters, G. P., Andres, R. J., Andrew, R. M., Boden, T. A., Ciais, P., Friedlingstein, P., Houghton, R. A., Marland, G., Moriarty, R., Sitch, S., Tans, P., Arneeth, A., Arvanitis, A., Bakker, D. C. E., Bopp, L., Canadell, J. G., Chini, L. P., Doney, S. C., Harper, A., Harris, I., House, J. I., Jain, A. K., Jones, S. D., Kato, E., Keeling, R. F., Klein Goldewijk,

- K., Körtzinger, A., Koven, C., Lefèvre, N., Maignan, F., Omar, A., Ono, T., Park, G.-H., Pfeil, B., Poulter, B., Raupach, M. R., Regnier, P., Rödenbeck, C., Saito, S., Schwinger, J., Segsneider, J., Stocker, B. D., Takahashi, T., Tilbrook, B., van Heuven, S., Viovy, N., Wanninkhof, R., Wiltshire, A., and Zaehle, S.: Global carbon budget 2013, *Earth System Science Data*, 6, 235–263, <https://doi.org/10.5194/essd-6-235-2014>, 2014.
- Le Quéré, C., Andrew, R. M., Friedlingstein, P., Sitch, S., Pongratz, J., Manning, A. C., Korsbakken, J. I., Peters, G. P., Canadell, J. G., Jackson, R. B., Boden, T. A., Tans, P. P., Andrews, O. D., Arora, V. K., Bakker, D. C. E., Barbero, L., Becker, M., Betts, R. A., Bopp, L., Chevallier, F., Chini, L. P., Ciais, P., Cosca, C. E., Cross, J., Currie, K., Gasser, T., Harris, I., Hauck, J., Haverd, V., Houghton, R. A., Hunt, C. W., Hurtt, G., Ilyina, T., Jain, A. K., Kato, E., Kautz, M., Keeling, R. F., Klein Goldewijk, K., Körtzinger, A., Landschützer, P., Lefèvre, N., Lenton, A., Lienert, S., Lima, I., Lombardozzi, D., Metzl, N., Millero, F., Monteiro, P. M. S., Munro, D. R., Nabel, J. E. M. S., Nakaoka, S.-I., Nojiri, Y., Padin, X. A., Peregón, A., Pfeil, B., Pierrot, D., Poulter, B., Rehder, G., Reimer, J., Rödenbeck, C., Schwinger, J., Séférian, R., Skjelvan, I., Stocker, B. D., Tian, H., Tilbrook, B., Tubiello, F. N., van der Laan-Luijkx, I. T., van der Werf, G. R., van Heuven, S., Viovy, N., Vuichard, N., Walker, A. P., Watson, A. J., Wiltshire, A. J., Zaehle, S., and Zhu, D.: Global Carbon Budget 2017, *Earth System Science Data*, 10, 405–448, <https://doi.org/10.5194/essd-10-405-2018>, 2018.
- Liu, Y., Lin, J., Huang, G., Guo, Y., and Duan, C.: Simple empirical analytical approximation to the Voigt profile, *J. Opt. Soc. Am. B*, 18, 666–672, <https://doi.org/10.1364/JOSAB.18.000666>, 2001.
- Massart, S., Agustí-Panareda, A., Aben, I., Butz, A., Chevallier, F., Crevoisier, C., Engelen, R., Frankenberg, C., and Hasekamp, O.: Assimilation of atmospheric methane products into the MACC-II system: from SCIAMACHY to TANSO and IASI, *Atmospheric Chemistry and Physics*, 14, 6139–6158, <https://doi.org/10.5194/acp-14-6139-2014>, 2014.
- McKain, K., Wofsy, S. C., Nehr Korn, T., Eluszkiewicz, J., Ehleringer, J. R., and Stephens, B. B.: Assessment of ground-based atmospheric observations for verification of greenhouse gas emissions from an urban region, *Proceedings of the National Academy of Sciences*, 109, 8423–8428, <https://doi.org/10.1073/pnas.1116645109>, 2012.
- Menut, L., Bessagnet, B., Khvorostyanov, D., Beekmann, M., Blond, N., Colette, A., Coll, I., Curci, G., Foret, G., Hodzic, A., Mailler, S., Meleux, F., Monge, J.-L., Pison, I., Siour, G., Turquety, S., Valari, M., Vautard, R., and Vivanco, M. G.: CHIMERE 2013: a model for regional atmospheric composition modelling, *Geoscientific Model Development*, 6, 981–1028, <https://doi.org/10.5194/gmd-6-981-2013>, 2013.
- Messerschmidt, J., Macatangay, R., Notholt, J., Petri, C., Warneke, T., and Weinzierl, C.: Side by side measurements of CO₂ by ground-based Fourier transform spectrometry (FTS), *Tellus B*, 62, 749–758, <https://doi.org/10.1111/j.1600-0889.2010.00491.x>, 2010.
- Morino, I., Uchino, O., Inoue, M., Yoshida, Y., Yokota, T., Wennberg, P. O., Toon, G. C., Wunch, D., Roehl, C. M., Notholt, J., Warneke, T., Messerschmidt, J., Griffith, D. W. T., Deutscher, N. M., Sherlock, V., Connor, B., Robinson, J., Sussmann, R., and Rettinger, M.: Preliminary validation of column-averaged volume mixing ratios of carbon dioxide and methane retrieved from GOSAT short-wavelength infrared spectra, *Atmospheric Measurement Techniques*, 4, 1061–1076, <https://doi.org/10.5194/amt-4-1061-2011>, 2011.

- Münkel, C., Eresmaa, N., Räsänen, J., and Karppinen, A.: Retrieval of mixing height and dust concentration with lidar ceilometer, *Boundary-Layer Meteorology*, 124, 117–128, <https://doi.org/10.1007/s10546-006-9103-3>, 2007.
- Myrhe, G., Shindell, D., Bréon, F.-M., Collins, W., Fuglestvedt, J., Huang, J., Koch, D., Lamarque, J.-F., Lee, D., Mendoza, B., Nakajima, T., Robock, A., Stephens, G., Takemura, T., and Zhang, H.: *Climate Change 2013 – The Physical Science Basis: Working Group I Contribution to the Fifth Assessment Report of the Intergovernmental Panel on Climate Change*, chap. 2013: Anthropogenic and Natural Radiative Forcing., pp. 659–740, Cambridge University Press, <https://doi.org/10.1017/CBO9781107415324.018>, 2013.
- Nassar, R., Hill, T. G., McLinden, C. A., Wunch, D., Jones, D. B. A., and Crisp, D.: Quantifying CO₂ Emissions From Individual Power Plants From Space, *Geophysical Research Letters*, 44, 10,045–10,053, <https://doi.org/10.1002/2017GL074702>, 2017.
- Olsen, S. C. and Randerson, J. T.: Differences between surface and column atmospheric CO₂ and implications for carbon cycle research, *Journal of Geophysical Research: Atmospheres*, 109, <https://doi.org/10.1029/2003JD003968>, 2004.
- Ostler, A., Sussmann, R., Rettinger, M., Deutscher, N. M., Dohe, S., Hase, F., Jones, N., Palm, M., and Sinnhuber, B.-M.: Multistation intercomparison of column-averaged methane from NDACC and TCCON: impact of dynamical variability, *Atmospheric Measurement Techniques*, 7, 4081–4101, <https://doi.org/10.5194/amt-7-4081-2014>, 2014.
- Petri, C., Warneke, T., Jones, N., Ridder, T., Messerschmidt, J., Weinzierl, T., Geibel, M., and Notholt, J.: Remote sensing of CO₂ and CH₄ using solar absorption spectrometry with a low resolution spectrometer, *Atmospheric Measurement Techniques*, 5, 1627–1635, <https://doi.org/10.5194/amt-5-1627-2012>, 2012.
- Petty, M. C.: *Molecular electronics: from principles to practice*, Wiley, <https://doi.org/doi:10.1002/9780470723890>, 2007.
- Ponater, M., Dietmüller, S., and Sausen, R.: *Atmospheric Physics: Background - Methods - Trends*, Chapter Greenhouse Effect, Radiative Forcing and Climate Sensitivity, Springer-Verlag Berlin Heidelberg, https://doi.org/10.1007/978-3-642-30183-4_6, 2012.
- Reuter, M., Bovensmann, H., Buchwitz, M., Burrows, J., Deutscher, N., Heymann, J., Rozanov, A., Schneising, O., Suto, H., Toon, G., and Warneke, T.: On the potential of the 2041–2047 nm spectral region for remote sensing of atmospheric CO₂ isotopologues, *Journal of Quantitative Spectroscopy and Radiative Transfer*, 113, 2009–2017, <https://doi.org/10.1016/j.jqsrt.2012.07.013>, 2012.
- Rodgers, C. D.: *Inverse Methods for Atmospheric Sounding: Theory and Practice*, Series on Atmospheric, Oceanic and Planetary Physics, World Scientific, <https://doi.org/10.1142/9789812813718>, 2000.
- Saunio, M., Bousquet, P., Poulter, B., Peregon, A., Ciais, P., Canadell, J. G., Dlugokencky, E. J., Etiope, G., Bastviken, D., Houweling, S., Janssens-Maenhout, G., Tubiello, F. N., Castaldi, S., Jackson, R. B., Alexe, M., Arora, V. K., Beerling, D. J., Bergamaschi, P., Blake, D. R., Brailsford, G., Brovkin, V., Bruhwiler, L., Crevoisier, C., Crill, P., Covey, K., Curry, C., Frankenberg, C., Gedney, N., Höglund-Isaksson, L., Ishizawa, M., Ito, A., Joos, F., Kim, H.-S., Kleinen, T., Krummel, P., Lamarque, J.-F., Langenfelds, R., Locatelli, R., Machida, T.,

- Maksyutov, S., McDonald, K. C., Marshall, J., Melton, J. R., Morino, I., Naik, V., O'Doherty, S., Parmentier, F.-J. W., Patra, P. K., Peng, C., Peng, S., Peters, G. P., Pison, I., Prigent, C., Prinn, R., Ramonet, M., Riley, W. J., Saito, M., Santini, M., Schroeder, R., Simpson, I. J., Spahni, R., Steele, P., Takizawa, A., Thornton, B. F., Tian, H., Tohjima, Y., Viovy, N., Voulgarakis, A., van Weele, M., van der Werf, G. R., Weiss, R., Wiedinmyer, C., Wilton, D. J., Wiltshire, A., Worthy, D., Wunch, D., Xu, X., Yoshida, Y., Zhang, B., Zhang, Z., and Zhu, Q.: The global methane budget 2000–2012, *Earth System Science Data*, 8, 697–751, <https://doi.org/10.5194/essd-8-697-2016>, 2016.
- Schepers, D., Guerlet, S., Butz, A., Landgraf, J., Frankenberg, C., Hasekamp, O., F. Blavier, J., Deutscher, N., W. T. Griffith, D., Hase, F., Kyrö, E., Morino, I., Sherlock, V., Sussmann, R., and Aben, I.: Methane retrievals from Greenhouse Gases Observing Satellite (GOSAT) shortwave infrared measurements: Performance comparison of proxy and physics retrieval algorithms, *Journal of Geophysikal Research–Atmospheres*, 117, <https://doi.org/10.1029/2012JD017549>, 2012.
- Schlager, H., Grewe, V., and Roiger, A.: *Atmospheric Physics: Background - Methods - Trends*, Chapter Chemical Composition of the Atmosphere, Springer-Verlag Berlin Heidelberg, https://doi.org/10.1007/978-3-642-30183-4_2, 2012.
- Schneider, M. and Hase, F.: Ground-based FTIR water vapour profile analyses, *Atmospheric Measurement Techniques*, 2, 609–619, <https://doi.org/10.5194/amt-2-609-2009>, 2009.
- Schröter, J., Rieger, D., Stassen, C., Vogel, H., Weimer, M., Werchner, S., Förstner, J., Prill, F., Reinert, D., Zängl, G., Giorgetta, M., Ruhnke, R., Vogel, B., and Braesicke, P.: ICON-ART 2.1 – A flexible tracer framework and its application for composition studies in numerical weather forecasting and climate simulations, *Geoscientific Model Development Discussions*, 2018, 1–37, <https://doi.org/10.5194/gmd-2017-286>, 2018.
- Sepúlveda, E., Schneider, M., Hase, F., García, O. E., Gomez-Pelaez, A., Dohe, S., Blumenstock, T., and Guerra, J. C.: Long-term validation of tropospheric column-averaged CH₄ mole fractions obtained by mid-infrared ground-based FTIR spectrometry, *Atmospheric Measurement Techniques*, 5, 1425–1441, <https://doi.org/10.5194/amt-5-1425-2012>, 2012.
- Shepard, D.: A Two-dimensional Interpolation Function for Irregularly-spaced Data, in: *Proceedings of the 1968 23rd ACM National Conference*, pp. 517–524, ACM, New York, NY, USA, <https://doi.org/10.1145/800186.810616>, 1968.
- Staufer, J., Broquet, G., Bréon, F.-M., Puygrenier, V., Chevallier, F., Xueref-Rémy, I., Dieudonné, E., Lopez, M., Schmidt, M., Ramonet, M., Perrussel, O., Lac, C., Wu, L., and Ciais, P.: The first 1-year-long estimate of the Paris region fossil fuel CO₂ emissions based on atmospheric inversion, *Atmospheric Chemistry and Physics*, 16, 14703–14726, <https://doi.org/10.5194/acp-16-14703-2016>, 2016.
- Sussmann, R., Stremme, W., Burrows, J. P., Richter, A., Seiler, W., and Rettinger, M.: Stratospheric and tropospheric NO₂ variability on the diurnal and annual scale: a combined retrieval from ENVISAT/SCIAMACHY and solar FTIR at the Permanent Ground-Truthing Facility Zugspitze/Garmisch, *Atmospheric Chemistry and Physics*, 5, 2657–2677, <https://doi.org/10.5194/acp-5-2657-2005>, 2005.
- Sussmann, R., Forster, F., Rettinger, M., and Bousquet, P.: Renewed methane increase for five years (2007–2011) observed by solar FTIR spectrometry, *Atmospheric Chemistry and Physics*, 12, 4885–4891, <https://doi.org/10.5194/acp-12-4885-2012>, 2012.

- Tallis, L., Coleman, M., Gardiner, T., Ptashnik, I., and Shine, K.: Assessment of the consistency of H₂O line intensities over the near-infrared using sun-pointing ground-based Fourier transform spectroscopy, *Journal of Quantitative Spectroscopy and Radiative Transfer*, 112, 2268–2280, <https://doi.org/10.1016/j.jqsrt.2011.06.007>, 2011.
- Toon, G. C.: The JPL MkIV interferometer, *Opt. Photon. News*, 2, 19–21, <https://doi.org/10.1364/OPN.2.10.000019>, 1991.
- Toon, G. C.: Telluric line list for GGG2014, TCCON data archive, hosted by the Carbon Dioxide Information Analysis Center, Oak Ridge National Laboratory, Oak Ridge, Tennessee, U.S.A., <https://doi.org/10.14291/TCCON.GGG2014.ATM.R0/1221656>, 2014.
- Tran, H., Hartmann, J.-M., Toon, G., Brown, L., Frankenberg, C., Warneke, T., Spietz, P., and Hase, F.: The 2ν₃ band of CH₄ revisited with line mixing: Consequences for spectroscopy and atmospheric retrievals at 1.67 μm, *Journal of Quantitative Spectroscopy and Radiative Transfer*, 111, 1344–1356, <https://doi.org/10.1016/j.jqsrt.2010.02.015>, 2010.
- Turnbull, J. C., Sweeney, C., Karion, A., Newberger, T., Lehman, S. J., Tans, P. P., Davis, K. J., Lauvaux, T., Miles, N. L., Richardson, S. J., Cambaliza, M. O., Shepson, P. B., Gurney, K., Patarasuk, R., and Razlivanov, I.: Toward quantification and source sector identification of fossil fuel CO₂ emissions from an urban area: Results from the INFLUX experiment, *Journal of Geophysical Research: Atmospheres*, 120, 292–312, <https://doi.org/10.1002/2014JD022555>, 2014.
- United Nations: World Urbanization Prospects: The 2014 Revision, United Nations, Department of Economic and Social Affairs, Population Division, 2015.
- Viatte, C., Lauvaux, T., Hedelius, J. K., Parker, H., Chen, J., Jones, T., Franklin, J. E., Deng, A. J., Gaudet, B., Verhulst, K., Duren, R., Wunch, D., Roehl, C., Dubey, M. K., Wofsy, S., and Wennberg, P. O.: Methane emissions from dairies in the Los Angeles Basin, *Atmospheric Chemistry and Physics*, 17, 7509–7528, <https://doi.org/10.5194/acp-17-7509-2017>, 2017.
- Vogel, F. R., Thiruchittampalam, B., Theloke, J., Kretschmer, R., Gerbig, C., Hammer, S., and Levin, I.: Can we evaluate a fine-grained emission model using high-resolution atmospheric transport modelling and regional fossil fuel CO₂ observations?, *Tellus B: Chemical and Physical Meteorology*, 65, 18681, <https://doi.org/10.3402/tellusb.v65i0.18681>, 2013.
- Vogel, F. R., Frey, M., Stauffer, J., Hase, F., Broquet, G., Xueref-Remy, I., Chevallier, F., Ciais, P., Sha, M. K., Chelin, P., Jeseck, P., Te, Y. V., Groß, J., Blumenstock, T., Tu, Q., and Orphal, J.: XCO₂ in an emission hot-spot region: the COCCON Paris campaign 2015, *Atmospheric Chemistry and Physics Discussions*, 2018, 1–37, <https://doi.org/10.5194/acp-2018-595>, URL <https://www.atmos-chem-phys-discuss.net/acp-2018-595/>, 2018.
- Washenfelder, R. A., Toon, G. C., Blavier, J.-F., Yang, Z., Allen, N. T., Wennberg, P. O., Vay, S. A., Matross, D. M., and Daube, B. C.: Carbon dioxide column abundances at the Wisconsin Tall Tower site, *Journal of Geophysical Research: Atmospheres*, 111, <https://doi.org/10.1029/2006JD007154>, 2006.
- Weimer, M., Schröter, J., Eckstein, J., Deetz, K., Neumaier, M., Fischbeck, G., Hu, L., Millet, D. B., Rieger, D., Vogel, H., Vogel, B., Reddmann, T., Kirner, O., Ruhnke, R., and Braesicke, P.: An emission module for ICON-ART 2.0: implementation and simulations of acetone, *Geoscientific Model Development*, 10, 2471–2494, <https://doi.org/10.5194/gmd-10-2471-2017>, 2017.

- Wofsy, S. C.: HIAPER Pole-to-Pole Observations (HIPPO): fine-grained, global-scale measurements of climatically important atmospheric gases and aerosols, *Philosophical Transactions of the Royal Society of London A: Mathematical, Physical and Engineering Sciences*, 369, 2073–2086, <https://doi.org/10.1098/rsta.2010.0313>, 2011.
- Wu, L., Broquet, G., Ciais, P., Bellassen, V., Vogel, F., Chevallier, F., Xueref-Remy, I., and Wang, Y.: What would dense atmospheric observation networks bring to the quantification of city CO₂ emissions?, *Atmospheric Chemistry and Physics*, 16, 7743–7771, <https://doi.org/10.5194/acp-16-7743-2016>, 2016.
- Wunch, D., Toon, G. C., Wennberg, P. O., Wofsy, S. C., Stephens, B. B., Fischer, M. L., Uchino, O., Abshire, J. B., Bernath, P., Biraud, S. C., Blavier, J.-F. L., Boone, C., Bowman, K. P., Browell, E. V., Campos, T., Connor, B. J., Daube, B. C., Deutscher, N. M., Diao, M., Elkins, J. W., Gerbig, C., Gottlieb, E., Griffith, D. W. T., Hurst, D. F., Jiménez, R., Keppel-Aleks, G., Kort, E. A., Macatangay, R., Machida, T., Matsueda, H., Moore, F., Morino, I., Park, S., Robinson, J., Roehl, C. M., Sawa, Y., Sherlock, V., Sweeney, C., Tanaka, T., and Zondlo, M. A.: Calibration of the Total Carbon Column Observing Network using aircraft profile data, *Atmospheric Measurement Techniques*, 3, 1351–1362, <https://doi.org/10.5194/amt-3-1351-2010>, 2010.
- Wunch, D., C Toon, G., L Blavier, J.-F., A Washenfelder, R., Notholt, J., J Connor, B., W T Griffith, D., Sherlock, V., and Wennberg, P.: The Total Carbon Column Observing Network, 369, 2087–112, <https://doi.org/10.1098/rsta.2010.0240>, 2011.
- Wunch, D., Toon, G. C., Sherlock, V., Deutscher, N. M., Liu, X., Feist, D. G., and Wennberg, P. O.: The Total Carbon Column Observing Network’s GGG2014 Data Version, <https://doi.org/10.14291/TCCON.GGG2014.DOCUMENTATION.R0/1221662>, 2015.
- Yang, Z., Washenfelder, R. A., Keppel-Aleks, G., Krakauer, N. Y., Randerson, J. T., Tans, P. P., Sweeney, C., and Wennberg, P. O.: New constraints on Northern Hemisphere growing season net flux, *Geophysical Research Letters*, 34, <https://doi.org/10.1029/2007GL029742>, 2007.

Acknowledgements

Diese Arbeit wurde am Institut für Meteorologie und Klimaforschung (IMK) am Karlsruher Institut für Technologie durchgeführt. Mein erster Dank gilt Herrn Prof. Dr. Johannes Orphal für die Möglichkeit, diese spannende Doktorarbeit erstellen zu dürfen. Weiterhin bedanke ich mich für die Übernahme des Referats. Bei Herrn Prof. Dr. André Butz bedanke ich mich für die Übernahme des Korreferats sowie seine Hilfe bei der Planung eines wissenschaftlichen Auslandsaufenthaltes in Japan.

Mein besonderer Dank gilt Dr. Frank Hase. Ihm möchte ich für die unermüdlichen Anregungen und Hilfestellungen sowie fortwährende Bereitschaft zur Beantwortung von wissenschaftlichen Fragen danken. Die vielen gemeinsamen Stunden zur Feinjustierung unzähliger Spektrometer sollen hier nicht unerwähnt bleiben. Weiterhin möchte ich Dr. Thomas Blumenstock für seine Unterstützung danken, die kritische Durchsicht der gesamten Arbeit und für die Möglichkeit, die Ergebnisse meiner wissenschaftlichen Arbeit auf internationalen Konferenzen zu präsentieren. Der gesamten Bodengruppe danke ich für eine tolle gemeinsame Zeit, erinnert sei zum Beispiel an gemeinsame Abende während der Messkampagne 2014 in Berlin (Ein gemütlicher Grillabend zum Achtelfinale der Fussball WM bleibt mir besonders in Erinnerung) oder gemeinsame Aktivitäten während der NDACC-TCCON Konferenzen.

Auch bei meinen Mitdoktoranden und Kollegen möchte ich mich für die fortwährende Unterstützung sowie eine tolle Zeit am IMK bedanken.

Ich bedanke mich bei der Karlsruher Graduiertenschule für Klima und Umwelt (GRACE) für die Ermöglichung meines Auslandsaufenthaltes in Japan am National Institute for Environmental Studies und der Japan Aerospace Agency.

I gratefully thank Dr. Isamu Morino for hosting me at the National Institute for Environmental Studies and Dr. Kei Shiomi for hosting me at the Japan Aerospace Agency. I thank both of you for the hospitality you showed me and for the helpful discussions. I want to thank Takahiro Nakatsuru for a great time in Tsukuba and an introduction to Japanese culture.

Zu guter Letzt danke ich meiner Familie und meinen Freunden für die Unterstützung während der Anfertigung dieser Doktorarbeit.